UNIVERSITY OF CALIFORNIA
SANTA CRUZ

THE INTERNAL HISTORY OF THE MOON AND KUIPER BELT OBJECTS FROM GRAVITY AND TOPOGRAPHY

A dissertation submitted in partial satisfaction of the
requirements for the degree of

DOCTOR OF PHILOSOPHY

in

EARTH SCIENCE

by

Jack Conrad

December 2020

The Dissertation of Jack Conrad
is approved:

Professor Francis Nimmo, Chair

Professor Noah Finnegan

Professor Ian Garrick-Bethel

Dr. Ross Beyer

Quentin Williams
Interim Vice Provost and Dean of Graduate Studies

Copyright © by

Jack Conrad

2020

Table of Contents

List of Figures **v**

List of Tables **xii**

Abstract **xiii**

Dedication **xv**

Acknowledgments **xvi**

1 Introduction **1**

2 Lunar impact history constrained by GRAIL-derived basin relaxation measurements **4**

2.1 Introduction 5
2.2 Basin catalog updates in light of GRAIL data 8
2.2.1 Basin identification 8
2.2.2 Crater counting technique 11
2.2.3 Results 15
2.3 A basin relaxation transition 20
2.3.1 Measuring relaxation 20
2.3.2 Results 22
2.4 The early lunar bombardment timescale 27
2.4.1 Scenarios for the lunar bombardment history 27
2.4.2 Absolute timing using LMO thermal models and lunar cratering chronologies 33
2.5 Discussion 38
2.5.1 Summary 38
2.5.2 Hemispherical/Latitudinal variations 41
2.5.3 HSEs and the maximum number of basins 41
2.5.4 Timing for basin retention 47

2.5.5 Elusive ages for Asperitatis and Fecunditatis 49
2.6 Conclusions 50

3 An upper bound on Pluto's heat flux from a lack of flexural response of its normal faults 52
3.1 Introduction 53
3.2 Observations 55
3.3 Methods and results 62
3.3.1 Deflection 62
3.3.2 Heat flux 69
3.4 Discussion and conclusions 74
3.4.1 Other heat flux estimates 74
3.4.2 Relaxed craters as a possible heat flux constraint 75
3.4.3 Fault stresses 76
3.4.4 Implications of constraining Pluto's elastic thickness and heat flux in regard to surface features 77

4 Heat Flux Constraints from Variance Spectra of Pluto and Charon from Limb Profile Topography 79
4.1 Introduction 80
4.2 Methods 83
4.2.1 Limb picking methods 83
4.2.2 Limb fitting methods 86
4.2.3 Data processing methods 87
4.3 Analysis 91
4.3.1 Limb topography correlations 91
4.3.2 Topographic variance spectra 93
4.3.3 Topographic support 97
4.3.4 Heat flux 103
4.4 Discussion 108
4.4.1 Early heat sources for Charon 108
4.4.2 Comparisons with previous Pluto/Charon topographic variance results 112
4.4.3 Stresses induced by faulting 114
4.5 Conclusions 116

A Supplementary Figures for Chapter 2 118

B Supplementary Figures for Chapter 3 122

C Supplementary Data for Chapter 4 124

List of Figures

2.1 Crater counts, cumulative size frequency distribution, and R-plots for four proposed basins. From left to right for each basin: maps of the basin count areas with craters in red and the counting areas in black or blue, and the two types of crater size frequency plots: cumulative distribution (CSFD) and relative plot (R-plot) (see Group (1979)) . . . 16

2.2 Crater counting data and relative model age curves. Panels show the cumulative frequency distribution for each of the four proposed basins with crater counts. For derivation of the model crater chronology curves, see text. 17

2.3 Crustal thickness ratios for basins >450 km as a function of relative age. High crustal thickness ratios signify relaxed basins, while low values are unrelaxed. Older basins are to the left. Symbols are colored by diameter and the shape represents the catalog (or catalogs) the basin's properties are sourced. Basins with transparent symbols have doubtful impact origins and weak Bouguer gravity signals (Section 2.2.1). Basins with an inset P are located within the Procellarum KREEP Terrane on the nearside, and those with an inset N are located on the nearside, but not within the PKT. There is a significant switch from relaxed to unrelaxed between PN4 and PN5, with a few explainable outliers. . . . 24

2.4 A comparison of five lunar cratering chronologies assuming a scaling value of b=2.25 (blue, red, green, and cyan curves), the observed range of the cumulative number of basins that formed after PN4 (black solid lines), the cumulative total number of basins (black dashed lines), and the range of LMO solidification and cooling models (grey box, Section 2.4.2). Chronologies are scaled up from $N(1)$ or $N(20)$ (per km2) to $N(450)$ for the whole Moon. The observed number of basins $\geq$ 450 km, after PN4 is 13–15 and before that time is 8–16 (see Section 2.5.3). Top Panel A – terminal cataclysm an extrapolated scenario based on Robbins (2014). Middle Panel B – declining bombardment scenario based on Neukum et al. (2001) (red) and accretion tail scenario based on Morbidelli et al. (2018) (cyan). Bottom Panel C – two sawtooth scenarios based on Morbidelli et al. (2012) (Solid) and Morbidelli et al. (2018) (Dash). Successful chronologies intersect the solid black lines within the grey box. We include two variations with different b values with Figures A.3 and A.4. 29

2.5 Timeline of geophysical events presented in this study. A graphical representation of Table 2.4 in conjunction with LMO solidification age range models (ref. 1: Elkins-Tanton et al. 2011, and ref. 2: Meyer et al. 2010) and Moho cooling models (ref. 3: Kamata et al. 2015). Chronologies ages for the number of unrelaxed basins are shown relative to their coloring in Figure 2.4 (ref. 4: Robbins, 2014; ref. 5: Neukum et al. 2001; ref. 6: Morbidelli et al. 2012, and ref. 7: Morbidelli et al. 2018). Chronologies have to exist within the gray box to match geophysical observations. For example, the Sawtooth chronologies exhibits a high sensitivity to the value of b, and only fits at intermediate to lower b values for the values used in this study. 39

3.1 Image and topographic maps of large faults in Viking Terra and Cthulhu Regio, west of Sputnik Planitia. Left: Locations of maps on the right. Right: Topographic maps (Schenk et al. 2018a) of fault sections with chosen profile line locations. 56

3.2 Comparison of averaged fault profiles. Profiles are vertically offset for clarity and there is ∼17x vertical exaggeration. These profiles are generated using the same technique described in the text but the segments here are 100 km (∼5°) in length rather than the 10° segments used for comparison with topographic models. Inanna, Beatrice, the southern half of Dumuzi, and the northern half of Virgil all show similar forms. The northern side of Dumuzi is dominated by the deeper and longer Inanna Fossa, while Virgil shows a possible half-graben behavior (also noted in Schenk et al. 2018a). 59

3.3 Comparison of observed topography with modeled topography for Inanna Fossa. The uppermost plot is the averaged topographic profile of the faults we included in our study. The red area brackets the profile to show the profile's standard deviation. The lowermost four plots show the resulting model topography when the load described in this section is applied to a plate of various elastic thicknesses. As the elastic thickness increases the resulting model topography approaches the applied load shape. These may be compared to the uppermost plot. The red area in each box represents the standard deviation of Inanna's topographic profiles. 65

3.4 Relative misfit between our modeled deflection topography and the averaged topographic profiles for the extensional graben. The misfit is normalized by the asymptotic misfit for each graben. Color of each line matches the color scheme used in Figure 3.2 as shown in the figure legend. The dashed line represents the relative χ^2-value (1.74) for which a t_e parameter does not produce a model result misfit significantly (α=0.10) different than the background misfit. For the three largest fossae this crossover occurs at ∼8–10 km and for this reason we use 8 km as our minimum t_e value for the analysis in the following sections. 68

3.5 Temperature at the base of the elastic layer and maximum surface heat flux as it relates to strain rate with the elastic thickness set at t_e=8 km and a De range of 0.01–0.001. The elastic thickness is derived from the model for Figure 3.3 and is the minimum value based on our analysis. The three colors correspond to different grain sizes, with red as 10 cm, green as 1 cm, and blue as 1 mm, and the line style corresponds to the value of De. For De=0.001, the results for 10 cm and 1 cm nearly overlap which is a signal that the GBS-accommodated basal slip (which depends on grain size) is less prominent relative to dislocation creep at large grain sizes for our set of parameters. For De=0.01, the results for all three grain sizes overlaps which is a factor of dislocation creep dominating the cumulative ice flow. 73

4.1 Maps of Pluto (a) and Charon (b) with limb profile locations and topography. Labels number specific limbs to the indexing in Figure 4.3, and limbs are generally arranged in the encounter sequence from right to left. Other labels reference major areas on both bodies. Sputnik Planitia (SP), Cthulhu Regio (CR), and Pluto's Far Side (PFS) for Pluto. Vulcan Planitia (VP) and the Charon Far Side (CFS) for Charon. Background images are LORRI/MVIC mosaics (Moore et al. 2016) centered on the anti-encounter hemispheres of Pluto and Charon. Coordinate systems are constructed such that the zero latitude, zero longitude are placed on the Pluto-Charon tidal axis with longitude increasing eastward. Elevation color bars are capped at ±8 km to best show variations near mean elevations. 88

4.2 A comparison of Pluto and Charon limb profiles at similar distances from the two bodies. At a distance of ∼400 Pluto Radii (∼2.25 km/pix ground sample distance), with a vertical exaggeration of ∼132, these show how the topography at different scales vary between the two worlds. Labels to the left of the profiles corresponds to the labels on Figure 4.3, and the profiles are offset by 5 km. The dots plot the raw data before interpolation and detrending. A pixel scale bar is included to show how images translate to our limb profile topography. The 0.2 pixel corresponds to the uncertainty that Dermott and Thomas (1988) found with their similar method. Note the differences in roughness at long and short wavelengths. Charon has notable highs and lows at long wavelengths, but Pluto is rougher at shorter wavelengths. 90

4.3 Stacked Processed (Detrended and Filtered) Limb Profiles for Pluto (a) and Charon (b). The vertical exaggeration for both figures is ∼16. Limbs are labeled in the same manner as in Tables C.1 (Pluto) and C.2 (Charon). Limbs are positive right-hand oriented, with the "western" edge on the left of the panel. 91

4.4 Correlation of Bond albedo and limb profile elevation for Pluto. Linear fit is plotted in red. There is no correlation between the two parameters (R∼0.03). 94

4.5 Pluto and Charon's topographic variance spectra based on limb profile topography. a. Pluto's topographic variance spectrum with a linear fit (red) and broken fit (cyan; Main et al. 1999). The variance results for the 22 Pluto limb profiles are put into 30 bins. The points represent the mean value in each bin and the shading equals the standard deviation. Pluto's topographic variance spectrum is consistent with the expected single power law fit with a power law slope of ∼-1.8. The improvement due to a broken slope is minimal, especially compared to the results of Charon. b. Charon's topographic variance spectrum with a linear fit (red) and broken fit (cyan). The variance results for the 11 Charon limb profiles are put into 30 bins. Charon's topographic variance spectrum is somewhat consistent with a single power law slope of -2, but it is improved by adding a break in the slope at a wavelength ∼150 km. 95

4.6 Change in the Bayesian Information Criteria from the linear fit. Hued lines are for Pluto (green) and Charon (magenta). After determining the BIC for the range of changepoints, we additionally determined the BIC for the linear fit. We consider the linear fit to be the null result, as a single power law slope is the commonly used approximation for the distribution of a solid world's topography and requires the fewest assumptions. To compare Pluto and Charon, we subtract out the linear BIC to calculate the ΔBIC. While the peak for Pluto's curve has some statistical strength (ΔBIC >2; Kass and Raftery, 1995), Charon has a stronger fit over all changepoints. The wavelength range of 70-300 km for Charon is especially significant (ΔBIC >10). 98

4.7 Modeled variance spectra compared with our limb profile spectra. a. Pluto's topographic variance spectrum with compensation model results overlain. The solid lines are from the cartesian model, and dashed lines are the spherical with membrane support. Lines shift in hue from red to blue as the thickness of the elastic layer increases. The primary observation of the results for Pluto are that a thicker elastic layer improves the fit of both models, but the lack of a break in slope only allows for a minimum thickness to be determined. b. Charon's topographic variance spectrum with compensation model results overlain. The solid lines are from the cartesian model, and dashed lines are the spherical with membrane support. Lines shift in hue from red to blue as the thickness of the elastic layer increases. Due to the break in slope a range of elastic thicknesses can be determined instead of a minimum as with Pluto. . . . 102

4.8 Rheologic and heat flux model results for Pluto and Charon. A. Temperature at the base of the elastic layer over a range of strain rates for a variety of rheologic parameters. The results for $De = 10^{-3}$ start to show the trade-off between the dislocation creep and grain-boundary dependent regimes. At the lower De of 10^{-4}, the transition between the same regimes and how they depend more on the grain size as grain-boundary dependence regimes starts to dominate. B. "Heat" map of surface heat flux as a function of the elastic layer thickness and basal temperature. Contours for 10, 20, 30, 50, 75 and 100 mWm^{-2} are plotted in white. Dashed boxes define our estimates for the possible range of heat fluxes for Pluto and Charon. 107
4.9 RMS spectra comparison of Ermakov et al. (2018) and this study. The data from Ermakov et al. (2018) is presented as solid lines, and the data from this study as the binned average with shaded regions of the standard deviation within the bin. Color matches those used in Figures 4.6 and 4.8b. Shorter wavelengths for Charon match well, and longer wavelengths are within the standard deviation. However, there is an observable mismatch of the values for Pluto. 113

A.1 R-plot variation of Figure 2.2. This is a construction similar to the one made for Figure 2.2, but instead we show the relative size-frequency plots for each proposed basin where we achieved a reasonable crater count. . . 118
A.2 Crustal Thickness Ratio Against Basin Diameter Labeled by Region. This figure is a readjustment of Figure 2.3 where the Crustal Thickness Ratio is shown as a factor of diameter and the color labeling is done by region on the Moon. Basins in the thicker farside crust are shown in blue, and the thinner crust nearside basins are shown in warm colors with yellow outside and red inside the PKT region. The Miljkovic et al. (2013) result can be clearly seen for unrelaxed basins. Any apparent trend can better be explained through age rather than location or size. 119
A.3 A comparison of three lunar cratering chronologies assuming a scaling value of b=2.00. Same dimensions and symbolism as Figure 2.4. Lower b values imply that events happen later in lunar history. 120
A.4 A comparison of three lunar cratering chronologies assuming a scaling value of b=2.50. Same dimensions and symbolism as Figure 2.4. Higher b values imply that events happen earlier in lunar history. 121

B.1 Profile topography for the four major Fossa. The derived topography from Schenk et al. (2018a)'s DEM for each of our chosen profiles (black) with the average profile also included (red). Changes in fault depth along strike can be observed, especially with Inanna Fossae where the maximum depth is ∼0.5 km deeper than the average. The vertical exaggeration varies for each set of profiles but is ∼2.5 times for Inanna, ∼10 times for Dumuzi, ∼5 times each for Virgil and Beatrice Fossa. 122

B.2 Comparison of observed topography with modeled topography for Dumuzi, Virgil, and Beatrice Fossa. The uppermost plot is the averaged topographic profile of the faults we included in our study. The red area brackets the profile to show the profile's standard deviation. The lowermost four plots show the resulting model topography when the load described in this section is applied to a plate of various elastic thicknesses. As the elastic thickness increases the resulting model topography approaches the applied load shape. These may be compared to the uppermost plot. We include the red area which represents the standard deviation of the topographic profiles. Beatrice Fossae fits well starting at $t_e = 10$ km, much like Inanna Fossae. This is unlike Dumuzi Fossae for which a load profile fails to fit well. The load profile is a representative profile, while a slightly different profile was used for the north and south flanks in the RMS calculations. 123

List of Tables

2.1 Properties of impact basins ≥450 km analyzed in this study: Location and Age 12
2.2 Properties of impact basins ≥450 km analyzed in this study: Crustal Thickness 14
2.3 Crater counting results for proposed impact structures 15
2.4 Timing of lunar geophysical events. 40

3.1 Parameters used in chapter 3. 63

4.1 Parameters used in chapter 4. 100

C.1 Pluto Image Properties. The spacecraft parameters are calculated using the most consistent SPICE information based on the smithed kernels from Schenk et al. (2018a). 124
C.2 Charon Image Properties. The spacecraft parameters are calculated using the most consistent SPICE information based on the smithed kernels from Schenk et al. (2018b). 126
C.3 Pluto limb fit parameters. The non-identification values in this table have been derived from our limb picking techniques (section 4.2.1) and are utilized in section 4.2.2. 127
C.4 Charon limb fit parameters. The non-identification values in this table have been derived from our limb picking techniques (section 4.2.1) and are utilized in section 4.2.2. 128

Abstract

The Internal History of the Moon and Kuiper Belt Objects from Gravity and Topography

by

Jack Conrad

This thesis comprises two separate but interesting projects that attempt to constrain the internal history of planetary bodies. The first set attempts to interpret the Moon's internal thermal history from the relaxation state of lunar impact basins. As the Moon cools, impact structures degrade at a slower and slower rate. This can be observed in maps of lunar topography and crustal thickness. This analysis, however, was greatly enhanced by the GRAIL spacecraft mission to the Moon. In Chapter 2, I present the first relaxation analysis of the most up-to-date complete lunar impact basin catalog. With the addition of ∼6 new impact basins and the re-qualification of other basins, a basin relaxation transition is clearly observed in the lunar impact record. This relaxation transition signal can be used to constrain and link lunar solidification and cooling models with impact chronology models. In that study, I find that if the lunar surface experienced a lull in basin-class impacts it must have solidified and cooled rapidly following its formation.

The second project involves two studies that try to understand the thermal history of Pluto and its moon Charon. In July 2015, the field of Kuiper Belt Objects was greatly widened with the arrival of the New Horizons spacecraft at the Pluto-Charon

system. One of the major discoveries of that mission was the prevalence of extensional tectonic features on both worlds, a likely signal of a frozen-out (or possibly still freezing) subsurface ocean. In Chapter 3, I characterize the large extensional tectonics features in the encounter hemisphere on Pluto. Then by comparing the features to topographic flexure models, I was able to constrain the maximum surface heat flux experienced by Pluto. This showed that Pluto's internal evolution matches thermal models that primarily use a radiogenic heat source.

Although Chapter 3 put maximum heat flux constrains on the thermal history of Pluto, the constraints can be improved upon and expanded to include analysis of Charon's surface. In Chapter 4, I create and use limb profile topography of Pluto and Charon to understand the differences in the morphological and interior history of the two worlds. This is achieved by calculating the topographic variance spectra from limb profiles, which typically results in a single-power law spectrum. While this typical case holds for Pluto, it does not for Charon which displays a characteristic wavelength. My analysis further constrains an upper limit for Pluto's maximum surface heat flux, but it also sets a range for the absolute maximum heat flux for Charon that cannot be solely explained by radiogenic heating. This implies that an extra heat source, probably tidal heating, was necessary.

For Rachel and Sarek.

Acknowledgments

I am kind of surprised that my PhD is nearly complete, although everything is temporally confused with "Shelter in Place". While working from home, however, the world has surprisingly remained opened. We can now watch seminars from all over the world, and I can talk with friends across the country more consistently. But, this all also makes me more focused on how the years before the pandemic had gone.

My first forays into planetary science were guided by the late Jay Melosh while I was at Purdue. The research project I did with Jay confirmed that studying physics through geology was and is my path. The world lost Jay about a month ago as of my writing this thesis. We lost him far too soon and I am saddened that I will never get to continue my undergrad project with him.

In retrospect, my journey at Santa Cruz began more than a year before I took my first step in the university. At AGU 2013, I met Francis for the first time when Jay introduced me. Although it was just a passing meeting, I am glad that I eventually decided to go to Santa Cruz to work with Francis. He has been a great guiding help in focusing my study of planetary science. I am always grateful for the time I have spent in Francis' research group.

Also while at Santa Cruz (and in the Bay Area) I am grateful for the other professors and scientists in the region, especially my reading committee. While research project attempts with Noah Finnegan and Ian Garrick-Bethel did not take-off into fully fledged projects, my discussions with them were greatly informative. I am also thankful

to work with Ross Beyer on my two Pluto related projects. Without him I certainly would have made many geographical mistakes.

When I first got to Santa Cruz, the only planetary grads were Carver, Nick, and myself. Following us, a large amount of new students have entered the group. Now the group is nearly at a dozen and is one of the more cohesive groups in the department. Thanks Nick, Rachel, Szilard, Megan, Coby, Huazhi, Wenchang, Brynna, Linfeng and Secana.

There are two additional graduate students I want to thank and nominate as honorary planetary grads: Adrienne and Sarah. Without either of you, my time at UCSC would have been less entertaining and my belly would have been filled with far fewer baked goods.

I also could never have achieved anything in this department without the help of the administrative/support staff in the Earth and Planetary Sciences department. Jennifer and Amy in particular have been of extreme help in navigating the intricacies of academic bureaucracy. They, along with all the other staff, are unappreciated and I only hope that everyone in the department

There are other people in Santa Cruz I want to thanks, namely Nat and MihnThi. Thanks for dealing with living in the same houses as me for about 4 years or so. I'm glad I was able to meet people like you two outside of the school.

A special thanks to my family. I'm sorry that I moved so far away from y'all in the midwest, which caused me to miss weddings and births. Yet I'm glad how much support you have shown over my entire life. Thanks to Mom for the hugs and Dad

for the worried concern. Thanks to Chloe and Lawrence for being real with me when necessary. Julian and Elias, I'm excited to be a few states closer to watch my nephews grow.

Rachel. You're the best, I hope you know that, and I'm excited to keep working with and supporting each other for the future to come. I hope we have 5ever to go.

Previously published material

The text of this thesis includes modified reprints of the following previously published material:

Chapter 2: Conrad, J. W., F. Nimmo, C. I. Fassett, and S. Kamata (2018) "Lunar impact history constrained by GRAIL-derived basin relaxation measurements." Icarus 314, 50-63

Chapter 3: Conrad, J. W., F. Nimmo, P. M. Schenk, W. B. McKinnon et al. (2019) "An upper bound on Pluto's heat flux from a lack of flexural response of its normal faults." Icarus 328, 210-217

Chapter 4: Conrad, J. W., F. Nimmo, R. A. Beyer, C. J. Bierson, and P.M. Schenk (2021) "Heat Flux Constraints from Variance Spectra of Pluto and Charon from Limb Profile Topography." Journal of Geophysical Research: Planets, submitted.

Chapter 1

Introduction

This thesis is split into two parts, the second of which comprises two different studies. The first part concerns constraining the thermal evolution of the Moon from the degradation state of its largest impact structures. While the difference between the Earth and Moon's impact histories is not completely understood, they had to have been similar as they sample from the same impactor population. Understanding the impact history of the Moon in its first billion years would help our understanding of the condition of Earth's surface during that same time frame. However, due to the leftover heat from formation the topographic signature of most of the oldest impact basins are muted (Freed et al. 2014). This makes identification of these oldest impact basins difficult without additional information.

This additional information now exists in the form of GRAIL gravity data. Identification of crustal thinning due to mantle uplift can be observed as a large region of higher gravitational acceleration. From this a new impact basin catalog was determined

(Neumann et al. 2015), and numerous structures with no clear topographic basin but with a signal of mantle uplift were discovered. These newly discovered, probable impact basins represent the oldest events that the lunar crust was able to preserve.

In the first part of this thesis I present work that attempted to place these newly discovered probable impacts into the context of the lunar impact history. I used topography and gravity maps along with crustal thickness models to determine the stratigraphic age of these structures with a technique called crater counting (Fassett and Head 2008; Fassett et al. 2012). This technique determined that the structures, or at least the overlying (and thus younger) terrain, are among the oldest on the Moon. I then used techniques from Kamata et al. (2015) to calculate the relaxation state of all known impact basins. The results of this analysis form the focus of Chapter 2.

The second part of the thesis studies results from the New Horizons spacecraft flyby of the Pluto system (Stern et al. 2015). This mission has cast new questions to ask about the formation and evolution of the worlds in the Pluto system and Kuiper Belt Objects in general. One of the more intriguing surface features discovered on Pluto (and Charon) are large extensional fault complexes. Through their size and shape, these faults likely contain information about the internal thermal evolution of Pluto. I discuss efforts to constrain the maximum surface heat flux since the formation of the faults in Chapter 3.

The other Pluto/Charon related chapter (ch. 4) details the creation and analysis of an additional topography dataset for the two bodies using the body edge in images (i.e. the limb profile). While the work in Chapter 3 was able to constrain the

maximum heat flux since the formation of the faults, the constraint only weakly narrowed down possible sources of heat. Using the limb profile topography, I was able to calculate topography variance spectra for Pluto and Charon. With the spectra I was able to further constrain a maximum possible surface heat flux for Pluto and determine upper and lower bounds for Charon. I detail the implications that these limb profiles hold for the formation and evolution of the Pluto system in Chapter 4.

Chapter 2

Lunar impact history constrained by GRAIL-derived basin relaxation measurements

This chapter is a slightly modified reprint of work previously published as Conrad, J. W., F. Nimmo, C. I. Fassett, and S. Kamata (2018) "Lunar impact history constrained by GRAIL-derived basin relaxation measurements." Icarus 314, 50-63. https://doi.org/10.1016/j.icarus.2018.05.029

Abstract

GRAIL observations have been used to derive an updated catalog of lunar impact basins with diameters ≥450 km. In this study, we assess the age and relaxation state of these basins and find that the 13–15 stratigraphically younger basins are

significantly less relaxed than the 8–16 identifiable older basins. The change in relaxation state is most likely a signature of the cooling of the base of the lunar crust below 1300–1400 K, which we infer happened between 4.21–4.45 Ga based on geochronological measurements. We compare the predicted number of basins before and after this reference point with several different modeled lunar cratering chronologies. While these models are sensitive to the ratio of 1km:450 km craters, we conclude that a model with a broad period of late heavy bombardment (a "sawtooth") is more likely to fit both the number of relaxed and unrelaxed basins, and the mass of material delivered as a late veneer.

2.1 Introduction

The early bombardment history of the Moon provides fundamental constraints on the final stages of planetary accretion. The total mass delivered, the duration of delivery, and the size-distribution of the impactors have all been used to distinguish between different accretion scenarios (Stöffler et al. 2006; Bottke and Norman 2017). In particular, the idea that the Moon experienced a late increase in bombardment rate around 3.9–4.1 Ga, originally proposed on geochronological grounds (Tera et al. 1974; Wetherill 1975; Cohen et al. 2000), has been used to argue for a dramatic reorganization in solar system architecture at that time (Tsiganis et al. 2005; Walsh and Morbidelli 2011; Marchi et al. 2012; Bottke et al. 2012). While the strength, duration, and existence of this increase have been called into question (Michael et al. 2018), the idea of a late

heavy bombardment (LHB) has remained a significant hypothesis in the field (Bottke and Norman 2017).

Interpreting the lunar bombardment history as recorded by the largest impact basins has proven to be complicated, for two main reasons. First, while relative ages of the basins can be established using cross-cutting relationships or crater counts, absolute age estimates based on sample geochronology are only available for a few of the younger basins, and these age estimates are contentious (Stöffler et al. 2006; Michael et al. 2018). Second, definitive recognition of ancient basins is difficult because their surface expressions tend to be subtler than younger basins.

Recently, however, both problems have been partially mitigated. For the first point, Kamata et al. (2015) suggested that the extent that basins have viscously relaxed could be used to infer their absolute age. Only basins that formed around the solidification of the magma ocean and relatively shortly thereafter should show relaxation and still be observable. That solidification time can be determined using geochemical and geophysical models, allowing us to link the onset of unrelaxed basins to an absolute age. This was done previously on the basis of the topographic expression of the basin floors and rims (Baldwin 1987), but with improved crustal thickness models (Wieczorek et al. 2013) and computational advances we now have a more complete picture of basin relaxation. We will also comment on the fate of basins produced by impacts before any observable feature can be preserved. For the second point, Neumann et al. (2015) used gravity data from the GRAIL mission (Zuber et al. 2013) to identify ancient basins based on inferred mantle uplift, thus avoiding some of the previous identification challenges

based on image and topography data alone.

Kamata et al. (2015) did not have access to the updated basin catalog provided by Neumann et al. (2015). In this study, we expand the Kamata et al. (2015) relaxation analysis by making use of Neumann et al. (2015)'s results. This requires that we calculate the age of these newly identified lunar basins using a relative age system. Below we detail our changes to the basin catalog used in Kamata et al. (2015). Although we find that the transition from relaxed to unrelaxed basins is not as clear as in Kamata et al. (2015), we argue that it is more robust due to the fact that our basin catalog is more complete. We also use our results to investigate which of several proposed lunar cratering chronologies are most consistent with the basin constraints.

The structure of the rest of this paper is as follows. We first discuss how the basin catalog used by Kamata et al. (2015) is modified in the light of the GRAIL results and provide crater size-frequency data (relative ages) for some newly-identified basins. This is a different emphasis from the Kamata et al. (2015) study that focuses more on relaxation calculations and not on basin detection and age determination. We then discuss the implications of the ages assigned to these structures given their relaxation state. Specifically, we focus on tying together lunar magma ocean (LMO) solidification models to lunar cratering chronologies in order to determine how various chronology styles (such as those described in Bottke and Norman (2017) and Morbidelli et al. (2018)) are sensitive to the geophysical constraints we describe in this study. We then discuss the implications of these results for the number and fate of basins on the Moon.

2.2 Basin catalog updates in light of GRAIL data

2.2.1 Basin identification

For our study, we begin with the basin catalog compiled by Neumann et al. (2015). Prior to that work, basin identification primarily used morphology and/or topography data (Wilhelms et al. 1987; Cook et al. 2002; Frey 2011). This made ancient basins – subject to subsequent burial or overprinting – hard to recognize. GRAIL maps of the Bouguer gravity anomaly revealed that some of these hypothesized ancient basins were also characterized by an uplifted mantle, making their impact origin much more secure (Neumann et al. 2015). Conversely, some proposed ancient basins, like many in Frey (2011), showed no signs of mantle uplift. While absence of uplift does not rule out an impact origin – the basin could have undergone complete relaxation – it does place constraints on the thermal state of the crust at the time of formation. We discuss this issue further below.

Tables 2.1 and 2.2 provide an updated catalog of basins with diameters $\geq$450 km, making use of GRAIL data. This table may be compared directly with that of Kamata et al. (2015). There are three principal differences. First, we have added six additional basins (Fitzgerald-Jackson, Australe North, Mutus Vlacq, Asperitatis, Moscoviense-North, and Topo-22) based on the GRAIL results discussed above – these are marked in bold. For these proposed basins we find relative age assignments, discussed in more detail in the subsequent sections.

Second, we regard several of the basins used by Kamata et al. (2015) (marked

with brackets) as being of uncertain origin, because of the absence of Bouguer anomalies. These features are mostly circular, visible depressions cataloged in Wilhelms et al. (1987) (e.g. Werner-Airy, Marginis, etc) as possible or doubtful impact basins. We chose not to exclude these features completely, but make note of where our results are significantly changed by their inclusion. The stance we take on these doubtful basins is that they are unlikely to lose this doubtful status and will more than likely fall out of future crater catalogs. The primary reason we include them in our catalog is so that we can compare our results with Kamata et al. (2015). From the table we can see that there are 30 total possible basins, with diameter $\geq$450 km, with 22 having strong Bouguer anomalies indicative of impact origin.

Third, we check for basins where their published properties have been updated using LOLA and GRAIL data. This only adds the basin Dirichlet-Jackson, which was confirmed using LOLA topography (Head et al. 2010), but its crater rim is degraded, and its diameter was assigned as <450 km. Neumann et al. (2015), using GRAIL gravity data, found a diameter of 452 km and that qualifies it for our catalog. However, we should note that diameter estimates from GRAIL data inherit some amount of uncertainty. This does not change any results in this study, but may change future studies that focus on a broader diameter range of basins.

More complicated sub-surface structure has been recognized at the location of some previously proposed impact basins in GRAIL data. One such structure is found under Mare Insularum, which was previously identified as an impact basin based on circular patterns of "terra islands" poking out of the maria (Wilhelms and McCauley

1971). However, a set of three medium-sized circular positive gravity anomalies - instead of one large anomaly - were observed in GRAIL data. Neumann et al. (2015) identified these as possible buried impact structures (Copernicus-H, Aestuum, and Medii) and their rims could explain the "terra islands". Given that current evidence supports multiple impact events forming this region's gravitational signature we chose not to include Insularum in our study.

We make other minor changes to the Kamata catalog. For instance, we now use GRAIL or altimetry data, rather than images, as the primary determination of basin diameter. An example of this is Mutus-Vlacq, which was reported in Wilhelms et al. (1987) to have a diameter of 700 km, but the same basin was found by Neumann et al. (2015) to have a diameter of 450 km. The centers of basins also are modified by this new evidence. An example of this is Australe, whose center was reported previously as 94.5°E, 51.5°S (Wilhelms et al. 1987), but GRAIL data revealed that the true center of the positive gravity anomaly associated with the basin is to the north: 96°E, 35.5°S. Therefore, Neumann et al. (2015) decided to rename the structure Australe-North to separate the impact basin from Mare Australe. There are also basins we exclude from our study due to a reduction in the diameter (D<450 km) that had previously been included in Kamata et al. (2015). Balmer-Kapteyn's diameter was previously defined as 550 km (Wilhelms et al. 1987) using the size of the depression southeast of Mare Fecunditatis. However, with GRAIL data, the size of the positive gravity anomaly signals a basin diameter of 265 km.

2.2.2 Crater counting technique

For four of the six newly identified basins in Tables 2.1 and 2.2, we determined an approximate stratigraphic age by using crater counting, specifically the buffered technique (Fassett and Head 2008; Fassett et al. 2012). This technique applies a correction based on craters that are centered outside of the counting region, but have edges intersecting the region. We mapped the preserved basin-related materials and facies, attempting to focus on areas reset by the proposed basin impact ejecta. Three of these features have had areas mapped for crater counting in previous studies: Fitzgerald-Jackson (Fassett et al. 2012), Australe-North (as Australe) (Wilhelms et al. 1987) and Mutus-Vlacq (Wilhelms et al. 1987). However, the counting areas in those studies were based primarily on imaging and/or topography rather than gravity. Because these basins are old, our choice of area is affected by having to avoid deposits from nearby younger features, and gravity helps determine an appropriate counting area. An example of this is how we chose the area for the proposed basin Fitzgerald-Jackson (Figure 2.1) by specifically avoiding basin material from the nearby younger basins Freundlich-Sharanov and Dirichlet-Jackson.

We use a catalog of lunar craters $\geq$20 km in diameter from LOLA data (Head et al. 2010; Kadish et al. 2011) to assist in identifying and counting craters in our mapped areas. The catalog and specific details are found online at `http://www.planetary.brown.edu/html_pages/LOLAcraters.html`. Although the catalog is extensive, it is not complete and there are craters that were missed. We examined the counting area

of each basin to find and include the missing craters; in our areas, we found ∼5% of craters≥20 km were missed by the catalog. This value is smaller than the ∼12% found by Fassett et al. (2012), and we attribute our smaller value to a combination of differences in identification of degraded craters and randomness from using different counting areas. We do compare craters where counting areas in the Fassett et al. (2012) study and this study overlap, and we find no substantial difference beyond the measured diameter of some craters.

To analyze the counting areas, we use the LOLA digital elevation model (DEM; updated 2017) at a 128 pixel per degree (ppd) resolution. This is equivalent to about 235 m/px at the equator. For counting we use the CraterTools extension to ArcMap (Kneissl et al. 2011), which appropriately corrects diameter measurements that occur due to changing the local projection (we use an equal area map projection) and includes the ability to do a buffered count correction (Kneissl et al. 2015).

Table 2.1: Properties of impact basins ≥450 km analyzed in this study: Location and Age

#	Name[a]	Center	Diameter (km)	Rel. Age[b]	Region[c]
1	South Pole-Aitken[d]	190°E, 54°S	2050	PN1	SPA
2	Dirichlet-Jackson[e]	201.8°E, 13.4°N	452	PN2	FHT
3	(Werner-Airy)[f]	12°E, 24°N	500	PN2	FHT
4	**Fitzgerald Jackson**[d]	190.5°E, 25.1°N	564	PN2	FHT
5	(Flamsteed-Billy)[f]	315°E, 7.5°S	570	PN2	PKT
6	(Marginis)[f]	84°E, 20°N	580	PN2	FHT
7	(Al-Khwarizmi-King)[f]	11°E, 21°N	590	PN2	FHT
8	(Tsiolkovsky-Stark)[f]	128°E, 15°S	700	PN2	FHT
9	**Australe North**[g]	96°E, 35.5°S	880	PN2	FHT
10	**Mutus Vlacq**[g]	24°E, 53.5°S	450	PN3	FHT

Continued on next page

Table 2.1 – *Continued from previous page*

#	Name	Center	Diameter (km)	Rel. Age	Region
11	**Topo-22**[gh]	179°E, 49.9°N	500	PN3	FHT
12	(Lomonosov-Fleming)[f]	105°E, 19°N	620	PN3	FHT
13	(Tranquillitatis)[f]	40°E, 7°N	800	PN3	FHT
14	Nubium[d]	344.6°E, 18.6°S	835	PN3	PKT
15	Fecunditatis[f]	52°E, 4°S	990	PN3	PKT
16	(Keeler-Heaviside)[f]	162°E, 10°S	780	PN4	FHT
17	Coulomb-Sarton[f]	237°E, 52°N	530	PN5	FHT
18	Smythii[d]	86.6°E, 1.83°S	887	PN5	FHT
19	Freunlich-Sharonov[d]	175°E, 18.3°N	582	PN8	FHT
20	Moscoviense[d]	149°E, 27.5°N	629	N1	FHT
21	Mendel-Rydberg[d]	266.3°E, 50°S	636	N1	FHT
22	Nectaris[d]	34.7°E, 14.5°S	915	N1	FHT
23	Hertzsprung[d]	231°E, 2°N	549	N2	FHT
24	Humboltdtianum[d]	82°E, 57.2°N	603	N2	FHT
25	Serenitatis[f]	19.2°E, 26.5°N	937	N2	PKT
26	Humorum[f]	320.5°E, 24°S	820	N2	PKT
27	Crisium[d]	59.8°E, 17°N	1092	N2	FHT
28	Orientale[d]	265.4°E, 19.7°S	928	I	FHT
29	Imbrium[d]	17.4°E, 33.5°N	1114	I	PKT
30	**Asperitatis**[g]	26.8°E, 7.7°S	730	Unk	FHT
31	**Moscoviense-North**[g]	148.8°E, 27.3°N	640	Unk	FHT

[a] Names are from their respective sources. Bold signals the new prospective basins with properties mainly sourced from Neumann et al. (2015). Brackets denote doubtful ancient basins, identified in Wilhelms (1987).

[b] Relative Age: PN, N, and I indicate Pre-Nectarian, Nectarian, and Imbrian ages respectively. Non-bold ages from Wilhelms et al. (1987) or are based on other crater counting studies (Fassett et al. 2012). The number refers to the subperiod, with 1 identifying the oldest in a period and counting up decreases the age. (i.e. PN1 is old like SPA and PN9 is the end of the Pre-Nectarian, although no basins are of that subperiod)

[c] PKT, FHT, and SPA indicate the region of the basin location. Procellarum KREEP Terrane, Feldspathic Highlands Terrane, and South Pole-Aitken respectively (Jolliff et al. 2000).

[d] Head et al. (2010)

[e] Wilhelms et al. (1987)

[f] Cook et al. (2002)

[g] Neumann et al. (2015)

[h] Frey (2011)

Table 2.2: Properties of impact basins ≥450 km analyzed in this study: Crustal Thickness

#	Name[a]	Surrounding Crustal Thickness (km)[b]		Crustal Thickness Ratio[b]	
		This Study	K15[c]	This Study	K15[c]
1	South Pole-Aitken	37.9 ± 9.7	37.5 ± 1.7	0.45 ± 0.12	0.41 ± 0.02
2	Dirichlet-Jackson	51.6 ± 7.2	N/A	0.72 ± 0.09	N/A
3	(Werner-Airy)	30.4 ± 5.8	30.3 ± 1.6	0.89 ± 0.12	1.00 ± 0.05
4	**Fitzgerald Jackson**	47.6 ± 8.6	N/A	0.63 ± 0.11	N/A
5	(Flamsteed-Billy)	30.0 ± 6.7	29.9 ± 1.7	0.90 ± 0.17	0.79 ± 0.05
6	(Marginis)	28.8 ± 4.5	28.7 ± 1.0	0.90 ± 0.12	1.00 ± 0.03
7	(Al-Khwarizmi-King)	35.0 ± 5.2	34.9 ± 0.7	0.92 ± 0.11	1.00 ± 0.02
8	(Tsiolkovsky-Stark)	36.1 ± 5.8	36.4 ± 0.9	0.94 ± 0.12	1.00 ± 0.03
9	**Australe North**	33.1 ± 6.3	N/A	0.70 ± 0.12	N/A
10	**Mutus Vlacq**	34.5 ± 5.6	N/A	0.63 ± 0.10	N/A
11	**Topo-22**	41.1 ± 7.2	N/A	0.61 ± 0.11	N/A
12	(Lomonosov-Fleming)	33.8 ± 5.3	33.9 ± 0.5	0.84 ± 0.12	0.95 ± 0.01
13	(Tranquillitatis)	30.7 ± 5.7	31.0 ± 0.9	0.94 ± 0.13	0.95 ± 0.03
14	Nubium	32.1 ± 6.5	32.1 ± 0.6	0.76 ± 0.14	0.75 ± 0.01
15	Fecunditatis	30.3 ± 6.4	30.3 ± 0.6	0.41 ± 0.07	0.42 ± 0.01
16	(Keeler-Heaviside)	37.2 ± 6.8	38.1 ± 0.6	0.84 ± 0.12	0.98 ± 0.02
17	Coulomb-Sarton	38.9 ± 7.8	40.4 ± 0.5	0.48 ± 0.10	0.44 ± 0.01
18	Smythii	31.7 ± 6.7	31.9 ± 1.1	0.21 ± 0.04	0.20 ± 0.01
19	Freunlich-Sharonov	45.2 ± 8.4	45.3 ± 0.2	0.28 ± 0.05	0.27 ± 0.001
20	Moscoviense	39.0 ± 7.2	39.0 ± 0.7	0.20 ± 0.04	0.16 ± 0.003
21	Mendel-Rydberg	31.6 ± 7.3	33.6 ± 0.9	0.36 ± 0.07	0.34 ± 0.01
22	Nectaris	29.4 ± 6.2	29.4 ± 1.9	0.26 ± 0.05	0.25 ± 0.02
23	Hertzsprung	50.1 ± 8.1	50.1 ± 0.7	0.38 ± 0.06	0.38 ± 0.01
24	Humboltdtianum	30.3 ± 4.2	30.2 ± 0.3	0.17 ± 0.03	0.15 ± 0.001
25	Serenitatis	27.2 ± 7.5	28.2 ± 1.0	0.28 ± 0.11	0.25 ± 0.01
26	Humorum	32.1 ± 5.8	32.0 ± 1.0	0.28 ± 0.05	0.24 ± 0.01
27	Crisium	29.3 ± 6.4	29.9 ± 2.5	0.12 ± 0.03	0.07 ± 0.01
28	Orientale	37.9 ± 9.9	38.2 ± 1.7	0.20 ± 0.05	0.20 ± 0.01
29	Imbrium	28.8 ± 5.2	29.2 ± 1.1	0.32 ± 0.05	0.36 ± 0.01
30	**Asperitatis**	33.2 ± 6.7	N/A	0.47 ± 0.09	N/A
31	**Moscoviense-North**	39.0 ± 7.2	N/A	0.20 ± 0.04	N/A

[a] Names are from their respective sources as noted in Table 2.1. Bold signals the new prospective basins with properties mainly sourced from Neumann et al. (2015). Brackets denote doubtful ancient basins, identified in Wilhelms et al. (1987).

[b] A GRAIL based, 34 km average crustal thickness model was used.

[c] Kamata et al. (2015)

2.2.3 Results

Table 2.3 displays the superimposed crater densities and relative ages determined for the proposed basins in Figure 2.1. In the table, we provide $N(20)$ and $N(60)$ metrics. By convention, $N(\mathrm{X})$ is the cumulative number of craters of size greater than or equal to diameter X normalized to an area of 10^6 km^2. Using $N(20)$, $N(60)$, and the shape of the cumulative size frequency distribution and R-plot a relative age can be found as described below.

Table 2.3: Crater counting results for proposed impact structures

Name	Center	Diameter (km)	$N(20)$	$N(60)$	Relative Age	Notes
Fitzgerald-Jackson	190.5°E, 25.1°N	564	258±45	47±20	PN2	Possible artificial high density
Australe North	96°E, 35.5°S	880	173±26	29±9	PN2	Large and small craters have different ages
Mutus Vlacq	24°E, 53.5°S	450	211±20	25±11	PN3	
Topo-22	179°E, 49.9°N	500	233±26	45±18	PN3	R-plot displays a younger age

Figure 2.2 illustrates our relative age period assignment system, which is based on the system designed by Wilhelms et al. (1987). We use the same principles as laid out in that study, but with updated data (Fassett et al. 2012). Individual periods are divided into sub-periods based on the internal stratigraphic super-positioning and crater density comparisons. Pre-Nectarian 1 (PN1) contains the oldest known basin, South Pole-Aitken, and is purely determined by stratigraphy (see Wilhelms et al. (1987) for a further

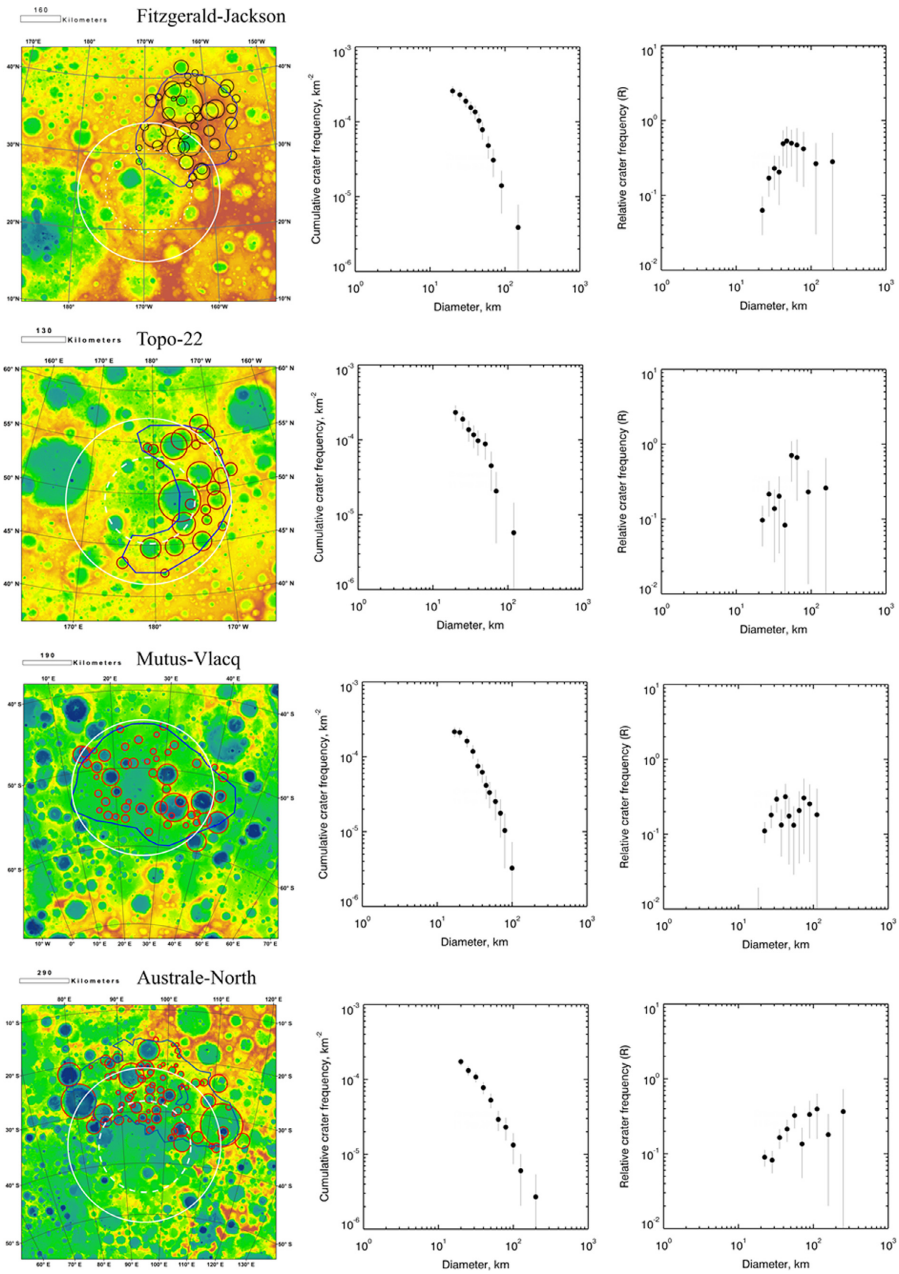

Figure 2.1: Crater counts, cumulative size frequency distribution, and R-plots for four proposed basins. From left to right for each basin: maps of the basin count areas with craters in red and the counting areas in black or blue, and the two types of crater size frequency plots: cumulative distribution (CSFD) and relative plot (R-plot) (see Group (1979))

discussion of SPA). As the sub-period gets younger, the number counts up (PN4 is younger than PN3). The exact numerical extent of each of these periods and sub-periods is based on crater densities derived for basins with clear stratigraphic relationships. Assignment of individual basins to these sub-periods is necessarily provisional, however, given the uncertainty in the crater statistics of individual basins.

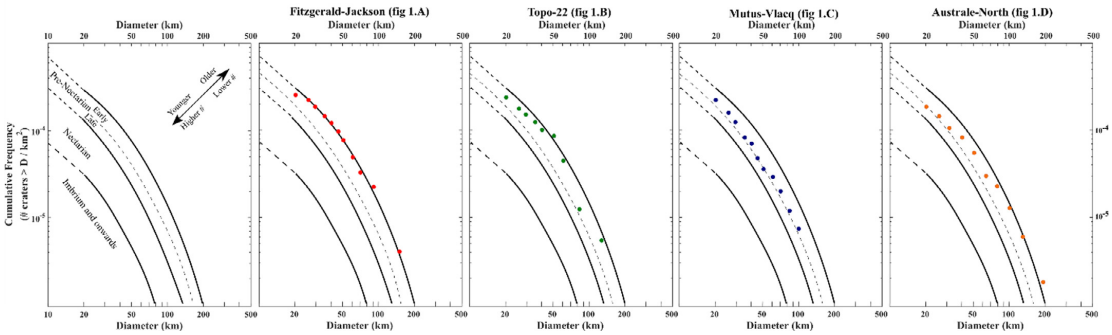

Figure 2.2: Crater counting data and relative model age curves. Panels show the cumulative frequency distribution for each of the four proposed basins with crater counts. For derivation of the model crater chronology curves, see text.

One of the major discoveries from the LOLA lunar topographic dataset found by Fassett et al. (2012) is that crater densities of lunar surfaces are generally higher than previously derived. They show that this increase is especially apparent on Nectarian and Pre-Nectarian surfaces, with an increase in $N(20)$ of 50–70 above the Wilhelms et al. (1987) values being standard on those surfaces. This increase is particularly apparent at lower crater diameters. As such, we cannot directly use Wilhelms et al. (1987) crater count data to construct our relative age period curves. To use the new LOLA-derived crater data we shift the scale of the CSFD used by Wilhelms et al. (1987) (Figure 7.16) upwards by 60 craters / 10^6 km^2 at 20 km for Nectarian and Pre-Nectarian age ranges.

This increase is relatively less pronounced at larger diameters, implying a larger ratio between craters in the 1–20 km range compared with larger complex and basin-scale impacts. This quantifiable increase at 20 km allows us to use the period boundaries as defined in Wilhelms et al. (1987), but with crater densities derived from modern data sets, such as Fassett et al. (2012). We also pin the Nectarian boundary to the Nectaris data obtained by Fassett et al. (2012) (with N(20)$\sim$135) and for the Pre-Nectarian 2 boundary we used counts for the basin Dirichlet-Jackson from the same paper, which showed high crater densities (with $N(20)\sim266$) across all crater bins.

By comparing our crater counts with the revised cumulative plots, we assign ages to 4 of the newly-proposed basins (Figure 2.2). For example, we find that the proposed basin Fitzgerald-Jackson should be in the Pre-Nectarian period with the sub-period assignment of PN2. Another proposed basin, Mutus-Vlacq, has a CSFD curve with lower values for nearly every bin and as such is a younger feature. However, the difference in crater densities is relatively small and gives Mutus-Vlacq a relative age of PN3. Another one of our proposed basins, Australe-North, has a CSFD curve showing a gradual increase with increasing diameter in the relative crater densities compared to what would be expected from the N(20) value. This is similar behavior to SPA, which shows a lack of craters in the 20–60 km range compared to the densities above that range. The explanation given by Fassett et al. (2012) is that a resurfacing event preferentially removed smaller craters. We assume that the same explanation applies for the proposed basin Australe-North basin, which also shows moderate volcanic activity, and as such assign it the relative age of PN2 implied by the larger craters in the counting

area. All of our proposed basins with uncompromised crater counts place in the early pre-Nectarian relative age range (PN2-4). The exact age assignment is not crucial to the arguments we develop below, if all these basins are PN4 or older.

Two of the proposed basins with diameters≥450 km have relative ages that are elusive, due to mare and other basin material that superimpose their surfaces. These proposed impact basins are Asperitatis and Fecunditatis, named for the sinus and mare at their locations, respectively. Asperitatis has been under scrutiny as a possible impact basin for a few decades, but until the advent of high quality GRAIL gravity data there was no convincing evidence for its impact origin. Asperitatis also has a clear stratigraphic relationship with Nectaris, which directly superimposes it and puts the proposed basin in the pre-Nectarian system by definition. Choosing a large enough area where the surface material is primarily Asperitatis basin material, rather than Nectaris or mare material, is impossible. Fecunditatis was previously considered an impact basin (Wilhelms et al. 1987), but no clear rings were found with altimeter data and it was removed from subsequent studies of lunar impact basins (Fassett et al. 2012). However, with GRAIL data, the quasi-circular gravity anomaly associated with impact basins can be observed and its properties can be better determined (Neumann et al. 2015). We temporarily use the assigned relative age of PN3 from Wilhelms et al. (1987) in future sections, but we want to stress that the Wilhelms et al. (1987) assignment is uncertain in the context of modern data. Neumann et al. (2015) found that the Bouguer anomaly for the proposed basin Fecunditatis has roughly the same center, but is about 2/3rd the previous radius (and thus about half the previous area). A smaller radius

makes the area to the southeast (the area Wilhelms et al. (1987) used) unlikely to be Fecunditatis ejecta. Areas to the southwest, which could be related, are more likely to have originated in the Nectaris impact or are covered in mare basalts. Based on results and discussion presented later in this study (Table 2.2, Section 2.3.1, and Section 2.5.5), there is evidence to support a late pre-Nectarian formation age range for both of these impacts. Secondary cratering is a phenomenon that affects the crater density of counting areas, increasing the overall crater density, but it pushes the CSFD away from the source population (Wilhelms et al. 1987; McEwen and Bierhaus 2006). One potential uncertainty in our results is the formation of secondary craters, particularly due to large basins, which have the potential to pollute our measured results. However, even for the largest, younger basins such as Imbrium and Orientale, the number of secondaries larger than 20 km that were produced is relatively minimal (Wilhelms et al. 1978). The size-frequency distribution of secondary craters is steep, with a clear majority being smaller than 20 km (McEwen and Bierhaus 2006). Since we start counting craters at 20 km, secondaries should not be a systematic problem with our results.

2.3 A basin relaxation transition

2.3.1 Measuring relaxation

Older geological features are often more relaxed due to viscous flow of the mantle and crust. Since viscous relaxation of silicates is highly temperature dependent (Karato 2012), the relaxation of large-scale structures such as the thinned crust under

lunar impact basins (Neumann et al. 1996) is expected to have occurred rapidly when the lunar crustal temperature was high and effectively shut off when the crust passed below a critical temperature. Recent numerical models (e.g. Balcerski et al. 2010; Melosh et al. 2013; Dombard et al. 2013; Freed et al. 2014) show that the formation of a large mantle uplift, resulting in a basin interior crust that is about 20–30% the thickness of the surrounding crust, should be standard for lunar basin-class impacts. Lateral flow of crustal material will slowly erase the thinned area, at a rate dependent on the crustal thickness and temperature (Kamata et al. 2015). Inferring the modern crustal thickness of the impact basin relative to the surrounding region allows for a determination of the current relaxation state separate from surface/morphological evidence. The current relaxation state of impact basins serves as evidence of the lunar thermal history since their formation.

We have decided to use a slight variation of the method used by Kamata et al. (2015) to quantify basin relaxation. They used a method where crustal thickness profiles were calculated for every basin by azimuthally averaging the crustal thickness in the region surrounding the basin. From the profile, they found the mean and standard deviation in the range from 2 to 3 basin radii. Our method utilizes a gridded data set (with 0.25-degree resolution) where we averaged the crustal thickness from 2 to 3 basin radii in an annulus around the basin. Our analysis also excludes regions inside the central topographic depressions of other basins, on the basis that they do not represent the surrounding crust. The values obtained using either method are within error of the other, but our grid method allows for the calculation of the crustal thickness variance.

This variance represents the range of crustal thickness values surrounding the basin and is reported as the uncertainty in Table 2.2. We use GRAIL-derived crustal thickness values for the Moon from Wieczorek et al. (2013), specifically the model assuming a 34 km average crustal thickness. Other crustal thickness models from the same study display would not lead to significant differences for our results ($< 10\%$ difference).

For the interior crustal thickness, we used the crustal thickness at the geographical center, rather than the mean or median value of the entire basin interior, to stay consistent with Kamata et al. (2015). Both alternatives are more susceptible to interference from overlying craters.

Once the interior and surrounding crustal thicknesses are found, we can quantify basin relaxation through the crustal thickness ratio. The crustal thickness ratio is the interior crustal thickness divided by the average surrounding crustal thickness, calculated by the method above. A value near one signals that the basin is relaxed, while a value near zero signals the opposite. This value serves to determine whether a basin is relaxed or unrelaxed and is relatively insensitive to modification of surface topography (Head et al. 2010; Fassett and Thomson 2014; Hirabayashi et al. 2017).

2.3.2 Results

Figure 2.3 shows the relaxation state of basins as a function of their relative age. Overall, the behavior is similar to that seen by Kamata et al. (2015), in that more ancient basins show larger degrees of relaxation, while younger basins are generally less relaxed. No basin of age PN5 or younger shows relaxation of$>60\%$, while for

basins of PN4 or older nearly all basins are about 50% or more relaxed. There are two anomalous basins in our study, Fecunditatis and South Pole-Aitken, which appear less relaxed compared to similarly aged basins. We discussed the possible misidentification of the age of Fecunditatis in Section 2.2.3 above on the basis of counting areas, while SPA is likely anomalous due to its size. This is due to the nature of viscous relaxation, where when the wavelength of the feature is much larger than the flowing layer (i.e. the crust) the relaxation timescale goes as (McKenzie et al. 2000):

$$\tau \sim \frac{\eta \lambda^2}{\Delta \rho g \delta^3} \tag{2.1}$$

Here τ is the relaxation timescale, η is the viscosity, λ is the wavelength of the feature, $\Delta\rho$ is the crust-mantle density contrast, g is the surface gravity, and δ is the thickness of the flowing layer. Since wavelength is the major differing variable when considering basins of approximately the same age, we can compare the relaxation of SPA and Australe-North (a more relaxed basin of around the same relative age) for example. The ratio of the relaxation timescales should go as the ratio of the wavelengths squared $(\lambda_1/\lambda_2)^2$. SPA is around 2.5 to 3 times the size of Australe-North, which would imply that the timescale for SPA is an order of magnitude longer than Australe-North. This strong wavelength dependence helps explain why SPA is anomalous in terms of its relaxation state.

In Figure 2.3, basins with a square symbol represent features of uncertain origin, shown with brackets in Table 2.1 (see Section 2.2.1). Although these features may be highly relaxed impact features, there are established basins in the PN2 age range

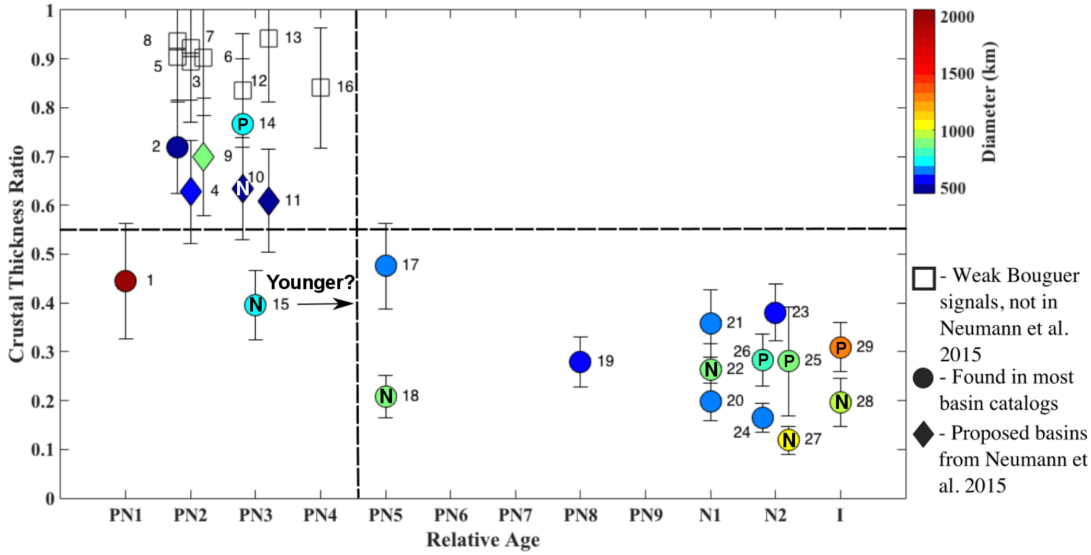

Figure 2.3: Crustal thickness ratios for basins >450 km as a function of relative age. High crustal thickness ratios signify relaxed basins, while low values are unrelaxed. Older basins are to the left. Symbols are colored by diameter and the shape represents the catalog (or catalogs) the basin's properties are sourced. Basins with transparent symbols have doubtful impact origins and weak Bouguer gravity signals (Section 2.2.1). Basins with an inset P are located within the Procellarum KREEP Terrane on the nearside, and those with an inset N are located on the nearside, but not within the PKT. There is a significant switch from relaxed to unrelaxed between PN4 and PN5, with a few explainable outliers.

that are less relaxed (crustal thickness ratios near ∼60–70%). The spread in relaxation state could be real and might result from differences in local thermal state (Miljković et al. 2016) or impact conditions. However, we do not observe any correlation in relaxation state with either longitude or basin diameter; such a correlation would be expected if this kind of explanation were correct (see also Section 2.5.2 below). We also do not see a strong trend between the relaxation state and local thermal variation for nearside basins. This result is also evident in Figure 2.3, where there is no systematic difference between the relaxation state of nearside basins inside or outside the PKT and farside

basins. Also, this result is apparent in Figure A.2, which shows the lack of relationship between relaxation state and diameter.

Figure 2.3 shows a relatively sharp transition in behavior between PN4 and PN5 similar to that identified by Kamata et al. (2015). These authors argued that this transition is associated with cooling of the Moho below a temperature of 1300–1400 K, beyond the point where viscous relaxation is no longer effective. We use the term Moho in the same manner as Kamata et al. (2015) to refer to the base of the crust. Since we care about this boundary only after the LMO has solidified, we consider the location of the Moho to remain constant. Figure 2.3 indicates that only 13 basins formed after this temperature transition (i.e. during or after PN5), or 15 if two additional basins (Fecunditatis and Asperitatis) are included. Moscoviense-North can also be added with Moscoviense, but then the inner ring of the dual basin structure is assumed to be the diameter of Moscoviense (Neumann et al. 2015) and the diameter of Moscoviense drops below 450 km. Conversely, somewhere between 8 and 16 basins of age PN4 or older can be identified. These observations will allow us to distinguish between different lunar cratering chronology scenarios, as we discuss below.

Notably our results do not differ much from Kamata et al. (2015) except for larger error bars and slight differences in the ratio values. The larger error bars arise from a difference in our analysis where we take the mean and standard deviation of the surrounding crustal thickness rather than the mean of the average crustal thickness profile radially around the basin (see above). This means that the error bars describe the range in crustal thickness ratios surrounding the basin. The range of surrounding

crustal thicknesses for older basins is far larger than that of younger basins, a possible consequence of younger events disrupting the thickness of the crust. Additionally, if we take the stance that these doubtful impact structures are not formed by impacts then the relatively sharp transition that Kamata et al. (2015) found becomes slightly muted and the trend through relative time shows a less pronounced transition between relaxed and unrelaxed basins. We still place the switchover at PN4 in this case, but this interpretation of the mean relaxation state transition would imply that our relaxed set of basins formed shortly before the Moho cooled to the critical temperature.

A notable continuation from the Kamata et al. (2015) results, neglecting the "doubtful" basins, is that the Pre-Nectarian 2 and 3 basins have the same approximate relaxation level. This could imply either that these two sub-periods take place over a short absolute time window or that relaxation stalls at some characteristic (highly) relaxed state. Kamata et al. (2015) argue against the latter, as basins can reach relaxation states where they are indistinguishable from the surrounding crustal thickness variations when the Moho is initially above 1400 K. It is more likely that the PN2-3 basins formed in a relatively short timeframe and sample the Moho temperature around 1400 K. We discuss the implications of this clustering in the next and discussion sections.

2.4 The early lunar bombardment timescale

2.4.1 Scenarios for the lunar bombardment history

Based on a combination of Apollo-era absolute geochronology and impact crater counts, several models of the lunar cratering chronology have been proposed (Wilhelms et al. 1987; Hartmann et al. 2000; Neukum et al. 2001; Stöffler et al. 2006; Robbins 2014) (Wilhelms, 1987; Hartmann et al. 2000; Neukum et al. 2001; Stöffler et al. 2006, Robbins, 2014). As we explain below, five representative chronologies are shown in Figure 2.4, which plots the cumulative number of impact basins≥450 km in diameter recorded on the whole Moon as a function of time. These example chronologies can then be compared with the geophysical inferences discussed above to provide further constraints on which scenarios are permissible.

Lunar cratering chronologies are typically reported as densities per area of craters greater than a particular diameter, e.g $N(1)$ or $N(20)$ as a function of time. We use the $N(1)$ version as the starting point for our rescaled chronologies, which required some additional scaling for the chronology based on Morbidelli et al. (2012). These authors used a ratio (∼1400:1) scaling between 20 km and 1 km that we also used. Since we are interested in basins, we need to scale the flux curves appropriately based on an assumed impact size-frequency distribution. The general form of the scaling is a power law, e.g.:

$$N = kX^{-b} \tag{2.2}$$

Here N is the $N(X)$ value for diameter X (where X is the minimum diameter

for the cumulative density), k is the scaling constant and b is the power law exponent that describes the scaling between numbers of different crater sizes. When scaling between the expected frequencies N at different diameter X, k drops out and the ratio will give:

$$N_1 = N_2 \left(\frac{X_1}{X_2} \right)^{-b} \tag{2.3}$$

where the subscripts describe the two diameters chosen. Another way of expressing this concept is that the $(X_1/X_2)^{-b}$ value is the ratio of the number of craters at each diameter.

The ratio of 1 km to 450 km craters is important to interpret the geophysical implications of each chronology. For the rest of the paper b specifically refers to the power of the ratio from 1 km to 450 km. We use a wide range of b values to show the implications for the impact history of the Moon at high and low crater number scaling ratios. We determined this range of ratio values through analysis of various crater distributions and other analytical studies.

The range of crater number scaling values we use is b=2.0, 2.25, and 2.5. Results for each are shown in Figures A.3, 2.4, and A.4 respectively. These b values applied to crater diameters of $\geq$1 km and $\geq$450 km produce ratios of $\sim$2.03x10^5:1, $\sim$9.33x10^5:1, and $\sim$4.30x10^6:1, for b=2, 2.25, and 2.5 respectively.

The low b value (b=2 / Figure A.3) was primarily obtained from a Neukum et al. (2001) study, but the use of the value is common because it generates a horizontal line in Relative plots (e.g. Figure A.1). We also use a higher b value (b=2.5 / Figure A.4) based on the results of Minton et al. (2015). These authors used a Cratered Terrain

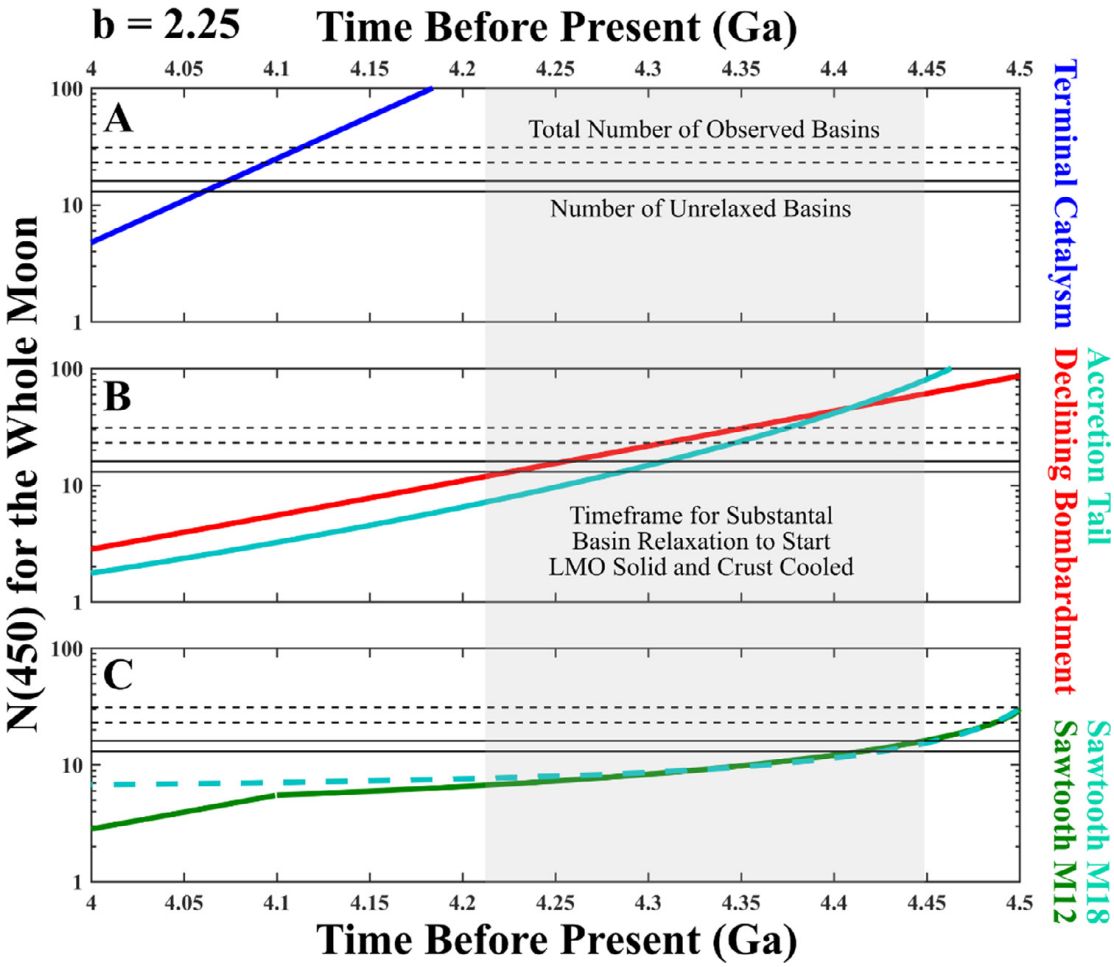

Figure 2.4: A comparison of five lunar cratering chronologies assuming a scaling value of b=2.25 (blue, red, green, and cyan curves), the observed range of the cumulative number of basins that formed after PN4 (black solid lines), the cumulative total number of basins (black dashed lines), and the range of LMO solidification and cooling models (grey box, Section 2.4.2). Chronologies are scaled up from $N(1)$ or $N(20)$ (per km2) to $N(450)$ for the whole Moon. The observed number of basins $\geq$ 450 km, after PN4 is 13–15 and before that time is 8–16 (see Section 2.5.3). Top Panel A – terminal cataclysm an extrapolated scenario based on Robbins (2014). Middle Panel B – declining bombardment scenario based on Neukum et al. (2001) (red) and accretion tail scenario based on Morbidelli et al. (2018) (cyan). Bottom Panel C – two sawtooth scenarios based on Morbidelli et al. (2012) (Solid) and Morbidelli et al. (2018) (Dash). Successful chronologies intersect the solid black lines within the grey box. We include two variations with different b values with Figures A.3 and A.4.

Evolution Model (CTEM) to model the topographic evolution of a heavily cratered surface (like the lunar farside). They found that a number ratio of $N_{>5.5km}/N_{>70km} \sim$ 630 fits the lunar farside better than the modern main asteroid belt. This ratio implies a b value for that set of crater diameters of $\sim$2.5. We assume that this b value will hold at higher diameters, even though the approximate measured shape of the cratering distribution (across most studies, e.g. Neukum et al. (2001) and Werner (2014)) shows that the curve diverges from a simple power law distribution before 450 km. Finally, we also adopt an intermediate value of b=2.25. This value is supported by the Hartmann production function (HPF) (Hartmann 1999) which uses b=2.2 for the power law slope at high crater diameters. After the $N(450)$ values are found, we apply an additional scaling to go from per km^2 to the whole lunar surface, which allows us to calculate the predicted number of craters of a given size forming on the Moon since a given time. The results of the chronology scaling for b=2.25 are presented in Figure 2.4.

Some issues exist with scaling from $N(1)$ to $N(450)$, including that large impacts are rare, stochastic events, and as such can deviate from probabilistic expectations due to small number statistics. Moreover, the shape of the size-frequency distribution may not have been constant with time (Strom et al. 2005; Head et al. 2010) leading to variations in this N(1) to N(450) ratio. Therefore, although an error of $\sim$ N is assumed, the combination of the stochastic, systematic, and observations errors may be large – at least tens of millions of years. In general, however, neither this level of uncertainty nor the uncertainty in which b-value to adopt significantly affects our conclusions (see below).

The curves shown in Figure 2.4 are primarily based on a recent LHB review by Bottke and Norman (2017) in addition to a study by Morbidelli et al. (2018). They represent five examples of proposed lunar cratering chronologies and are unconstrained past 3.91 Ga. The aim of the current study is to use geophysical inferences to provide additional constraints on the proposed chronologies.

The top curve in Figure 2.4 (panel A/blue curve) is an extrapolation of the study performed by Robbins (2014) where he remapped areas previously mapped by Neukum et al. (1975). Robbins based his new counts on images from the Lunar Reconnaissance Orbiter (LRO) Wide Angle Camera (WAC) and found higher crater densities than determined in earlier studies. The higher crater densities obtained by Robbins (2014) imply that the impactor flux was higher in the period shortly after mare emplacement than originally assumed by Neukum. The Robbins chronology is undefined past 3.91 Ga, but we extrapolate out to 4.5 Ga, as was done in Bottke and Norman (2017) to show the effects of assuming a monotonically declining chronology with a higher impactor flux at ∼3.9 Ga. We use the term "terminal cataclysm" to describe this chronology based on Robbins (2014), as Bottke and Norman (2017) did in their review of the LHB, although we note that the original Robbins (2014) chronology is unrelated to the LHB "cataclysm".

Neukum et al. (2001) (panel B/ red curve) is a widely applied standard for the "declining bombardment" scenario where the impactor population for the inner solar system is assumed to be sourced from one population. The shape of the curve is constrained by coupling isotopic dating of samples to observed crater densities (normalized

to $N(1)$) of surfaces sampled by the Apollo and Luna missions. It should be noted that, as the attribution of particular samples to particular surfaces are widely disputed prior to ~3.9 Ga, so all of these models are poorly constrained before that time. The disagreement over whether we have a sample that constrains the absolute age of Nectaris is one of the major sources of this dispute. The $N(1)$ densities were also calculated before modern mapping missions of the Moon.

The next chronology we analyze is based on a study by Morbidelli et al. (2018). The "accretion tail" chronology is a smooth chronology based on dynamical models, similar to the "sawtooth" style chronologies. However, in this chronology, a giant planet instability occurs at 4.5 Ga (not 3.95 Ga or 4.1 Ga). As a result, the shape is closer to the chronology based on Neukum et al. (2001) and is included in panel B (cyan curve). This chronology has a lower $N(450)$ value in the timeframe where the geophysical constraints apply.

With development of dynamical models such as the Nice model (Tsiganis et al. 2005; Morbidelli et al. 2005; Gomes et al. 2005) the idea of a single impactor source population has been questioned. Morbidelli et al. (2012) (Panel C/ Green Curve) designed a lunar cratering chronology based on dynamical models (Morbidelli et al. 2010), where the cratering rate spikes at 4.1 Ga due to a giant planet instability. For ages younger than 4.1 Ga the model matches the Neukum et al. (2001) model (panel B), but for older ages the model has a lower flux and hence lower crater density at a given age. The differential (as opposed to cumulative) chronology function (the impact flux) has a shape like a sawtooth, with a sharp uptick at ~4.1 Ga. Though this model is consistent

(by design) with the Neukum chronology for younger ages, prior to ∼4.1 Ga it is not very well constrained by observations, a gap this study helps to close.

We note that the shape of the Morbidelli et al. (2012) curve was updated in a newer study (Morbidelli et al. 2018). The major change for their sawtooth style chronology in this study is the retiming of the impact spike to 3.95 Ga, whereas in this Morbidelli et al. (2012) the spike occurs at 4.1 Ga. However, the fluxes from the two models nearly match in the interval from 4.5 to 4.1 Ga (which we show in Figure 2.4, panel C) and only greatly differ at younger epochs. As a result, our analysis is unchanged irrespective of which of these two models we use is treated when considering a sawtooth style chronology.

2.4.2 Absolute timing using LMO thermal models and lunar cratering chronologies

Figure 2.3 shows an abrupt transition at the PN4-PN5 boundary between relaxed and unrelaxed basins. Kamata et al. (2015) argued that this transition indicates the time when the lunar Moho drops below 1300–1400 K, which we refer to as t_{cool}. They further argued that thermal evolution models constrained this point in time to 50–100 Myr after the solidification of the magma ocean, t_{solid}. This argument allows us to make a link between the relative timescale, established with crater counts, and an absolute timescale, constrained by flux models and geochronology.

Models for the solidification of the lunar magma ocean depend on the assumed chemical composition and heat input. Both control the time when a floating lid forms,

causing the system to behave as a conductive body rather than radiating directly to space, and the rate that the lid grows. We have decided to use a range of t_{solid} of 10–200 Myr after Moon formation based on the work of Elkins-Tanton et al. (2011) and Meyer et al. (2010), where the former is a model where the LMO solidifies rapidly due to an early mantle overturn inhibiting early crustal lid growth. The latter is a model with tidal heating included in the lid. As a result, the magma ocean must cool through conduction with a warm lid. This results in prolonged cooling of the lid and slowed solidification of the underlying LMO.

To tie model time ranges to an absolute age, we need an estimate for the formation time of the Moon, which comes from isotopic analysis. The primary system used is ^{182}Hf-^{182}W due to the half-life (∼8.9 Myrs) being comparable to the timescales of interest, and the elements having different partitioning behavior (hafnium is a lithophile element, while tungsten is a siderophile element). Kruijer and Kleine (2017) used this system with a suite of lunar samples to determine that the Moon differentiated at least 70 Myrs after solar system formation. This inferred age just barely overlaps with the Barboni et al. (2017) lunar zircons study, which places the formation of the Moon at prior to ∼60 Myrs after Solar System formation. We therefore take the formation of the Moon to have happened at 4.51 Ga, like Elkins-Tanton et al. (2011). We note that the range of solidification and cooling would be shifted earlier or younger linearly based on the formation time assumed. To summarize, if Moon forms at ∼4.51 Ga, t_{solid} is then at ∼4.5–4.31 Ga.

We then subtract an additional 50–100 Myr for the Moho to cool past ∼1300–1400

K (Kamata et al. 2015) to get t_{cool}=4.45–4.21 Ga. Figure 2.3 shows that ∼13 lunar basins >450 km in diameter have formed since t_{cool}. Uncertainties in this number are low because the basins are unrelaxed and thus easy to identify. A maximum of 15 basins can be considered to have formed after PN4. In the interval PN2-PN4, 8–16 basins≥450 km formed, yielding a total of 21–31; this is more uncertain due to difficulties in identifying the most ancient of basins (see Section 2.2 and below).

As outlined in our previous section the lunar cratering chronologies that we used (Figure 2.4) can be described as terminal cataclysm (panel A), declining bombardment (panel B/red) or accretion tail (panel B/cyan), and two hybrid or sawtooth models (panel C/green and cyan). These chronologies represent a range of impactor flux models, including single population models (panel A+panel B/red) and multipopulation models (panel C+panel B/cyan). With extremely high (A) and low (C) overall impactor numbers, the observed basin population (and their properties) should allow us to discriminate between the different models. Figure 2.4 does this comparison graphically; successful cratering chronologies should intersect the solid horizontal lines (representing the unrelaxed basins) in the time window (t_{cool}) represented by the gray box. Table 2.4 shows the timing for the intersection of the chronologies with basin observations.

The terminal bombardment scenario (Figure 2.4 panel A) would require not only the post PN4 basins, but all observed basins to have formed after 4.11 Ga in the b=2.25 scenario. For the observed post PN4 basins and a b value of 2.25, this model gives an age for the transition t_{cool} of 4.06 - 4.07 Ga, which is inconsistent with our geochronological- derived range of 4.21–4.45 Ga. This idea of a high impact rate

around 3.9 - 4.1 Ga has been studied (e.g. Ryder, 2002), but requires every basin to have formed in a brief timeframe, including SPA, and that no basin formed prior to 4.1 Ga was recorded (either because they did not form or were subsequently obliterated). It also requires that basins switch from being relaxed to unrelaxed over a very brief time interval, about 20 Myr. Such a short interval is inconsistent with thermal models indicating progressively decreasing lunar relaxation (Kamata et al. 2015). Varying the assumed value of b does not affect our conclusions regarding this scenario, until the point that b reaches unreasonable values. This chronology shows the issues created by monotonically extrapolating past 3.91 Ga for the Robbins (2014) data.

Neukum et al. (2001)'s standard declining bombardment (Figure 2.4 panel B/red) requires high b values to reconcile with the observations. Assuming a b value of 2.25, this chronology gives an age for the PN4 relaxation switchover of 4.23–4.25 Ga, which just crosses the age range set by LMO solidification and cooling models. If a larger b value of 2.5 is assumed, then t_{cool} has a range of 4.45–4.46 Ga, which is just barely within the inferred switchover time. This would require the shorter timescale for LMO solidification (Elkins-Tanton et al. 2011) and cooling (Kamata et al. 2015). For a b value of 2.25, the onset of basin preservation is at 4.30–4.35 Ga, implying a prolonged interval (∼150–200 Myr) after Moon formation when no basins were preserved to the present. Because we find it more likely that there are 6, rather than 16, relaxed basins, the younger end of the onset of preservation is more likely as well. In this model, the total number of basins formed after 4.5 Ga but not recorded is then ∼50–60. We also find that the Neukum et al. (2001) chronology fails to have enough basin-class impacts

at high b values. This might not be a large problem due to the stochastic nature of large impacts. We further discuss the implications of hiding so many basin-class impacts in Section 2.5.3.

Of the five chronologies, the sawtooth models from Morbidelli et al. (2012; 2018) match the geophysical observations across a broad range of low to intermediate b values. For a b value of 2.25, the relaxation transition happens at the younger edge of ∼4.42 - 4.44 Ga, consistent with the geochronology of a rapidly solidifying LMO and cooling crust. Looking at the other b values, 2 and 2.5, it is evident that this type of chronology is highly sensitive to the ratio of 1 km and 450 km craters. With a b value of 2, the time range for the cooling of the Moho is 4.00-4.02 Ga for the 2012 sawtooth and 3.90–3.91 Ga for the 2018 sawtooth, outside the chronological constraints and more importantly implying that impact basins with a wide range of relaxation states formed during the same timeframe. This is an unlikely scenario (e.g. Kamata et al. 2015). Chronologies scaled by a higher b value (2.5) fail to produce enough basin-class impacts, preserved or otherwise. For the b value of 2.25, the number of unrecorded basins is ∼0–10 which would imply that nearly all basin-class impacts since 4.5 Ga are preserved and observed.

The last chronology we will discuss is the accretion tail model from Morbidelli et al. (2018). The shape of this model is similar to the Neukum et al. (2001) declining bombardment and matches the slope (though not the values) of that chronology at times younger than 4.25 Ga. At b=2.25 the chronology predicts the timing of the relaxation crossover to be 4.29 – 4.30 Ga, which fits inside the geophysical constraints and allows

for prolonged LMO solidification (e.g. Meyer et al. (2010)). At lower b values, this chronology has the same problems as the Neukum et al. (2001) chronology but works across a larger range of intermediate to higher b values than the Neukum et al. (2001) chronology and all other chronologies presented in this study. The lowest b value the Moon can have for this chronology to work (outside of the inclusion of stochastic errors) is 2.15.

Typically, there is a range of b values that allows an individual chronology to fit the constraints we set earlier in this study. Low b values tend to have geochronological events occur late and produce a large number of unrecorded basins (Section 2.5.3). High b values fail to produce enough basin-class impacts or have events occur early. For the sawtooth-style chronologies lower to intermediate b values ($\sim$2.1-2.25) allow these chronologies to fit the constraints laid out previously. For the more continuous-style chronologies (e.g. the Morbidelli et al. (2018) accretion tail model) a wider range of b values can fit the constraints. To distinguish between the individual chronologies further, we will below consider the effects of the late veneer.

2.5 Discussion

2.5.1 Summary

Figure 2.5 summarizes the timeline discussed in previous sections. The Moon forms at 4.51 Ga and at some time between 4.5–4.31 Ga the lunar magma ocean (LMO) solidifies. Basins start to be preserved either right before or at some point after the

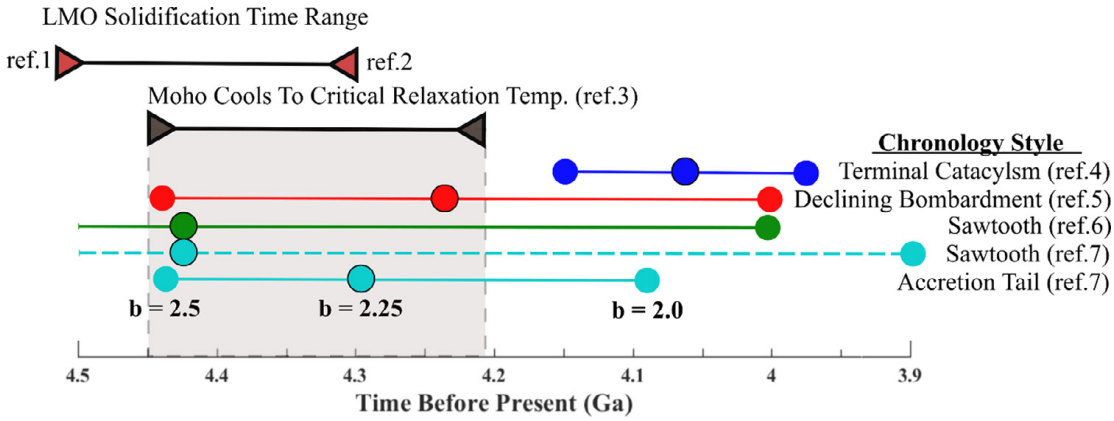

Figure 2.5: Timeline of geophysical events presented in this study. A graphical representation of Table 2.4 in conjunction with LMO solidification age range models (ref. 1: Elkins-Tanton et al. 2011, and ref. 2: Meyer et al. 2010) and Moho cooling models (ref. 3: Kamata et al. 2015). Chronologies ages for the number of unrelaxed basins are shown relative to their coloring in Figure 2.4 (ref. 4: Robbins, 2014; ref. 5: Neukum et al. 2001; ref. 6: Morbidelli et al. 2012, and ref. 7: Morbidelli et al. 2018). Chronologies have to exist within the gray box to match geophysical observations. For example, the Sawtooth chronologies exhibits a high sensitivity to the value of b, and only fits at intermediate to lower b values for the values used in this study.

LMO solidifies (see Section 2.5.4 below). Once the Moho cools below 1400 K, significant basin relaxation ends. Based on thermal evolution models this cooling happens between 50–100 Myr after the LMO solidifies, and is identifiable in the basin record (Figure 2.3).

Of the five lunar cratering chronologies presented in Section 2.4, all but one can explain the observed number of unrelaxed basins and the inferred relaxation transition timing. The sawtooth style chronologies from Morbidelli et al. (2012, 2018) tend to fit the observations at lower b values than the smoother declining bombardment (Neukum et al. 2001) and accretion tail (Morbidelli et al. 2018) style chronologies (which prefer intermediate to higher b values). There are minor differences between the two sawtooth-style chronologies in the period set by our constraints. Between the two

smooth chronologies, the Morbidelli et al. (2018) accretion tail model predicts younger ages for events compared to the declining bombardment unless high endmember b values are assumed.

Table 2.4: Timing of lunar geophysical events.

	t_{cool} N(450)$_{cool}$ = 13-15[a]	t_{solid} (± 20 Ma) N(450)$_{max}$=21-31[a]	N(450)$_{tot}$ at t = 4.5 Ga[b]	LV mass estimate[c]
Geochronology	4.21-4.45 Ga	N/A		
***b* = 2.00**				
Robbins (2014)	3.97-3.98	4.00-4.02	8.6x10^{4}	2.8x10^{22}
Neukum+ (2001)	4.00-4.02	4.07-4.13	400	1.4x10^{20}
Morbidelli+ (2012)	4.00-4.02	4.02-4.22	140	5.2x10^{19}
Morbidelli+ (2018):				
Sawtooth	3.90-3.91	3.90-3.91	140	5.2x10^{19}
Accretion Tail	4.08-4.10	4.16-4.21	1060	3.6x10^{20}
***b* = 2.25**				
Robbins (2014)	4.06-4.07	4.09-4.11	1.9x10^{4}	6.3x10^{21}
Neukum+ (2001)	**4.23-4.25**	4.30-4.35	86	**3.4x10^{19}**
Morbidelli+ (2012)	**4.415-4.44**	4.48-4.5	30	**1.6x10^{19}**
Morbidelli+ (2018):				
Sawtooth	**4.425-4.45**	4.48-4.5	30	**1.6x10^{19}**
Accretion Tail	**4.29-4.30**	4.34-4.38	230	8.2x10^{19}
***b* = 2.50**				
Robbins (2014)	4.15-4.16	4.18-4.21	4080	1.4x10^{21}
Neukum+ (2001)	**4.45**-4.46	N/A	19	**1.2x10^{19}**
Morbidelli+ (2012)	N/A	N/A	7	**8.0x10^{18}**
Morbidelli+ (2018):				
Sawtooth	N/A	N/A	7	**8.0x10^{18}**
Accretion Tail	**4.43-4.44**	4.46-4.48	50	**2.2x10^{19}**

[a] The columns t_{cool} and t_{solid} are the times after the 13–15 unrelaxed basins and 21–31 total basins form, based on different model impactor fluxes (Figure 2.4). For the t_{cool} column, times in bold agree with the inferred constraint of 4.45-4.21 Ga. We put heavier significance on the younger ages for the t_{solid} column due to the doubtful nature of the some of the ancient basins (Section 2.2.1).

[b] The column $N(450)_{tot}$ is the number of basins expected to have formed after 4.5 Ga.

[c] LV stands for the late veneer. The late veneer mass estimate is derived from this $N(450)_{tot}$ value and may be compared with the geochemically-estimated value of 1.47x10^{19} kg (Section 2.5.3). Values in bold fall within a factor of 2 of the estimated value.

2.5.2 Hemispherical/Latitudinal variations

Hemispherical variations in many lunar characteristics have been noted previously, including diameter of basins (Miljković et al. 2013) and thorium and uranium concentrations (Korotev 2000). These factors may be related to the asymmetrical thermal evolution of the Moon (Laneuville et al. 2013), with the nearside having a higher temperature crust. Miljković et al. (2013) showed that an impactor creates a larger final basin if a KREEP layer exists under the crust.

We observe the same hemispherical difference in diameter as seen in Miljković et al. (2013) (Figure A.2), but we do not observe any other significant dichotomies between hemispheres or regions. This observation may be contrasted with the substantial change in the mean relaxation state around PN4. We also do not see any difference in the crustal thickness ratio between nearside basins inside and outside the PKT, despite the expectation that higher heat fluxes would increase the rate of viscoelastic relaxation (Solomon et al. 1982; Kamata et al. 2013). One possible explanation for this lack of variation could be that there is a trade-off: a higher heat flux could offset the effect of a thinner crust on the channel thickness δ (Eq. 2.1) and thus the relaxation timescale.

2.5.3 HSEs and the maximum number of basins

Our analysis (Table 2.4) implies that, at a minimum, tens of basin forming impactors struck the Moon without leaving any visible record in an interval from 4.5 Ga to the start of basin preservation. Proposed basins like Topo-22 are only marginally identifiable; basins that formed earlier are likely to be unidentifiable at the present day.

Numerical models that simulate large impacts into the growing lunar crust overlying a magma ocean (Miljkovic et al. 2017) confirm that such basins are unlikely to be identifiable. These basins start in a relaxed state and can easily relax further due to the high crustal temperatures (Kamata et al. 2015).

Fortunately, these impacts also produce geochemical imprints that can be detected and allow the number of missing basins to be quantified. To do so, we use inferences of the late veneer (the extra mass accreted by a planet after core formation ceases) (Day et al. 2007; Bottke et al. 2010; Day and Walker 2015). A similar approach was used by Morbidelli et al. (2018) to compare various chronological models produced from numerical N-body simulations.

We estimate the amount of mass that was delivered to the surface by the known set of basin-class impacts and compare it to studies (Day and Walker 2015) that derived the total mass delivered during the late veneer. Day and Walker (2015) obtained a value for the late-accreted mass of $\sim$1.47x10^{19} kg by looking at concentrations of highly siderophile elements (HSEs) in Apollo samples. Lunar core formation is presumed to have scavenged all pre-existing HSEs from the mantle; since core formation probably took place immediately after Moon formation, the impacts we are considering should all have contributed to the present-day mantle HSE budget. We can assume this because even under the shortest case of LMO solidification and crustal cooling, 50 Myr should have elapsed. Rubie et al. (2016) looked at FeS segregation as the primary mode for HSEs sequestration into the core. They found that FeS segregation ends at 50–70% of LMO solidification. Both of the end-member LMO solidification models we use in this

study have ∼80% of solidification within ∼10^5 years; as a result, all the impacts we are interested in should post-date the end of core formation.

Now we have to make a set of assumptions to derive the amount of mass delivered. We assume (1) that ∼50% of the projectile escapes from the system – either through evaporation or ejection (Artemieva and Shuvalov 2008), (2) the mean impactor density is ∼2.5x10^3 kgm^{-3}, (3) that accreted material is well-mixed into the mantle, and (4) that the material is CI chondritic. We also tested two different projectile-crater scaling laws, including a simple 10:1 projectile to-final-crater diameter ratio, and a scaling equation from Johnson et al. (2016). Additionally, we focus on the 21+SPA basin set with GRAIL Bouguer gravity evidence (Neumann et al. 2015) instead of the total 31 basin set. If we use the 22 (21 plus SPA) basin set, the mass delivered by the impactors forming the set of observed basins has of values of 8.21x10^{18} kg for the 10:1 scaling and 9.87x10^{18} kg for the Johnson et al. (2016) scaling. While the number of ≥450 km basins in this scenario drops by about a third compared to the 31 basin case, the mass estimate is only ∼20% lower. This is an effect of the GRAIL-derived basin distribution having a relatively higher number density at larger diameters. We note that the late veneer mass we obtain from both scaling equations is dominated by the largest basin impacts. This is true for all cases where the b value is <3. For the Moon, SPA dominates the mass. Our impactor diameters for SPA are 205 km and 235 km for the 10:1 and Johnson et al. (2016) scaling respectively and we get ∼50–60% of the total mass represented being delivered by SPA. These diameters are both larger than the 170 km derived from Potter et al. (2012)'s best-fit iSALE hydrocode models. The

source of this discrepancy is likely that the scaling equations overestimate the size of impactors for basins whose formation is greatly affected by the curvature of the body. To be conservative, below we will use the 10:1 scaling, but note that a large amount of uncertainty exists regarding the size of the SPA impactor.

We wish to calculate the total mass delivered after Moon formation for the different scenarios summarized in Table 2.4. To do this we need to make a few assumptions, mainly concerning the shape of the CSFD and the anomaly of SPA. We assume the CSFD takes the form of a simple power law function and that b is constant in time, so that the size-distribution of basins has stayed constant. This implies that the mass accreted is linearly related to the total number of impacts. Strictly speaking, this is true only in the limit of a large number of impacts, so there is a stochastic component; however, since we are mostly interested in order-of-magnitude scale effects, this simplification should not matter. One factor that has a minor effect on the estimated mass is the question of whether SPA is an anomalous basin or is a part of the size frequency distribution. The inclusion of SPA-class impacts in the distribution increases the total mass by 30–50% when the number of basins is increased to ∼60 total basins. Yet, without concrete evidence of another SPA-class basin in topographic or gravity data, we do not include SPA in the CSFD for our mass estimates in Table 2.4 and add in the mass from SPA as an additional step. It is currently unknown if SPA-class impacts would necessarily leave geophysical or morphological evidence if they occur at ages older than SPA (e.g. Jutzi and Asphaug 2011). We display our total mass estimates in Table 2.4 for each chronology for various b values. It is evident that the extrapolated Robbins

(2014) curve delivers far too much mass to be consistent with the estimated late veneer.

Based on the inferred late veneer mass, the total number of basins expected to have formed after ∼4.5 Ga is in the range 30–80. This may be compared with the predicted numbers of basins formed for the various scenarios shown in Table 2.4. The extrapolated Robbins (2014) based chronology predicts on the order of 10^4 basins ≥450 km in diameter, which is far above the 30–80 basins predicted by HSEs. The other chronologies we use in this study tend to under-produce basins at higher values of b while overproducing at lower values relative to the estimated number.

The sawtooth style chronologies (Morbidelli et al. (2012, 2018)) at b=2.25 match the lower end of our estimation (∼30). This fits well with the geochronological constraints that imply that this style of chronology favors lower values of b (∼2.1–2.25). The smoother styles of chronologies prefer intermediate to high values of b. The chronologies based on Neukum et al. (2001) and Morbidelli et al. (2018) continue to fit at the maximum value of b (2.5) used in this study.

This late veneer analysis places limits on how many missing basins there could be. However, it is important to understand how sensitive the results are to the assumptions we made. For example, we assumed that the accreted material is well-mixed into the mantle. While this is a solid assumption for smaller, undifferentiated asteroids, it may not hold for larger, differentiated bodies (Marchi et al. 2018). SPA, the only basin in our catalog that was formed by a projectile with a radius > 100 km, is the most likely candidate to have been formed by a differentiated impactor; smaller impactors are unlikely to have been heated by ^{26}Al sufficiently to cause differentiation (McCoy

et al. 2006). With the largest impacts causing less of an effect on HSE concentrations in the mantle than we assume, this would allow an extra SPA-sized projectile to accrete without violating the observational constraints.

When and at what scale impacts fail to mix their mass into the lunar mantle is a possible additional complication. Bottke et al. (2010) place the end of late accretion when the lunar crust has formed, which is within the tens of million years after core formation. They argue that most of the HSEs in both the terrestrial and lunar mantles must have arrived before this time. Although this may be too strict an assumption, especially in the case of a tidal-heat-prolonged LMO (Meyer et al. 2010), the youngest basins in our catalog might not be able to mix their mass as efficiently into the mantle as we assume earlier. This would further push the total number of possible basin-class impacts upwards.

Another issue that we do not pursue is the fact that the same impactor will produce a larger basin on the (warmer) nearside than the (cooler) farside (Miljković et al. 2013). Miljkovic et al. (2013) find an increase in diameter of around 60% comparing simulations of impacts into nearside versus farside crust. This would imply that the simple basin to impactor diameter scaling for the nearside in and around the PKT terrain is 16:1. This would make a difference of around 50% to the mass for the non-SPA basins (3.7×10^{18} kg delivered without SPA). Such a difference would result in a total delivered mass of 50–75% of the non-SPA mass we calculate above.

2.5.4 Timing for basin retention

In our survey of the Bouguer gravity map produced by the GRAIL mission, we failed to find any new circular positive gravity anomalies compared to Neumann et al. (2015). Any feature above ∼80% relaxed is indiscernible given background variations in the Bouguer gravity field, such as those caused by cryptovolcanic features (Sori et al. 2016). Since the Neukum et al. (2001) model coupled with our geophysical calculations predicts an interval of ∼150 Myrs when no basins are retained, it is important to investigate further how basin retention works.

We use the term basin retention to refer to the time when signals of basin-size impact craters can be preserved to modern day. Basins formed prior to this time will relax past ∼80% and blend in with the background crustal thickness variations. That time likely begins before t_{solid}, but the exact timing is currently not well defined. Hydrocode models have recently been constructed to replicate an asteroid impact into an early crust overlying a layer of partially or completely molten material (Miljkovic et al. 2017). They find that as this molten layer shrinks (solidifies) there exists a critical melt thickness (∼10–15 km); below that thickness the initial basin morphology is unrelaxed, and the impacts are unaffected by the remaining melt. Basins formed at or after this point would be expected to survive, albeit in a relaxed and partly obscured form.

We can estimate the timeframe for the last 10–15 km of solidification (when the crust thickens from 30 km to 45 km) using the Stefan solution, which solves for the propagation of a phase boundary. The Stefan problem is outlined in Turcotte and

Schubert (2002) and takes the form:

$$t = \frac{d_f^2 - d_i^2}{4\lambda^2\kappa} \tag{2.4}$$

Here t is the time it takes for the phase boundary to propagate from the initial crustal thickness d_i to the final thickness d_f given a non-dimensional constant, λ, and the thermal diffusivity of the upper layer, κ. The non-dimensional constant, λ, depends on the temperature difference over the solid layer, the latent heat of fusion, and the specific entropy. For the final solidifying layer, we use $\lambda \approx 0.88$ and $\kappa \approx 10^{-6}$ $\mathrm{m^2s^{-1}}$. We find that solidifying the last 10–15 km of melt should take ∼10 Myr, which when combined with the ∼50–100 Myr needed for the crust to cool past the critical relaxation temperature (Kamata et al. 2015) gives ∼60–110 Myr as the likely interval between the onset of recorded (but relaxed) basins, and the onset of unrelaxed basins. We call this interval Δt_{EPN}, where EPN stands for Early Pre-Nectarian.

This predicted interval can be compared with the results predicted from the different chronology curves (Figure 2.4). In Table 2.4, the time when the onset of recorded basins occurs is given in the $N(450)_{max}$ column and the onset time of unrelaxed basins in the $N(450)_{cool}$ column. The difference between these two columns is Δt_{EPN}. The shorter end of the timeframe is set by the maximum number of basins formed after PN4 and the minimum total number (i.e. excluding the transparent squares in Figure 2.3) and the longer end is set by including all basins in Table 2.1. We give higher weight to the likelihood of a shorter timeframe because the stronger set of basins excludes the doubtful group with no Bouguer gravity signal, implying a later preservation starting

date for impact basins.

The chronology based on an extrapolation of Robbins (2014) gives Δt_{EPN} ∼20–50 Myr, a brief time for all the preserved early Pre-Nectarian basins to have formed compared with our Stefan solution. The chronology based on Neukum et al. (2001) predicts a Δt_{EPN} ∼50–120 Myr. The accretion tail model (Morbidelli et al. 2018) has a similar Δt_{EPN}, ∼40–90 Myr. Both ranges fit within the Stefan solution framework. If these epochs were long, it would imply that either the cooling period was prolonged (e.g. by tidal heating) or that basins could survive to the present even when formed on thin crusts.

Morbidelli et al. (2012)'s sawtooth model gives a range of ∼40–85 Myr for Δt_{EPN}, which is on the low end of our Stefan timescale. The Morbidelli et al. (2018) sawtooth model gives a similar timeframe of ∼35–75 Myr. This is driven by the high initial slope of the sawtooth models. On the other hand, the sawtooth models do not require a prolonged epoch before the onset of basin preservation, and also readily explains the relative abundances of unrelaxed (post-PN4) and relaxed (PN4 or older) basins.

2.5.5 Elusive ages for Asperitatis and Fecunditatis

With the change in the mean relaxation state that divides the early pre-Nectarian from younger basins, we have another rough check to determine the approximate age of large lunar features. By combining the crustal thickness ratio with stratigraphy, we can constrain the ages of proposed basins to within a range of a few

relative age units. The crustal thickness ratio for Asperitatis is 0.47±0.09. This value would place it within the unrelaxed group (ratio<0.6) and would imply that the impact occurred shortly after the LMO solidified and the Moho cooled past 1400 K. This combined with the stratigraphic evidence would place Asperitatis as forming in the late Pre-Nectarian over earlier in the same period. We include Asperitatis in the upper range of basins that formed during or after the late pre-Nectarian in our previous sections. Fecunditatis has the lowest crustal thickness ratio in the early pre-Nectarian group (#15 in Table 2.1/Figure 2.3). The basin's relative age remains elusive, but the relaxation state of the feature implies that it may be younger than previously thought. This technique may provide a tool for studying the age of large-scale features on terrestrial bodies where we understand the evolution of the thermal state. On the Moon, this could be useful due to the unconstrained nature of the early eras of the lunar surface.

2.6 Conclusions

GRAIL gravity data have revealed and characterized new lunar impact basins. We have applied crater counting techniques in order to find relative ages for these ancient proposed basins. The proposed basins based on gravity data (Neumann et al. 2015) for which we achieved crater counts are all older than PN4.

Using a variation on the methodology used in Kamata et al. (2015), we characterized the relaxation state of all basins ≥450 km. We observed the same trend of decreasing relaxation with decreasing age, with a notable change in the mean relaxation

state around PN4 (Figure 2.3). This implies that the thermal state of the Moho passed a critical temperature (1300–1400 K) around PN4.

We then compared the number of unrelaxed basins to estimates based on magma ocean solidification timescales (from geochronology) and different impactor flux models (Section 2.4.2, Figure 2.5). Of the five chronologies we used, the Morbidelli et al. (2012, 2018) sawtooth chronology fits best when we assume a smaller ratio of 1km:450 km craters for the lunar surface (b=2.25). The Neukum et al. (2001) and the Morbidelli et al. (2018) accretion tail chronologies also fit our constraints, especially when assuming a larger ratio of 1km:450 km craters for the lunar surface (b=2.5). Both the Neukum/accretion tail and sawtooth chronologies match tcool. If the actual value of b is between 2.15 and 2.25, then the sawtooth chronologies provide the best fit to the estimated late veneer mass; the Neukum and accretion tail chronologies produce too massive a late veneer (Section 2.5.2, Table 2.4). Future lunar crater chronologies will have to take the limited number of basins that formed after PN4 and the mean relaxation state of these basins into account.

Chapter 3

An upper bound on Pluto's heat flux from a lack of flexural response of its normal faults

This chapter is a slightly modified reprint of work previously published as Conrad, J. W., F. Nimmo, P. M. Schenk, W. B. McKinnon et al. (2019) "An upper bound on Pluto's heat flux from a lack of flexural response of its normal faults." Icarus 328, 210-217

Abstract

The topography of rifts on icy bodies can be used to probe their internal properties. Uplifted and curved rift flanks occur when the elastic thickness (t_e) of the crust is low, indicative of high heat flow out of the body. Stereo topography of Pluto

shows no evidence of rift-flank uplift associated with large extensional graben to the west of Sputnik Planitia. Modeling the amount of topographic deflection expected from varying elastic thicknesses yields a conservative lower bound on t_e of 8 km at the time of deformation; the maximum implied heat flux since graben formation is 66–85mWm^{-2}. This upper bound is consistent with the predicted paleo-heat fluxes from radioactive decay ($\sim$6mWm^{-2}), but likely only marginally consistent with nearby apparently viscously-relaxed impact craters. Additionally, we also analyze the shear stresses on these faults and find that Pluto's faults only need to support low stresses in the range of 100–300 kPa to explain their dimensions.

3.1 Introduction

Constraining the thermal history of Pluto is important to understanding the formation and evolution of differentiated Kuiper Belt objects (KBOs). One way of constraining a planet's thermal history is to look for signs of elastic flexure of the lithosphere, which can then be used to infer the maximum heat flux since the time of deformation. That is the approach we take in this paper, using the loads imposed by extensional grabens.

When the *NewHorizons* probe visited Pluto in 2015 the first high resolution images of Pluto's surface revealed a complicated world showing a variety of features and processes (Stern et al. 2015; Moore et al. 2016). The encounter hemisphere is dominated by a large depression named Sputnik Planitita (SP). While the interior morphology

of Sputnik Planitia suggests processes are currently modifying the surface of Pluto (McKinnon et al. 2016; Trowbridge et al. 2016), the exterior regions record a more prolonged history. The bladed terrain of Tartarus Dorsa (east of SP) suggests the likely involvement of sublimation and deposition of CH_4 ices on the evolution of Pluto's geology (Moore et al. 2018). Regions to the north of SP (i.e. Voyager and Pioneer Terra) have likely been modified by deposition of CH_4 ices (Moore et al. 2016). Large extensional grabens are also observed in the area east of SP (e.g. Sleipnir and Sun Wukong Fossae), but the limits of topographic resolution and the degree of geologic modification have driven us to focus on the extensional graben in the regions west of SP, where there has been comparatively little degradation (Moore et al. 2016).

The stresses generated by large extensional grabens have been used to analyze the conditions of the near-surface crust of a variety of worlds, including Earth (e.g. Kusznir et al. 1991; Brown and Phillips 1999), Venus (e.g. Johnson and Sandwell 1994; Foster and Nimmo 1996), Mars (e.g Barnett and Nimmo 2002), Europa (e.g. Nimmo and Schenk 2006), Ganymede (e.g. Nimmo et al. 2002), Tethys (Giese et al. 2007), Enceladus (e.g. Giese et al. 2008), Ariel (Peterson et al. 2015), and Charon (Beyer et al. 2017). The flexural rift flank response (i.e. the amount that the topography at the edge of the rift is lifted above the surrounding elevation) as a result of the imposed negative load can be used to determine the characteristics of the crust. Primarily, we can estimate the depth to which the crust acted elastically (i.e. the elastic thickness) at the time of deformation, and how rapidly heat was lost through the crust (i.e. the heat flux). In our analysis, we will show that the minimum elastic thickness implied by the topographic

expression of Pluto's extensional graben is ∼8 km and the associated maximum possible surface heat flux since graben formation is ∼66–85mWm^{-2}. This is a conservatively high estimate, as it neglects the effects of layers of reduced thermal conductivity due to porosity (Giese et al. 2008) or volatile ices and should be interpreted as an upper bound; the expected radiogenic heat flux at the time of deformation is ∼6mWm^{-2} (see below).

3.2 Observations

There are two large extensional graben each in Viking Terra and Cthulhu Regio (4 total; Stern et al. 2015) that have widths on the order of 20 km, maximum throws ranging from 1.0 to 2.4 km, and lengths between 400 and 600 km. While other normal faults exist in these areas, the topographic expression of these other faults (e.g. their trough depths and flank dimensions) are close to an order of magnitude smaller and most are near the limit of the topographic resolution (∼300 m/px). Smaller faults are additionally less sensitive probes of the elastic thickness, because it is easier to support their negative topography with material strength (Turcotte and Schubert, 2002). For these reasons, we are focusing this study on the major four faults of Inanna and Dumuzi Fossae (Viking Terra) and Virgil and Beatrice Fossae (Cthulhu Regio). The surrounding topography near each fossa, the chosen profile line locations, and their location in Viking Terra and Cthulhu Regio are shown in Figure 3.1. The derived topography of these profiles is shown in Figure B.1, where trends along fault strike can be observed.

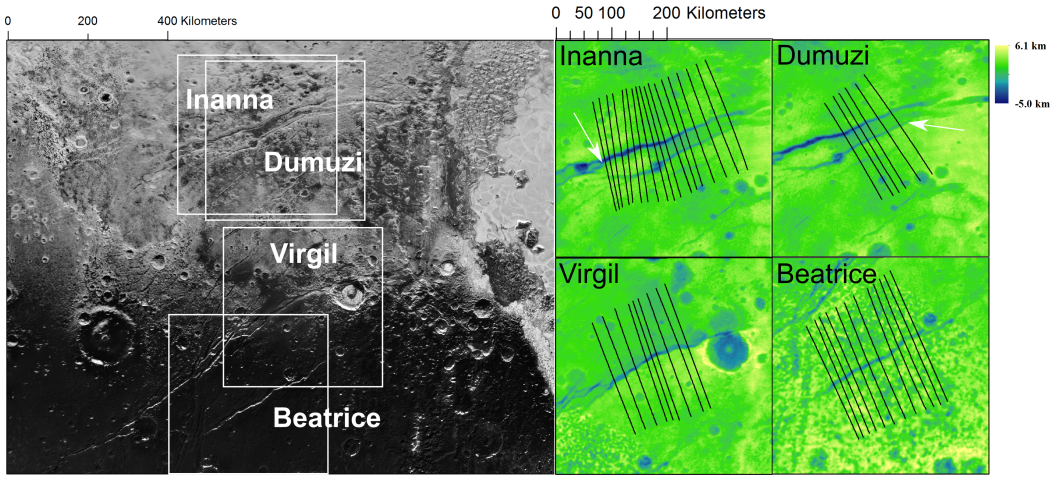

Figure 3.1: Image and topographic maps of large faults in Viking Terra and Cthulhu Regio, west of Sputnik Planitia. Left: Locations of maps on the right. Right: Topographic maps (Schenk et al. 2018a) of fault sections with chosen profile line locations.

We use the digital elevation model (DEM) from Schenk et al. (2018a), which for the analysis area has a $\pm$ $\sim$100m stereo height accuracy and a ground sample distance of $\sim$300 m/pixel. While not in the highest resolution area, the Viking terra and Chtuhlu regio appear in high enough resolution to allow a reasonably complete analysis. Although the DEM covers only $\sim$42% of the total surface, it covers nearly our entire analysis area with the only gaps occurring at the western termini of Virgil and Beatrice Fossae. Schenk et al. (2018) calculated the DEM through sets of stereo images from the MVIC hemispheric scans and LORRI mosaics. Since 5x5 pixel patches were used for each DEMpixel, we take some care to check for possible smoothing effects from the DEM creation process. This smoothing effect should be smaller than the smoothing effect from averaging profiles (see below).

Cratering statistics could be of use in determining the relative age of these faults. However, ages of features on Pluto calculated from crater statistics have issues deriving from variable lighting angles and active geology (Moore et al. 2016). Even so, using cratering models from Greenstreet et al. (2015), Moore et al. (2016) found that the surface ages of Viking Terra and Cthulhu Regio are ∼4 Ga. It should be noted, however, that the dating models have large uncertainties due to the unknowns in the crater production rate at Pluto's orbital distance (Greenstreet et al. 2015). In some places, such as in the case of a minor fossa (127.9° longitude, 21.2° latitude) in the middle of the major sets, a crater overprints a fossa, but more often a fossa cuts across a pre-existing crater (the eastern end of Virgil Fossae, for example). This implies that these fossae formed at times younger than ∼4 Ga, but are likely still older than features on most of Pluto's other regions (e.g. washboard terrain (Moore et al. 2018) and the convecting nitrogen ice cells in SP (Stern et al. 2015)). The likely age for the start of fault formation is approximately consistent with thermal model estimates of the beginning of Pluto's expansionary period at around 2.5 Ga, i.e. when its ice shell began to thicken (e.g. Robuchon and Nimmo 2011; Hammond et al. 2016; Bierson et al. 2018). We only analyze sections of the faults with little evidence for post-formation disruption.

We determine an average topographic profile for each of the four fossae by first calculating perpendicular great circle lines to chosen locations along the strike of the fault. We purposely choose locations along the center-line where there are no nearby large craters or features orthogonal to the fault strike. For example, at the eastern terminus of Inanna and Dumuzi Fossae, a shallow, unnamed fossa strikes in the

intermediate space between the two fossae. However, if an intervening feature cannot be avoided, as in the case of Inanna Fossa's northerly location with respect to Dumuzi Fossa, we use center-line points where the other fossa in the pair shows up in the profile. After we have the center-line points, two positions five degrees north and south along the great circle perpendicular to the strike of the fault are calculated. Using the three points (center-line point and north/south maxima) we calculate topographic profiles along the great circle path between those points using the software ArcMap. In the case of the profiles in Figure 3.2 our resolution is 0.05° (∼1 km). Before we calculate the average profile for a fault, we de-trend each profile. To de-trend the profiles we first remove any linear trend across the trough based on the slope between the average height of points at each end of the profile. Once this is done we set the endpoints of the profile to datum (or as close as the cross-strike de-trending allows); this ensures that the average trough depth is not muted or exaggerated due to long wavelength changes in the fault depth along strike relative to the datum. We note that changes in fault depth along strike will factor into the averaging with the resulting profile representing a compromise between the shallower and deeper profiles. However, since Inanna Fossae is the only fault with major changes in trough depth (reaching an additional 0.5 km deeper in its deepest sections relative to the average – see Figure B.1) this effect is unlikely to be very important. The resulting averaged profiles and the standard deviation are presented in Figure 3.2.

Generally, the fossae of Inanna and Beatrice share similar dimensions when their average profiles are considered (Figure 3.2). They are both E-W trending with

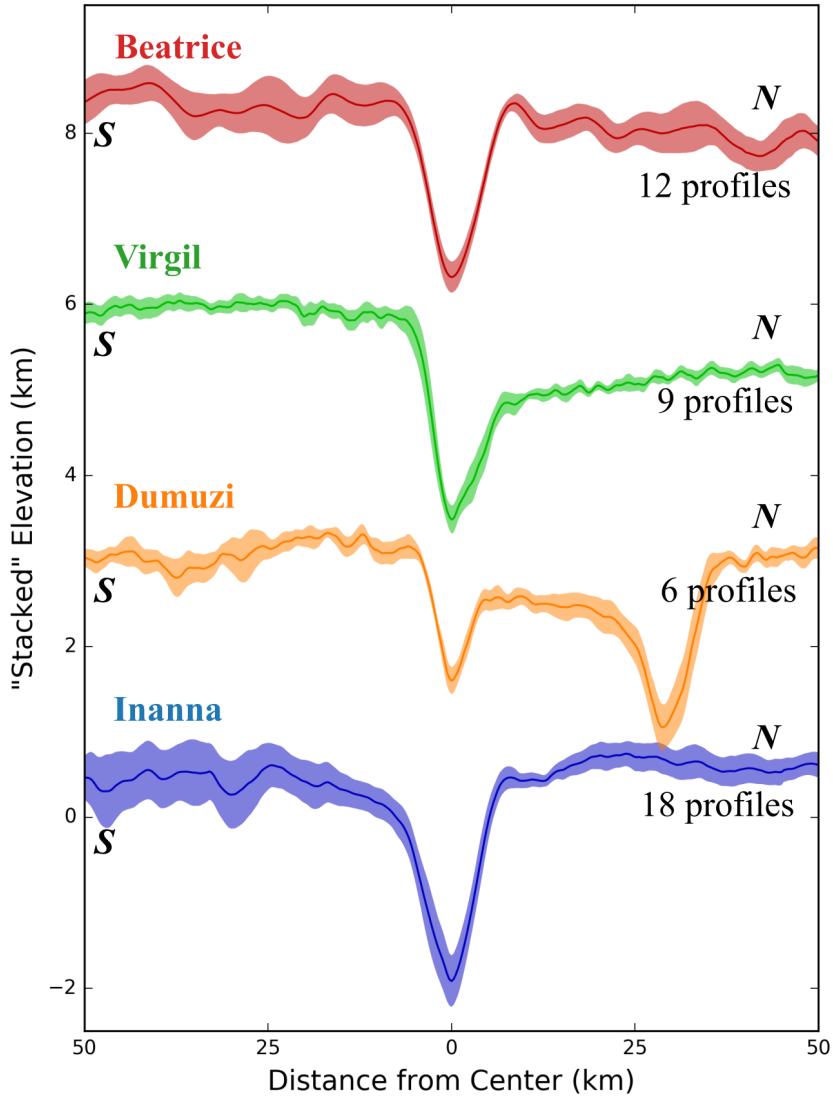

Figure 3.2: Comparison of averaged fault profiles. Profiles are vertically offset for clarity and there is ∼17x vertical exaggeration. These profiles are generated using the same technique described in the text but the segments here are 100 km (∼5°) in length rather than the 10° segments used for comparison with topographic models. Inanna, Beatrice, the southern half of Dumuzi, and the northern half of Virgil all show similar forms. The northern side of Dumuzi is dominated by the deeper and longer Inanna Fossa, while Virgil shows a possible half-graben behavior (also noted in Schenk et al. 2018a).

moderately symmetrical faulting and the flanks show little to no flexural uplift. The ratio of vertical offset to half-width is ∼1:5 for both fossae. This gives an "apparent" fault dip of around 11–12°. Fault dip angles for terrestrial normal faults are typically above 45° (Jackson and White, 1989); lower angles on terrestrial worlds typically implies that mass-wasting events have occurred. However, the actual graben profile can be observed in the images and DEM. In the images it becomes clear that there are sections of flat floors in every large graben, which are not resolved as clearly along the whole strike of each fossa in the DEM. We can use the images (Figure 3.1) to determine the exact distance over which the dip occurs, rather than estimating them through the DEM. By using the images to determine the horizontal extent of the fault surface and using the DEM to determine the vertical offset we can derive a more accurate dip angle. From a few locations along the strike of Inanna Fossae where we observe a flat floor in the images, the dip angle we calculate is ∼51±4°. This value better matches normal fault angles observed on other icy worlds (Kadel et al. 2000) and is also consistent with the expected dip angle based on the measured friction coefficient of ice at low temperatures (Beeman et al. 1988; Turcotte and Schubert 2002).

Dumuzi Fossa is the smallest of the four faults we study. It is approximately 1 km deep and about half as wide as Inanna and Beatrice Fossae. The ratios of vertical offset to half-width are still around 1:5 and the fault dip angle is likely also the same as Inanna and Beatrice Fossae. The profile of Dumuzi is also complicated by Inanna Fossa to the north so its southern flank is our focus. Because we are more concerned with why these structures show no apparent flexural uplift - which is easier to achieve

with smaller features - we place more weight on the results derived from analysis of the other three major faults.

The eastern section of Virgil Fossa displays differing geometry from the three other fossae. Most notably the southern flank ridge of Virgil is ∼1 km higher in elevation than the northern flank ridge (Moore et al. 2016; Schenk et al. 2018a). The structure implies that Virgil Fossa is a half-graben, or at least started out as a half-graben and is in an intermediate state. This asymmetry also exists in the dip angles; we can use the same method as we used for Inanna and Beatrice Fossae to estimate dip angles based on the images. We get a fault horizontal extent of around 1.0±0.1 km, and with a throw of ∼2.2±0.2 km, the dip angle is ∼66±3° for the southern flank. For the northern flank a similar horizontal extent with a throw of ∼1.5±0.2 km gives a dip angle of ∼55±3°.

Using the dip angles, we can calculate the displacement to length ratio (D/L), a useful value for comparing faults across different Solar System worlds (Nimmo and Schenk 2006; Schultz et al. 2006). To find a characteristic D/L for Pluto's faults we look at our high dip angle estimates from images for our largest fossae. For Inanna Fossa we estimate a D/L of 0.006 and for southern Virgil Fossa we estimate a D/L of 0.004. This is lower than values for terrestrial faults (∼0.01; Schultz et al. 2006), but is more in line with values found for martian faults (∼0.005; Schultz et al. 2006).

3.3 Methods and results

3.3.1 Deflection

In general, a load applied to an elastic plate will result in flexural deformation with a characteristic wavelength given by the flexural parameter, α. If this wavelength can be measured, an elastic thickness can be inferred (e.g. Turcotte and Schubert, 2002). In our case, however, no clear rift-flank deflection is observed (Figure 3.2). If rift-flank deflection was present the flanks of the graben would curve and rise above the surrounding topography. This lack of uplift suggests that the lithosphere is sufficiently rigid to prevent observable deflection, in which case only a lower bound on elastic thickness can be derived. We use the plate deflection method as used in Barnett and Nimmo (2002) to estimate the minimum elastic thickness at the time of fault formation. Their method is based on the method of McKenzie and Bowin (1976), assuming an unbroken and thin plate. A broken plate would yield a larger minimum elastic thickness, so our approach is conservative. We also neglect the role of membrane stresses, which is appropriate given the short wavelength of the load compared to the planetary radius. The deflection in the frequency domain, $X(k)$, from a load of thickness $S(k)$, on an elastic plate is given by:

$$X(k) = \frac{-S(k)\rho_c}{(1 + C_1 k'^4)\rho_m} \tag{3.1}$$

in which

$$C_1 = \frac{2EM_\mu}{3\mu(1-\nu^2)} \tag{3.2}$$

$$k' = \left(\frac{t_e}{2}\right)k \tag{3.3}$$

$$M_\mu = \frac{2\mu}{g\rho_m t_e} \tag{3.4}$$

Here k is the wavenumber, ρ_c is the load density, ρ_m is the density of the "upper mantle", E is Young's modulus, t_e is the elastic thickness, g is the gravitational acceleration, μ is the rigidity (equal to $E/2(1+\upsilon)$), and υ is Poisson's ratio. The parameters with their values or range in values are presented in Table 3.1.

Table 3.1: Parameters used in chapter 3.

Parameter		Value	Source
g	Surface acceleration due to gravity	0.62 ms^{-2}	Stern et al. (2015)
ρ_c	Load density	930 kgm^{-3}	
ρ_m	Density of the upper "mantle"	930 kgm^{-3}	
E	Young's modulus	9 x 10^9 Pa	Gammon et al. (1983)
υ	Poisson's ratio	0.3	Gammon et al. (1983)
Q	Activation energy	60[a], 49[b], 60[c] kJ/mol	see below[d]
n	Stress parameter	2.4[a], 1.8[b], 4[c]	see below[d]
A	Material parameter	a:5.5x10^7 $MPa^{2.4}$/s b:3.9x10^{-3} $MPa^{1.8}m^{1.4}$/s c:4.0x10^{-5} MPa^4/s	see below[d]
p	Grain size parameter	0[a], 1.4[b], 0[c]	see below[d]
R	Gas constant	8.315 $JK^{-1}mol^{-1}$	
De	Deborah number	10^{-3}-10^{-4}	Mancktelow (1999)
μ	Rigidity modulus	3.46 x 10^9 Pa	μ=$E/(2(1+\upsilon))$
d	Grain size	0.1-10 cm	Barr+McKinnon (2007)
T_s	Surface temperature	40 K	Stern et al. (2015)
κ	Thermal conductivity of pure H_2O ice	567/T Wm^{-1}	Klinger (1980)

[a] Basal slip-accommodated grain boundary sliding (GBS) regime.
[b] GBS-accommodated basal slip regime.
[c] Dislocation creep regime.
[d] Goldsby and Kohlstedt (2001).

For the load (which is negative, leading to uplift) we constructed a simplified profile that has a similar shape as the averaged Inanna Fossa profile. We used a 2.44 km deep and 24.5 km wide cosinusoidal trough (i.e. a trough in the shape of half a cosine wavelength) as our load for Inanna with the same resolution as our topographic profiles. Other load geometries were tested for Inanna with the same width and depth, and neither a boxcar load nor a triangular load (which are the two end members) created an appreciably better result and did not match the fault geometry as well as the cosinusoidal trough. Our use of the cosinusoidal trough is based on its use by Barnett and Nimmo (2002) and the shape can be observed in Figure 3.3 as the elastic thickness increases. The cosinusoidal load geometry can also be scaled to match Dumuzi and Beatrice Fossae by changing the depth and width to match their observed geometries. Figure 3.3 shows how the resulting model topography (load + response) compares with observations for Inanna Fossae. The analysis for the other three fossae is included in the supplemental (B.2)). For all fossae, at low elastic thicknesses significant model rift flank uplift occurs, which is not observed in the topographic data. As the elastic thickness increases, the rift-flank uplift becomes smaller, until at t_e=10 km the model topography matches the observations quite well and further increases produce no significant change in result. To quantify this effect, the elastic thickness (t_e) is varied over a range from 1 km to 60 km and the χ^2 misfit between the model and observed topography outside the trough is calculated for each t_e value.

For the other three fossae we used differing trough geometry to better fit the results of our models. We altered the model load topography to 1.2 km and 1.9 km deep

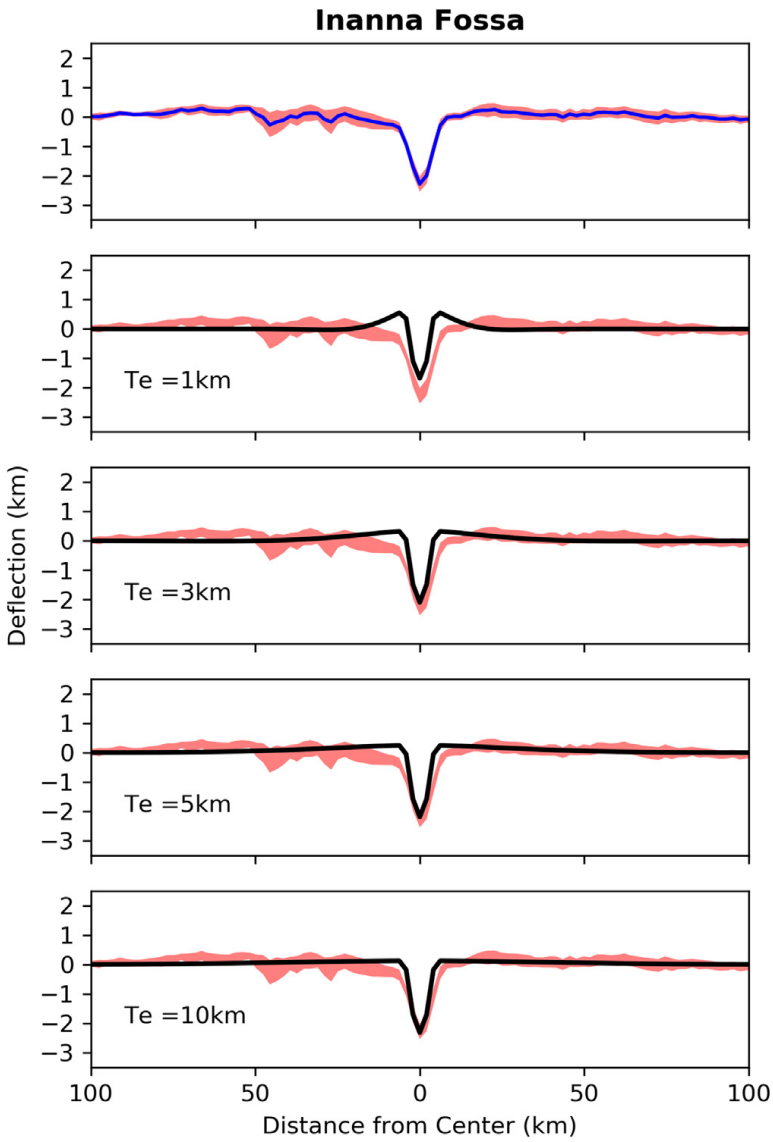

Figure 3.3: Comparison of observed topography with modeled topography for Inanna Fossa. The uppermost plot is the averaged topographic profile of the faults we included in our study. The red area brackets the profile to show the profile's standard deviation. The lowermost four plots show the resulting model topography when the load described in this section is applied to a plate of various elastic thicknesses. As the elastic thickness increases the resulting model topography approaches the applied load shape. These may be compared to the uppermost plot. The red area in each box represents the standard deviation of Inanna's topographic profiles.

troughs and widths of 13.2 km and 17.4 km for Dumuzi and Beatrice respectively. For Beatrice Fossa we calculate a minimum elastic thickness about the same as Inanna Fossa. This is expected as the topography of the fossae flanks is structurally similar to Inanna Fossa's. Virgil Fossa is structurally separate from the other major fossae in the regions west of Sputnik Planitia as the southern flank is higher by ∼1 km. Asymmetries across the fault profile prevent easily assigning a load shape to the whole fault. As such we determine statistical values like the misfit from each side separately with different model load topographies. We calculate the mismatch for the side where the load topography matches that flank's topography better and combine the misfit that we individually calculate for each side. Similarly, for Dumuzi Fossa we ignore the northern flank for our analysis due to the dominance of Inanna Fossae.

We use the results of our deflection models to determine the misfit between the model results and the observed topography. The χ^2 misfit between our model results and observed topography is calculated as follows:

$$\chi_i^2 = \sum_{i=1}^{N} \frac{1}{s_i^2}(z_{i,o} - z_{i,m})^2 \tag{3.5}$$

where N is the number of points outside the trough, s is the standard deviation of the ith point (as shown in Figure 3.2), and z is the topography of the observation (o) and model (m) for locations exterior to the trough width. We then calculate the misfit for every t_e in our model set. Generally, the misfit decreases as the elastic thickness increases (Figure 3.4). We then take the ratio of the misfit at each t_e to the asymptotic value reached at high values of t_e to obtain a relative misfit. This asymptotic value for

the misfit is the same as the misfit to a straight line fitting the observation data outside the trough. Once we have the relative misfit we can use an F-test (Bevington et al. 1993) to find the minimum t_e at which the model's misfit is no longer significantly different from the straight line misfit. We will use a probability level of 10%, that is values of the relative misfit less than this critical value do not yield a significant improvement over the straight-line fit at the 90% significance level. Additionally, to perform this test we need to determine the number of degrees of freedom v for our models and observations. Nearby points on a topographic profile are strongly correlated with each other, so that the number of effectively independent observations of topography is less than the total number of points. To estimate the number of independent observations N we determine the correlation length (J) between points in our profiles, where J is the mean number of points at which the correlation drops below 0.5. For all four profiles we obtain $J \sim$25. This in turn yields N=600/25=24 and v=22. At the 10% level this value for v gives an f-value of $\sim$1.74. The results for this analysis are displayed in Figure 3.4.

Our results for the F-test show that for Inanna, Virgil, and Beatrice fossae the crossover point for a relative χ^2 value of $\sim$1.74 occurs at t_e $\sim$8–10 km. However, Dumuzi Fossa fails to produce any result significantly different than the background variance. We ignore Dumuzi Fossa in the analysis in the following section. From the other three fossae we set a minimum elastic layer thickness of 8 km based primarily on the result for Inanna and Beatrice Fossae. While 8 km is a low value for a modern day elastic thickness given results of Pluto thermal history models (e.g. Bierson et al. 2018), properties in the past could have been different and the value we found here

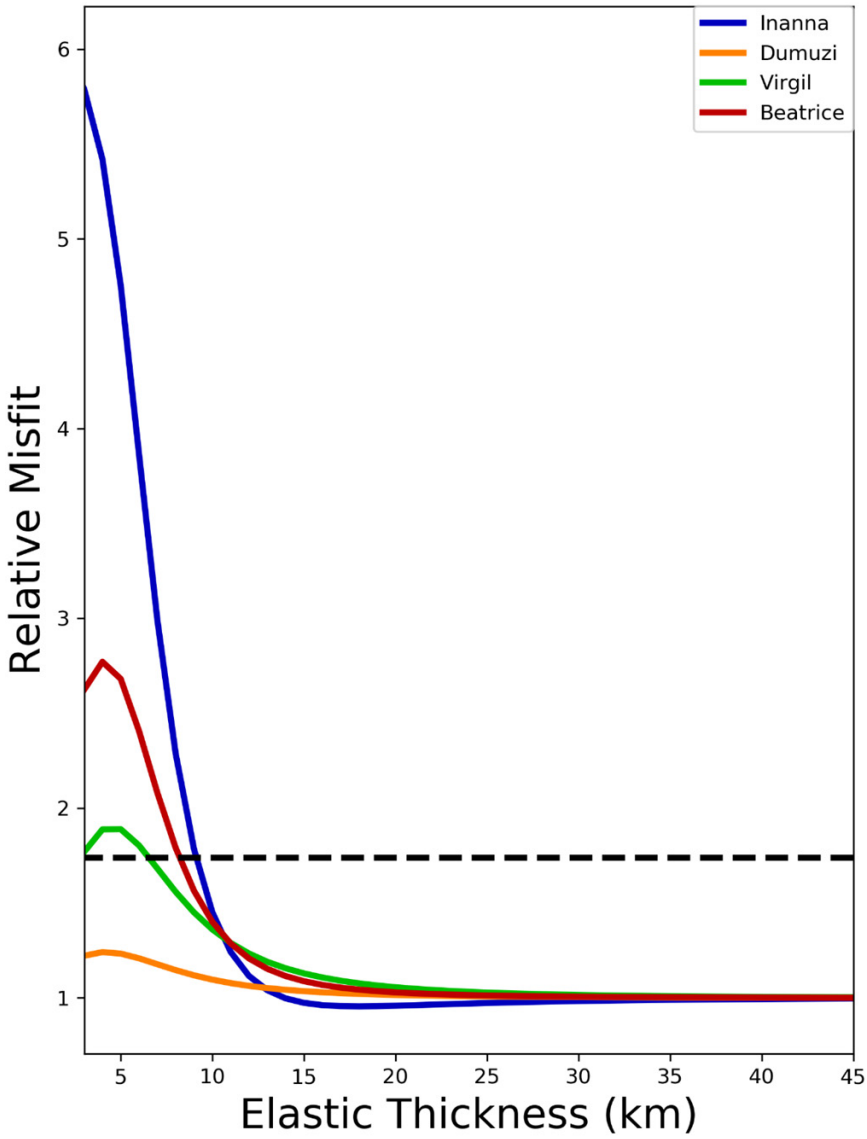

Figure 3.4: Relative misfit between our modeled deflection topography and the averaged topographic profiles for the extensional graben. The misfit is normalized by the asymptotic misfit for each graben. Color of each line matches the color scheme used in Figure 3.2 as shown in the figure legend. The dashed line represents the relative χ^2-value (1.74) for which a t_e parameter does not produce a model result misfit significantly (α=0.10) different than the background misfit. For the three largest fossae this crossover occurs at ∼8–10 km and for this reason we use 8 km as our minimum t_e value for the analysis in the following sections.

is the lower bound. The actual value could be anywhere in the range we set for our models, or perhaps higher.

3.3.2 Heat flux

Given an estimated minimum elastic thickness, we can additionally estimate the thermal structure of the elastic layer at the period of fault formation and find the maximum surface heat flux since the time of fault formation. While there are various ways of doing so in the literature, here we adopt an approach that utilizes the composite nature of different ice deformation regimes (Goldsby and Kohlstedt, 2001). We use the three primary grain boundary sliding regimes from Goldsby and Kohlstedt (2001) to determine a range of likely values for T_b, the temperature at the base of the elastic layer. Those regimes are basal slip-accommodated grain boundary sliding (GBS), GBS-accommodated basal slip, and dislocation creep. Note that we neglect diffusion creep as it is only likely to be important at very small grain sizes. Table 3.1 summarizes the values we used for the calculations in this section and show the difference in parameters between the three regimes. To be conservative we assume any of these mechanisms could be the dominant mechanism when obtaining heat flux estimates (Figure 3.5) and as such we use their cumulative strain rate relationship (Goldsby and Kohlstedt, 2001).

$$\dot{\varepsilon}_{comp} = \left(\frac{1}{\dot{\varepsilon}_{gbs}} + \frac{1}{\dot{\varepsilon}_{basal}} \right)^{-1} + \dot{\varepsilon}_{dis} \tag{3.6}$$

Here $\dot{\varepsilon}$ is the strain rate (which we estimate in this section) and the subscripts comp, gbs, basal, and dis correspond to composite (i.e. cumulative), basal

slip-accommodated grain boundary sliding (GBS), GBSaccommodated basal slip, and dislocation creep respectively. We will calculate the individual contribution to the strain rate for each regime as it depends on T_b and σ_{crit}, the critical stress at T_b. The strain rate for a given regime can be expressed as:

$$\dot{\varepsilon}_i = \left(\frac{\sqrt{3}}{2}\right)^{n_i+1} A_i d^{-p_i} \sigma^{n_i} \exp\left(\frac{Q_i}{n_i RT}\right) \tag{3.7}$$

Here $\dot{\varepsilon}$ is the strain rate, σ is the stress, d is the grain size, R is the gas constant, and A, Q, p, and n are rheological constants as defined by the different deformation regimes (Goldsby and Kohlstedt, 2001). The values for every variable in Eq. (6) can be obtained from Table 3.1 except for the stress, which is determined from assumptions of the crustal structure as follows. A transition from the elastic layer to the viscous layer of Pluto's crust occurs when the product of the Maxwell time and the strain rate is equal to the dimensionless Deborah number (De; Mancktelow, 1999). This, with the definition of the Maxwell time, will make the critical stress equal to:

$$\sigma_{crit} = De * \mu \tag{3.8}$$

Here μ is the shear modulus of water ice (rigidity and shear moduli are equivalent). We assume De ranges between 10^{-2} to 10^{-3}, using a slightly wider value range than Nimmo et al. (2002), and note that our upper bound values are based on De=10^{-3}. Changing De by an order of magnitude to 10^{-2} results in a decrease of T_b by about 10 K, not enough to significantly affect our conclusions. Taking De=10^{-3} is consistent with the thermal state and measured elastic thicknesses of terrestrial oceanic lithosphere (Watts 2001); for our case it also results in stresses of order 1 MPa, which is comparable

to the stresses resulting from the graben topography. The shear modulus we use is the same as in the flexure analysis (Section 3.3.1) and the value of it is included in Table 3.1.

We can now calculate $\dot{\varepsilon}$ for a given range of T_b values given a set of parameter values (Figure 3.2). For the grain sizes we use a range from 1mm to 10 cm; Barr and McKinnon (2007) showed that for large icy satellites (i.e. Ganymede/Callisto) this range of grain sizes should apply. Since the bulk of Pluto's ice shell is not expected to differ significantly from these worlds on a near-surface compositional level (although there are significant surface and atmospheric differences; Stern et al. 2015), we use the same range as in their study. We also assume that the elastic layer extends to the surface (i.e. we ignore any brittle layer).

When we calculate the strain rate from T_b we want to know what range of strain rates are reasonable for Pluto's geophysical history. While the exact amount of global surface strain for Pluto is unknown, we can estimate a range of reasonable strain rate values to use for our calculations based on thermal model results and the arguments presented for a present-day subsurface ocean (Nimmo et al. 2016). We analyzed a variety of thermal model solutions for the internal evolution of Pluto (e.g. Hammond et al. 2016; Bierson et al. 2018) to estimate the change in radius in the expansionary phase of Pluto's history (i.e. as the ocean re-freezes). These models predict $\sim$5 km of radius extension as the subsurface ocean freezes from its maximum extent to the present. From calculating the change in surface area of a sphere we calculate strains $<$1%. This would imply that the average strain rate over the extensional period of Pluto's history is about

10^{-19} s^{-1}. Other estimates of strain rate can be based on assumption for fault formation in response to reorientation of Pluto due to Sputnik Planitia formation (Keane et al. 2016; Nimmo et al. 2016). If we assume that the areal strain is ∼0.5% and is solely due to reorientation stresses, and we assume that reorientation happens due to growth of the nitrogen ice cap in SP, which Keane et al. (2016) finds to be 5 million years, then the strain rate should be ∼10^{-16} s^{-1}. For Figure 3.2, we present a range of strain rates from 10^{-20} to 10^{-14} s^{-1} with our highest preference put on strain rates between 10^{-19} s^{-1} and 10^{-16} s^{-1}. This approach allows us to infer a range of possible T_b values from the range of $\dot{\varepsilon}$.

To find the maximum heat flux since graben formation we use the temperature profile of a conductive ice shell, in which the thermal conductivity of ice, κ, varies as 567/T (Klinger, 1980). Because Pluto is not expected to be tidally-heated after reaching dual-synchronous orbit with Charon (which is expected to happen quickly), we neglect any source of internal heat in the icy shell. We do not include any effects from porosity; including porosity would result in a lower estimated heat flux, because porosity will reduce the strength of the ice and increase the near-surface temperature gradient. There are methods to include porosity (Giese et al. 2008), but as we are calculating the maximum possible heat flux these methods are not used. The heat flux F, with top and bottom temperatures T_s and T_b, respectively, is given by:

$$\frac{F}{567} = \frac{\ln(T_b/T_s)}{t_e} \tag{3.9}$$

Figure 3.5 shows how the temperature at the base of the elastic layer, T_b, and

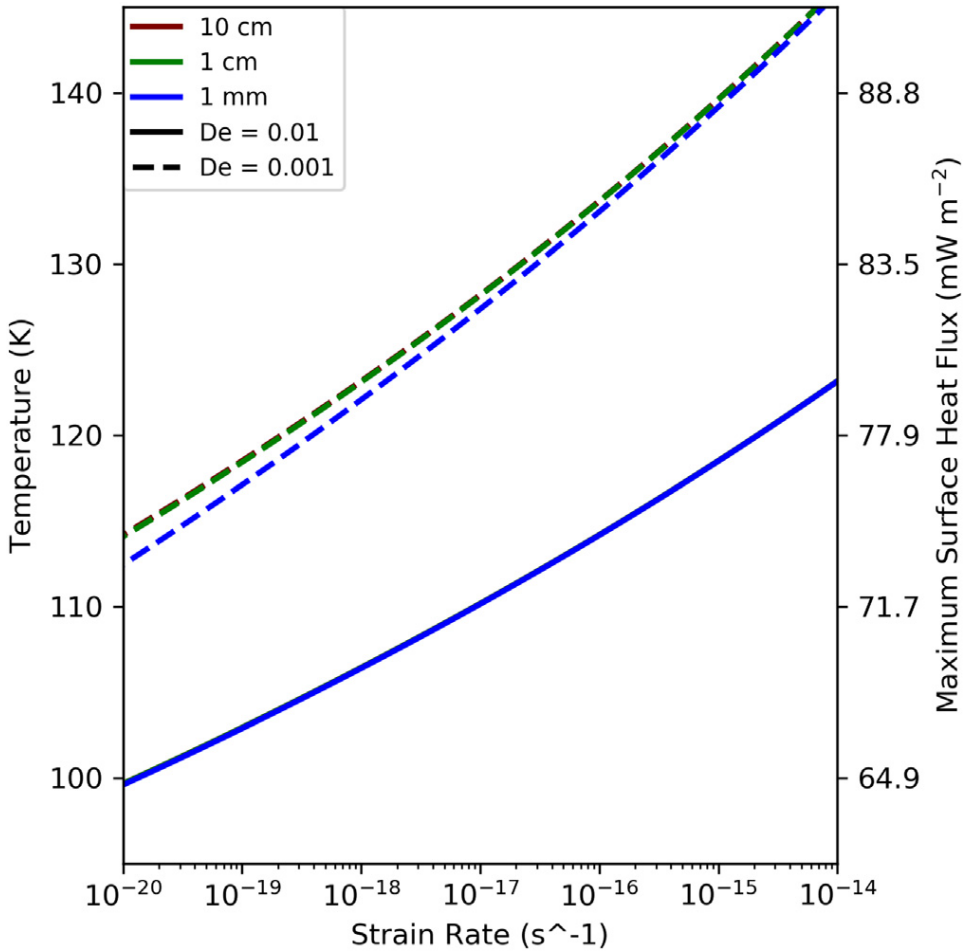

Figure 3.5: Temperature at the base of the elastic layer and maximum surface heat flux as it relates to strain rate with the elastic thickness set at t_e=8 km and a De range of 0.01–0.001. The elastic thickness is derived from the model for Figure 3.3 and is the minimum value based on our analysis. The three colors correspond to different grain sizes, with red as 10 cm, green as 1 cm, and blue as 1 mm, and the line style corresponds to the value of De. For De=0.001, the results for 10 cm and 1 cm nearly overlap which is a signal that the GBS-accommodated basal slip (which depends on grain size) is less prominent relative to dislocation creep at large grain sizes for our set of parameters. For De=0.01, the results for all three grain sizes overlaps which is a factor of dislocation creep dominating the cumulative ice flow.

the heat flux at the surface, F, varies with the strain rate, $\dot{\varepsilon}$, for three different grain sizes, t_e=8 km, and De=0.01–0.001. For the strain rate range of 10^{-19} s^{-1} to 10^{-16}

s^{-1} and an elastic thickness of 8 km, likely T_b values are ∼103–113 K for De=0.01 and ∼115–133 K for De=0.001 and a maximum possible surface heat flux since graben formation in the range of ∼66–85mWm^{-2} including both values of De is found. Depending on the range of strain rate, grain size, and Deborah number the elastic base temperature varies by $\sim \pm 15$ K and the maximum surface heat flux varies by $\sim \pm 9.5$mWm^{-2}. However, we stress here that the values found here represent maximum possible values; heat fluxes on Pluto are expected to have been lower (see below).

3.4 Discussion and conclusions

We found above that the absence of any observed rift-flank uplift implies a lower bound on elastic thickness of 8 km and, assuming a strain rate range of 10^{-19} s^{-1}–10^{-16} s^{-1}, an upper bound on heat flux since graben formation of 66–85mWm^{-2}. This is a conservative estimate, as neglected factors such as plate failure or porosity would tend to increase the inferred t_e and decrease the heat flux respectively.

3.4.1 Other heat flux estimates

Hammond et al. (2016) predict a maximum mean surface heat flux of ∼6mWm^{-2} at ∼3.5 Ga, with the maximum subsurface ocean thickness occurring at roughly the same time. Bierson et al. (2018) predict around the same value for the mean surface heat flux with a slight difference in the approximate time of maximum for both the heat flux and subsurface ocean at ∼2.5 Ga. Regardless, extensional graben should form after the subsurface ocean starts to refreeze due to the extensional stresses from the increase in

volume. Such low predicted heat fluxes are certainly consistent with our lower limit constraint, since they would imply elastic thicknesses of roughly 100 km. Both models (in addition to Robuchon and Nimmo, 2011, which also predicts a possible convective ice shell with around the same maximum heat flux) use radiogenic decay as the primary heat source.

3.4.2 Relaxed craters as a possible heat flux constraint

As noted in McKinnon et al. (2018) there are a pair of complex craters to the west of the fossae analysis area with an interesting difference in possible relaxation state. The craters of Oort (7.5° latitude, 91.5° longitude) and Edgeworth (6.5° latitude, 108.5° longitude) are approximately the same size (120 km and 140 km respectively), but display different relaxation states (Moore et al. 2016). Oort crater is relatively pristine for a complex crater on Pluto while Edgeworth's crater floor is either bowed up in a way that signals viscous relaxation (McKinnon et al. 2018) or in-filled with SP-like material in the same manner as Elliot crater (12° latitude, 138.5° longitude; Schenk et al. 2018a). The possible viscous relaxation shaping Edgeworth crater could help constrain the maximum surface heat flux through numerical modeling similar to that applied at Dione and Tethys (White et al. 2017). White et al. (2017) found that for similarly-sized craters to Edgeworth (e.g. Dione: Aeneas and Alcander; Tethys: Dolius) the required heat flux to relax those craters to ∼70–80% relaxation fraction is ∼50–60mWm^{-2}. While some factors (i.e. gravity and surface temperature) are different on Pluto, the likely result will be similar for Edgeworth crater. This relaxation-derived

heat flux is marginally consistent with our maximum possible heat flux. However, a more thorough study into Edgeworth crater, as well as the proposed relaxed crater of Burney (45° latitude, 134.5° longitude; main ring diameter ~250 km), should give a more precise insight into the thermal history of Pluto.

3.4.3 Fault stresses

The relationship between maximum shear stress (σ_{max}) on a fault and the regional elastic thickness is well documented for the Earth (Jackson and White 1989). Determining the maximum shear stresses that these faults could support is useful in determining the overall strength of Pluto's icy crust and comparing to terrestrial analogs. We use the set of equations from Jackson and White (1989) to describe σ_{max}:

$$\sigma_{max} = \frac{\rho_c g h}{2e} \qquad if\ \frac{\lambda}{t_e} < \frac{\pi}{2} \tag{3.10}$$

$$\sigma_{max} = \frac{3\rho_c g h \lambda}{8\pi t_e} \qquad if\ \frac{\pi}{2} < \frac{\lambda}{t_e} < \pi \tag{3.11}$$

$$\sigma_{max} = \frac{3\rho_c g h \lambda^2}{8\pi^2 t_e^2} \qquad if\ \frac{\lambda}{t_e} > \pi \tag{3.12}$$

Here $2h$ is the vertical displacement of the fault, e is the base of natural logarithms, and λ is the wavelength of the faulting width (twice the trough width in most cases). All other variables are the same as described in previous equations. Stresses must support the gravitational load of the faults to maintain topography; as the vertical displacement ($2h$) or trough width ($\lambda/2$) increases the stresses must also increase. It is unlikely that there are faults where $\lambda/t_e > \pi$ on Pluto based on our results, but we include the final equation for completeness. For Inanna and Beatrice Fossae we calculate

the maximum shear stress values based on their dimensions (λ and h) and a range of possible t_e values (1–60 km). We note that, past around t_e=18 km (i.e. where t_e=$2\lambda/\pi$) the maximum stress is constant (Eq. (10)) as t_e is increased. For Inanna and Beatrice Fossae the maximum shear stress supporting the faults is between ∼140 kPa and 290 kPa. Even at the maximum possible shear stress, Pluto's faults only need to support comparatively low stresses compared with faults on silicate bodies. Earth and Mars' faults appear to be able to support shear stresses on the order of a few to tens of MPa (Barnett and Nimmo, 2002) and Venus' exceptionally dry environment supports faults with strengths of ∼80 MPa (Nimmo and McKenzie, 1998). If the stresses responsible for causing the faults on Pluto were comparable to our estimated maximum shear stresses, they would be small compared to terrestrial plate tectonic stresses, but comparable to the tidal stresses apparently capable of driving deformation on Europa (Hoppa et al. 1999). Such small stresses would alternatively result from only a few hundred meters of shell thickening. True polar wander may have been an additional source of stress (Keane et al. 2016).

3.4.4 Implications of constraining Pluto's elastic thickness and heat flux in regard to surface features

The minimum elastic thickness values found in this study are higher than values calculated for icy satellites of giant planets (e.g. Nimmo et al. 2002; Giese et al. 2008; Peterson et al. 2015). One possible explanation is that Pluto, lacking a companion with greater mass, is unlikely to have ever experienced significant tidal heating. As such,

in this respect it is likely more similar to Callisto, which is distant enough not to be strongly tidally-deformed. Callisto however lacks evidence of wide-spread extensional tectonics (Moore et al. 2004).

Determining a maximum heat flux serves as an important constraint on possible processes to create and modify various features across the surface of Pluto. The ability of craters and large tectonic features (Schenk et al. 2018a) to relax place additional constraints on heat flux. Other features, like SP's convecting nitrogen ice layers are consistent with the low heat fluxes expected just from radioactive decay (McKinnon et al. 2016), but they do not constrain surface heat flux estimates because of uncertainties in the thickness of the nitrogen ice layer. Determining Pluto's elastic thickness history is also important to understanding Pluto's shape (Nimmo et al. 2017). Pluto is nearly spherical, with no obvious flattening. This probable lack of a fossil bulge can be explained by the development of an ocean, or by a low elastic thickness early in Pluto's evolution (Robuchon and Nimmo, 2011, Hammond et al. 2016; Bierson et al. 2018). Integrating all the available constraints into a single, coherent picture of Pluto's thermal evolution remains a challenge for the future.

Chapter 4

Heat Flux Constraints from Variance Spectra of Pluto and Charon from Limb Profile Topography

This chapter is a slightly modified reprint of work previously published as Conrad, J. W., F. Nimmo, R. A. Beyer, C. J. Bierson, and P.M. Schenk (2020) "Heat Flux Constraints from Variance Spectra of Pluto and Charon from Limb Profile Topography." Journal of Geophysical Research: Planets, submitted

Abstract

We derive a topography dataset from images of Pluto and Charon that contain the body edge (i.e. limb profiles) which will help in understanding the comparative history of the binary system. We use the profiles to derive topographic variance spectra

and find that while the variance spectrum of Pluto fits a single power law, Charon's spectrum displays a clear breakpoint at 150 km wavelength. Assuming the breakpoint is a result of topographic flexure, we find that Charon's elastic thickness must have been 20±10 km during topography formation. A lack of a breakpoint for Pluto sets a minimum elastic thickness for Pluto of 60 km. We use these elastic thickness estimates to calculate a maximum heat flux of ∼13 $\mathrm{mWm^{-2}}$ on Pluto during and after topography formation. On Charon, however, we find that the heat flux during topography formation was 35^{+44}_{-15} $\mathrm{mWm^{-2}}$. This range of values far exceeds the likely radiogenic heat production and is consistent with either heat released following the Charon-forming impact event or (more likely) tidal heating during Charon's early history.

4.1 Introduction

When the *NewHorizons* spacecraft reached the Pluto system in 2015, the illuminated disks of Pluto and Charon revealed the complexities of these Kuiper Belt Objects' geologic histories (Stern et al. 2015). Pluto is a world with a surprising range of surface ages and processes (Moore et al. 2016), while Charon has experienced a large amount of tectonic deformation (Beyer et al. 2017). Understanding why this difference in surface expression has resulted from the evolution of the Pluto system is one way to understand Kuiper Belt objects in general. We use topography derived from the body edge (i.e. limb profiles) in images of Pluto and Charon to study if there is an observable difference in the topographic variance of the two worlds.

While the current understanding of Pluto and Charon is based primarily on studies following the *NewHorizons* spacecraft mission, we will use ideas and techniques used in studies of other icy bodies. Although there are likely geologic differences between the two types of worlds (icy dwarf planets and icy satellites) due to how they form (Bierson and Nimmo 2020), their water ice crusts are likely to have similar rheologies. As a result, we will make use of previous studies that focus on understanding icy satellites with limb profiles (e.g. Nimmo et al. 2011).

We analyze the shapes of Pluto and Charon to understand the internal, thermal, and surface history of the two worlds. Nimmo et al. (2017) started this analysis of Pluto and Charon, focusing on the global shape (i.e. degree-2) using topography obtained from limb profiles. They found that both Pluto and Charon have flattening values less than $\sim$0.5%, which makes them effectively spherical. This puts broad constraints on the internal evolution of Pluto and Charon, and this lack of a fossil bulge is part of the argument for the existence of a past (and possibly present) subsurface ocean for both bodies (e.g. Keane et al. 2016; Nimmo et al. 2016). However, the limb profiles from Nimmo et al. (2017) contain information over a wide range of wavelengths. By expanding upon their work, we can investigate aspects of Pluto and Charon over a range of wavelengths. This increased range in wavelength analysis is one way of investigating if Pluto and/or Charon have been heated beyond radiogenic heating.

Length scales intermediate between those considered to represent the shape of the body (e.g. the flattening) and individual surface features contain geologic information about the interplay between interior and surface processes (Shepard et al. 2001)

and have been useful in determining geologic parameters, especially the thickness of a crust's elastic layer (e.g. Araki et al. 2009; Nimmo et al. 2011). We analyze our limb profile topography dataset using Fourier analysis to understand how the amplitude of the topography varies over a range of wavelengths. With this analysis, we find that the amplitude trend as a function of wavelength of Charon's limb profile topography has a break (i.e. change) in slope at a length scale in the range of ∼70-300 km. This observed characteristic wavelength for Charon's topography implies that either a surface process (or processes) prefer to form features at that wavelength or the interior behavior of the crust changes at a related wavelength. We analyze our results assuming that the latter is the case as it is not clear why a surface process would form features preferentially at that wavelength on Charon, while not doing so on Pluto. More specifically, we assume that the characteristic wavelength is the flexural parameter, implying an elastic thickness of ∼20±10 km. We also derive a minimum elastic layer thickness of 60 km for Pluto from a lack of break in slope. The thickness of these layers can be used to constrain the total conductive ice shell thickness and the surface heat flux at the time of topography formation. Compared to previous studies (Conrad et al. 2019), we find an upper bound on surface heat flux values for Pluto (∼13 $\mathrm{mWm^{-2}}$) that are more consistent with a primarily radiogenic heat source. However, the values for Charon (35^{+44}_{-15} $\mathrm{mWm^{-2}}$ during topography formation) require additional heat sources, which could be sourced from tidal deformation or a Charon-forming impact.

4.2 Methods

The primary goal of this study is to produce topographic datasets for Pluto and Charon derived from planetary limb profiles, separate from photogrammetry-derived digital elevation models (DEMs; Schenk et al. 2018a; Schenk et al. 2018b). We achieve this by determining the edge of the planetary body from images (i.e. limb picks). Using map projections and the known observing geometry, we can transform the pixel locations of the limb picks into a list of elevations at specific latitude and longitude locations. While our methodology mostly matches that of Nimmo et al. (2017), we will reiterate some aspects of their methods to detail updates and changes.

4.2.1 Limb picking methods

We began our process with a survey of *NewHorizons* images from the Long-Range Reconnaissance Imager (LORRI; Cheng et al. 2009) and the Ralph instrument's Multispectral Visible Imaging Camera (MVIC; Reuter et al. 2008) sub-instrument. Data from both instruments have been used extensively to study Pluto, Charon, and most recently Arrokoth (Spencer et al. 2020). Starting with the Planetary Data System, we surveyed the images to create a list of images containing body edges starting when Pluto was $\sim$100 pixels in diameter. In addition, we removed redundant images from the list. This list contained both day-side and night-side images from both LORRI and MVIC as the starting point for further analysis.

While we initially performed limb picks and fits for both LORRI and MVIC

images, we found large-amplitude, long-wavelength undulations for MVIC limb profiles. This occurs in MVIC images due to the line-scan exposure method combined with spacecraft motion (Weaver et al. 2009). Due to the relatively small number of MVIC images, we instead focus on the LORRI images in this analysis.

For limb picks of day-side (i.e. front-lit) images, we use Method A as presented in Nimmo et al. (2017). This method scans each row and column in the image to find the location of the limb where the brightness along the scan compared to the brightness of the on-body profile reaches a specific threshold. They found that two of their three methods (A and B) did not have systematic issues in over or under-estimating the radius, based on synthetic Pluto images. This is because the parameters in those methods could be tuned to correct the estimations. We generally calculate the average brightness over the same distance range ($0.5d$ to $0.9d$, where d is the on-body profile length from center to body edge) and then use the same brightness threshold (40%) as Nimmo et al. (2017) used with Method A. Images that show initial limb picks can be seen in Figure 1 of Nimmo et al. (2017).

Once the list of limb pixel locations is determined, we visually verify the algorithmically chosen limb picks and manually remove picks that are obviously not on the limb. These false limb points are often the result of either albedo variations or the terminator. Large albedo variations are only an issue with Pluto images that contain Cthulhu Regio (CR), a region south-west of Sputnik Planitia (SP). Limb picks of images that contain areas of CR that border regions of high albedo (e.g. SP) tend to place the limb location in CR inward of the actual limb. This happens because the average disk

brightness is incorporated into the algorithm, and if the brightest area of Pluto is near the middle while the darkest is at the edge, the 40% cutoff will occur before the actual limb location. However, we note that the local albedo at the limb does not show a systematic correlation with topography (see section 4.3.1), suggesting that this effect is minor. The algorithm also does not discriminate between the limb and terminator of the body, and we only use locations where the edge of the lighted hemisphere is caused by the edge of the body (limb) rather than the edge of the illuminated hemisphere (terminator). While some terminator picks can be accidentally incorporated into a set of limb picks, we apply additional geometric checks in the fitting method described below to remove points not located on the illuminated limb.

Although Nimmo et al. (2017) provide an extensive discussion of the uncertainty in recovering a body's radius, they did not discuss the uncertainties associated with individual limb picks. Dermott and Thomas (1988) argue that the limb location (a sharp transition in brightness) can be located to within $\sim$0.2 pixels. Since our method is similar to theirs, we assume that the same level of uncertainty applies to our limb profiles.

In night-side (i.e. backlit) images, the disk of Pluto is weakly illuminated by forward-scattered light from atmospheric hazes. The sharp contrast between the dark disk and the bright haze is captured very clearly by taking the gradient of the image. Therefore, to identify the limb in backlit images each row and column of the image is scanned away from the body center and the limb is taken to be the location of the maximum gradient. Unfortunately, this technique does not work on Charon due to

its lack of atmospheric hazes. Additionally, while this technique produces good quality topography for middle to long-length scale features (∼100 km; see Stern et al. (2020) for an application of night-side derived topography), at short wavelengths the profiles are noisy, presumably due to the low signal-to-noise ratio. Due to contamination concerns in our spectral analysis, we therefore focus on front-lit LORRI images in the following sections.

4.2.2 Limb fitting methods

After determining the limb location in terms of pixels (x,y), we use the camera intrinsics in the SPICE instrument kernels to project these points onto a spherical body to convert to an equivalent latitude, longitude position (φ, θ) on a spherical body given the image coordinates of the body's center (x_0, y_0), the latitude and longitude of the sub-spacecraft location (φ_0, θ_0), the body's radius R and the orientation of the rotation pole relative to the image (ϕ). The spacecraft parameters are calculated using the most consistent SPICE information based on the smithed kernels from Schenk et al. (2018a&b). We report these values for all used images in Tables C.1 and C.2, and the results of the pixel locations for x_0, y_0 and R (in pixels) in Tables C.3 and C.4. We use a general vertical perspective (GVP) projection for determining the latitude, longitude positions (φ, θ) of limb pick locations (Snyder 1987). Near closest approach, we account for the effect that can lead to a shifting of the limb to an angle less than 900 away from the sub-spacecraft point. At distances d far from the body center ($d \gg R$), the GVP projection reduces to the orthographic projection, which is commonly used

in limb profile fitting studies (Nimmo et al. 2017). In our projections we assume that both Pluto and Charon are spherical, based on the results of Nimmo et al. (2017). This simplifies the map projection calculations and determination of the radii from the (x,y) pixel locations. We also check if points are on the limb rather than the terminator by determining the angular separation between the points and the subsolar point on the surface. If the angle between the two points is greater than 90°, we remove the point from the limb profile. Subsolar coordinates are also present in Tables C.1 and C.2. Elevation is reported as relative to the mean radius of Pluto (1188.3 km) and Charon (606 km) also determined in Nimmo et al. (2017).

As expected from the flyby timing relative to Pluto's rotation rate, we managed to obtain wide longitudinal coverage from the images. The longitudinal range spans about 220° on both worlds. While the coverage is not enough to perform analysis of global shape beyond degree 2 using spherical harmonics (e.g. Nimmo et al. 2017), the profiles cross a wide range of terrain types. Although these profiles may be used to study individual features, in this manuscript we focus on the variation of roughness with wavelength contained within the profiles. The image properties and limb picking information relevant to our analysis are included in Tables C.1 (Pluto) and C.2 (Charon) in the appendix.

4.2.3 Data processing methods

After we obtain raw limb profile topography, the data are processed to remove a few different possible problems as described below. Generally, we use the raw data

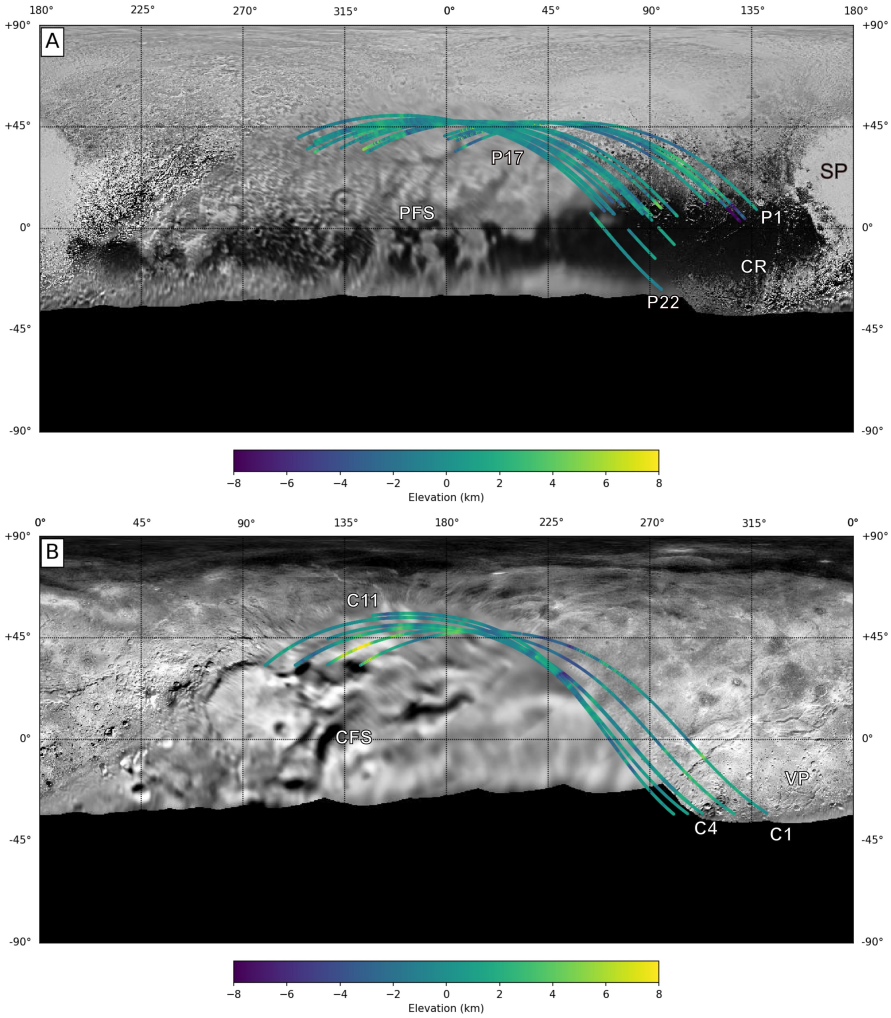

Figure 4.1: Maps of Pluto (a) and Charon (b) with limb profile locations and topography. Labels number specific limbs to the indexing in Figure 4.3, and limbs are generally arranged in the encounter sequence from right to left. Other labels reference major areas on both bodies. Sputnik Planitia (SP), Cthulhu Regio (CR), and Pluto's Far Side (PFS) for Pluto. Vulcan Planitia (VP) and the Charon Far Side (CFS) for Charon. Background images are LORRI/MVIC mosaics (Moore et al. 2016) centered on the anti-encounter hemispheres of Pluto and Charon. Coordinate systems are constructed such that the zero latitude, zero longitude are placed on the Pluto-Charon tidal axis with longitude increasing eastward. Elevation color bars are capped at ±8 km to best show variations near mean elevations.

for most of our analysis, while the processed data is used with presentation of limb profiles and some aspects of our analysis. We note when we use the processed data in the relevant sections. Our primary post-processing concerns are long-wavelength false signals and short-wavelength noise. Since LORRI is a framing camera, any long-wavelength signals with LORRI images are likely real. For the presentation of the profiles in Figures 4.2 and 4.3, however, we detrend the profiles by removing the linear trend through the endpoints of the profile after interpolation (see below). This matches part of the processing we use to perform Fourier transformations in section 4.3.2.

Figure 4.2 compares our raw limb profile picks with the processed version. The short wavelength noise occurs due to the methodology of our limb picking algorithm. When we apply the line-scan method, the algorithm scans both vertically and horizontally. This can introduce noise when the horizontal and vertical scans to pick the limb yield a different answer for the same point, and usually occurs in areas of varying brightness around the limb (this can be observed in the left-hand side of the Charon profile in Figure 4.2). To remove the shorter wavelength noise, as well as prepare our limb profiles for further analysis, we interpolate the limb topography onto a grid with constant spacing at a slightly worse ground sampling distance (half the total number of original data points). We use a gaussian weighted interpolation technique which allows us to control the scale that weighs the input values for each location:

$$y'_j = \frac{\sum_i^N y_i * \exp\left(-\frac{1}{2}\left(\frac{x'_j - x_i}{\omega}\right)^2\right)}{\sum_i^N \exp\left(-\frac{1}{2}\left(\frac{x'_j - x_i}{\omega}\right)^2\right)} \tag{4.1}$$

Here the new jth (x', y') location is the point we are interpolating from the

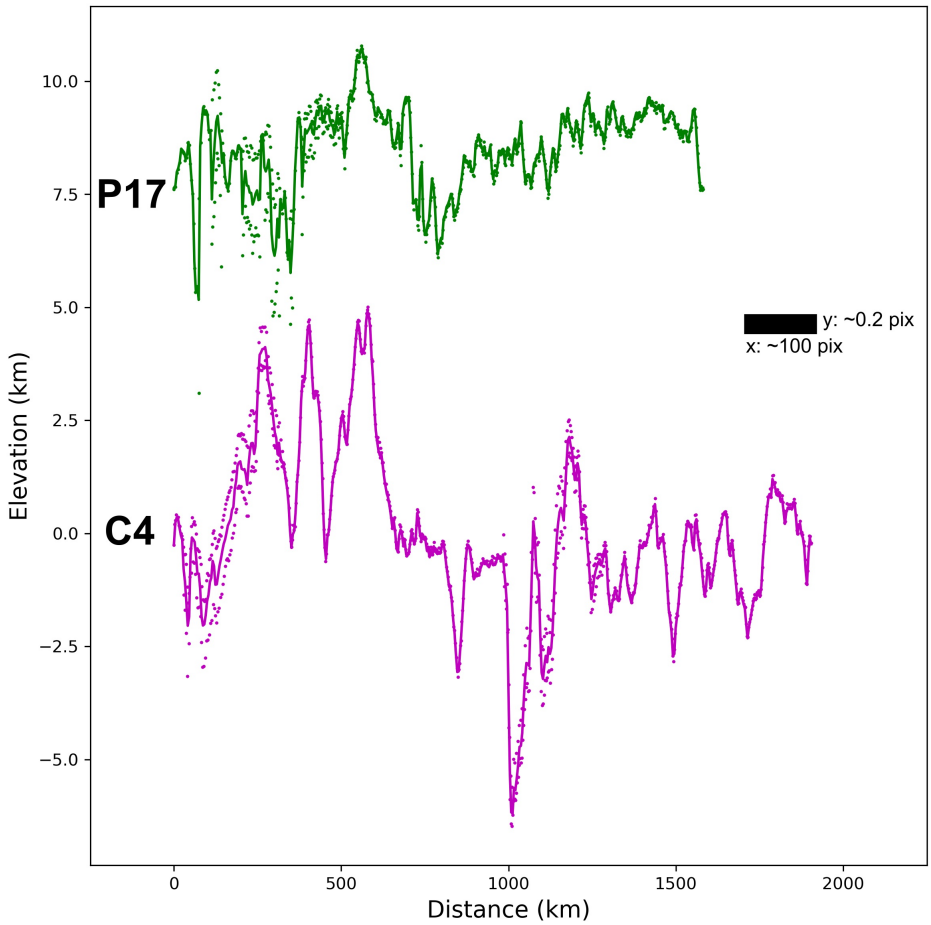

Figure 4.2: A comparison of Pluto and Charon limb profiles at similar distances from the two bodies. At a distance of ∼400 Pluto Radii (∼2.25 km/pix ground sample distance), with a vertical exaggeration of ∼132, these show how the topography at different scales vary between the two worlds. Labels to the left of the profiles corresponds to the labels on Figure 4.3, and the profiles are offset by 5 km. The dots plot the raw data before interpolation and detrending. A pixel scale bar is included to show how images translate to our limb profile topography. The 0.2 pixel corresponds to the uncertainty that Dermott and Thomas (1988) found with their similar method. Note the differences in roughness at long and short wavelengths. Charon has notable highs and lows at long wavelengths, but Pluto is rougher at shorter wavelengths.

original (x, y) data, N is the number of points in the raw profile, i is the index over which we set the weighting from the raw data, and ω is the weighting length scale. This

length scale, individually determined on each profile, is set equal to half the median spacing of points in the raw profile. The median spacing is as high as 4.7 km at the chronological beginning of the set (limb P1) and reaches a minimum of 455 m for P22 and 346 m for C11. As Figure 4.2 shows, this successfully removes the scan noise.

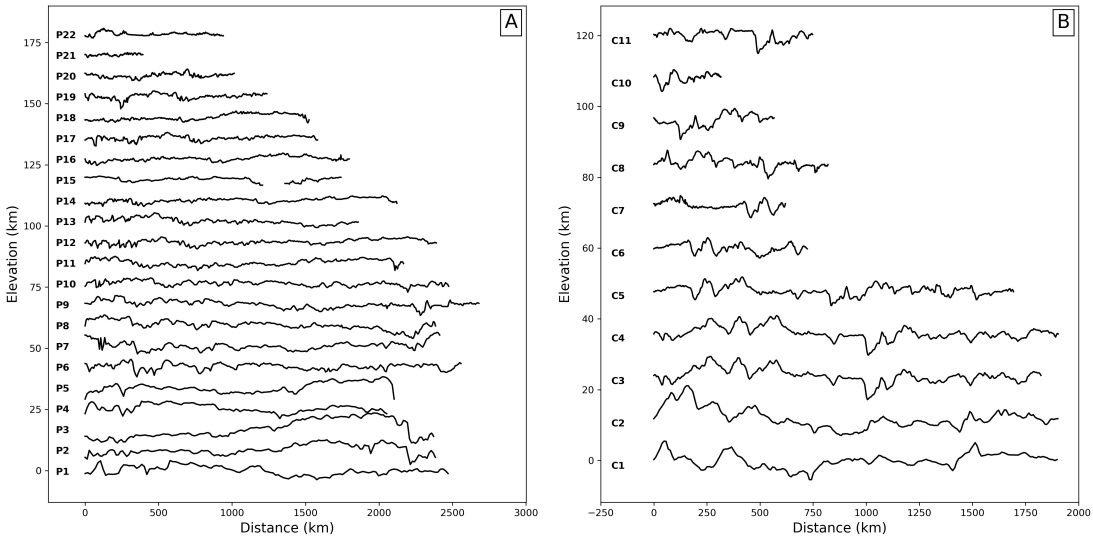

Figure 4.3: Stacked Processed (Detrended and Filtered) Limb Profiles for Pluto (a) and Charon (b). The vertical exaggeration for both figures is ∼16. Limbs are labeled in the same manner as in Tables C.1 (Pluto) and C.2 (Charon). Limbs are positive right-hand oriented, with the "western" edge on the left of the panel.

4.3 Analysis

4.3.1 Limb topography correlations

A validation method we could use is a comparison between our limb profile-derived topography with the digital elevation model (DEM) of Pluto calculated using sets of stereo image pairs (Schenk et al. 2018a&b). An unfortunate issue that arises due

to *NewHorizons*' single fly-by is a mismatch between the coverage of our limb profile topography dataset and the DEMs. When our limb profiles have a comparable ground sample distance (∼1 km per point) as the best areas of the DEMs (∼300 m/pixel), they do not significantly overlap with those DEMs. At locations where we have limb profiles which do overlap with the DEM (e.g. P1-10 and C1-4), the low quality in both the DEMs and the limb profiles makes any comparison between the two (which would provide a useful cross-check) almost meaningless. The number of limb profile points in each of the two regions that we consider contain good short wavelength information (i.e. P6-10 and C1-4) only comprises ∼4% of the total. All that can be stated with any confidence is that in the region where the DEMs and limb profiles overlap, for Charon the total relief measured by the two approaches is very comparable, whereas for Pluto the DEM-derived relief is a factor of 5 smaller than the limb-profile relief. We accordingly place more emphasis in the rest of this paper on our Charon results; further investigation of the apparent difference between the two Pluto data sets is desirable but not attempted here.

Another dataset for comparison is albedo values (Buratti et al. 2017). Since our limb picking method relies on the change in brightness, we need to investigate whether albedo variations are introducing biases into our limb picks. While Charon exhibits small albedo variations, we are more concerned with Pluto. This is due to the wide albedo variation observed on Pluto (Buratti et al. 2017), which can produce underestimates of the radius in scans that include both dark regions like CR and bright areas like SP. To investigate whether low-albedo regions (e.g. Cthulhu Regio) exhibit

systematically low elevations, we took the Bond albedo dataset from Buratti et al. (2017) and interpolated the Bond albedo onto the limb profile coordinates. The Bond albedo maps are corrected for the body geometry in images and are thus mapped as normal reflectance scaled by a body-wide phase integral. Since the angle between the spacecraft look direction and the local normal is the same for all points on the limb, we assume that geometric effects are minor. The results can be found in Figure 4.4. We then found the best linear fit between the elevation and bond albedo and found that the correlation is weak (R$\sim$0.03). Effectively there is no correlation between local Bond albedo and limb profile topography when considering the dataset as a whole; this suggests that any biases introduced by albedo variations are minor.

4.3.2 Topographic variance spectra

Topography generated from limb profiles can be used to analyze the long-wavelength properties of worlds. Limb topography variance spectra are a useful way of quantifying roughness as a function of wavelength (Araki et al. 2009; Shepard et al. 2001; Nimmo et al. 2011; Ermakov et al. 2018). To obtain the average variance spectrum, we calculate the discrete Fourier transform for each limb profile and then find the mean variance in a sequence of bins. For a set of evenly spaced topographic observations h_i, the discrete Fourier transform is (Press 1992):

$$H_j = \sum_{i=0}^{N-1} h_i e^{\frac{2\pi i j \sqrt{-1}}{N}} \tag{4.2}$$

where i, j are integers, N is the number of values in the limb profile and the

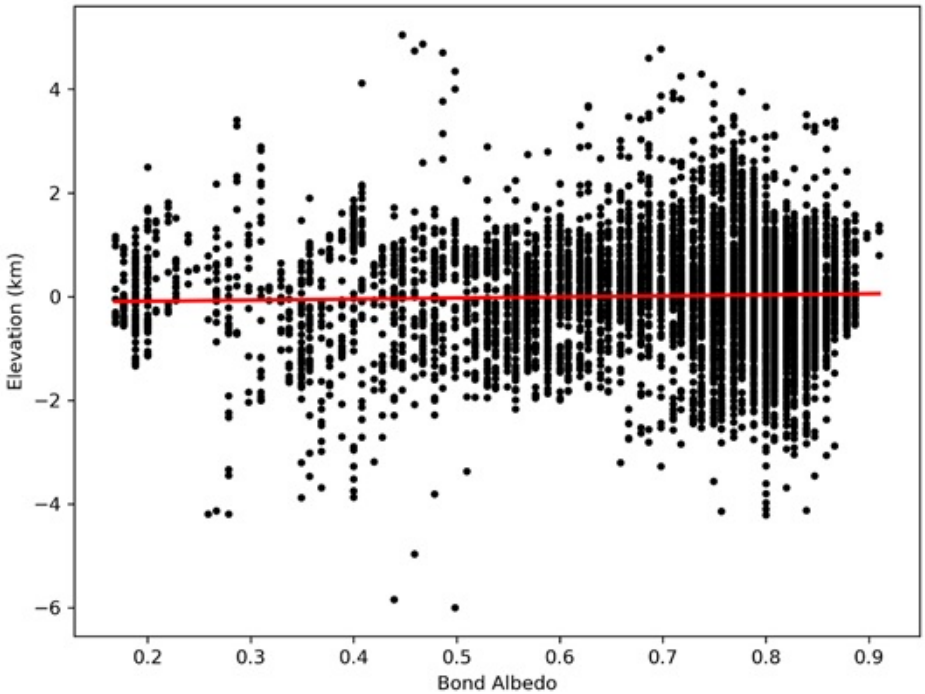

Figure 4.4: Correlation of Bond albedo and limb profile elevation for Pluto. Linear fit is plotted in red. There is no correlation between the two parameters (R∼0.03).

wave number k associated with H_j is given by $k = 2\pi(j\text{-}1)/L$, where L is the total length of the topographic profile. We use the processed profiles which have been interpolated to a constant spacing and de-trended. With the results for H_j, we then calculate the variance at each wave number as $\left|H_j\right|^2/N^2$. The results for both bodies are shown in Figure 4.5.

The primary result for both bodies is that they display a general power law trend with a slope of ∼-2. However, on closer inspection a single power law does not hold particularly well for Charon at longer wavelengths.

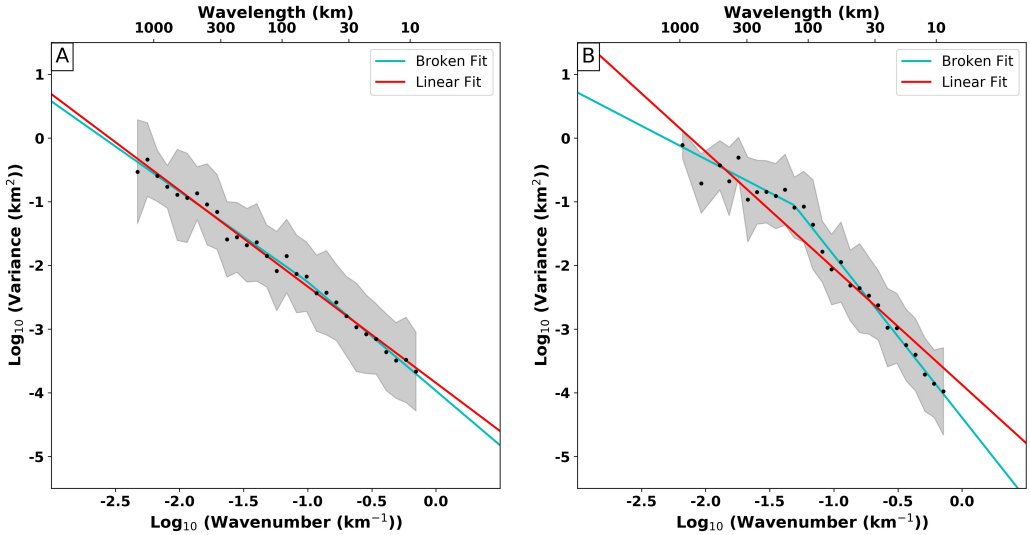

Figure 4.5: Pluto and Charon's topographic variance spectra based on limb profile topography. a. Pluto's topographic variance spectrum with a linear fit (red) and broken fit (cyan; Main et al. 1999). The variance results for the 22 Pluto limb profiles are put into 30 bins. The points represent the mean value in each bin and the shading equals the standard deviation. Pluto's topographic variance spectrum is consistent with the expected single power law fit with a power law slope of ∼-1.8. The improvement due to a broken slope is minimal, especially compared to the results of Charon. b. Charon's topographic variance spectrum with a linear fit (red) and broken fit (cyan). The variance results for the 11 Charon limb profiles are put into 30 bins. Charon's topographic variance spectrum is somewhat consistent with a single power law slope of -2, but it is improved by adding a break in the slope at a wavelength ∼150 km.

Due to possible biases from the number/distribution of the limb profiles and the fact that limb profiles are inherently biased towards topographic highs, we verified our ability to recover an accurate power spectrum using synthetic data. The base synthetic data was generated using SHTools (Wieczorek and Meschede 2018) with an input variance spectrum that resembles that of Charon, but with either a single -2-power law slope or the same with a flat variance spectrum before a break to a -2-power law slope at ∼150 km (spherical harmonic degree 25). From the global synthetic

topography, we sample by interpolating onto the same (φ, θ) locations as our Pluto and Charon profiles. We found that we could identify a break in slope if it existed, although the slope recovered from the 1-D synthetic limb profiles was slightly higher than the input slope from the 2-D spherical harmonics (a difference in slope is expected). We also tested the effect of using apparent limb profile topography rather than the actual synthetic limb topography by using the technique outlined in Nimmo et al. (2010) for profiles that have similar chord lengths as our 11 Charon limb profiles. Using Nimmo et al. (2010)'s equation (2), we determined when the masking effect of high topography off the limb causes the apparent limb topography to exceed the actual synthetic topography. We found that the variance spectra of the actual and limb-profile derived synthetic topography are essentially the same at long wavelengths and preserve the same break in slope. We conclude, as did Nimmo et al. (2010), that limb biases do not affect the variance spectra in any significant way at the wavelengths of interest. Comparison of our results with other efforts to find the variance spectra of Pluto and Charon (Ermakov et al. 2018) is deferred to the discussion section (section 4.4.2).

Determining the location and statistical strength of a possible break in slope/changepoint can be done using the method outlined in Main et al. (1999). We use their method to calculate the maximum Bayesian information criteria (BIC) with a set of possible changepoints (set at the middle of every bin), starting and ending at the fourth bin from each end. We calculate the linear fit on each side of the changepoint and compared our results to that found for a single slope linear fit. For both bodies, adding a break in slope tends to increase the fit across the spectra, as expected (Figure 4.6). However,

while for Pluto the improvement in BIC compared to the linear fit, referred to as ΔBIC, is modest (<2), for Charon the ΔBIC=14. This implies a statistically significant improvement (i.e. ΔBIC>10; Kass and Raftery 1995) signifying very strong evidence for an existence of a break in slope in the wavelength range ~70-300 km.

While a break in slope of the variance spectrum is sometimes seen for solid solar system bodies (Araki et al. 2009; Nimmo et al. 2011; Fu et al. 2017), there is probably more than one process which can create this break in slope. The break in slope in the Moon's topography spectrum is likely due to flexural effects (Araki et al. 2009), while on Ceres a crustal viscosity which varies with depth might be the cause (Fu et al. 2017). Pluto's lack of an obvious break in slope may simply be the result of a rigid lithosphere. Given previous studies which provide a lower bound on Pluto's elastic layer of ~10 km (Conrad et al. 2019), in the following sections, we test if the break in slope on Charon and the lack of a break on Pluto can be explained by elastic (flexural) processes.

4.3.3 Topographic support

Pluto and Charon's modern crusts are the result of their evolution from the initial states they had after formation. Thermal models (e.g. Hammond et al. 2016; Bierson et al. 2018) show that the initial state has little effect on the current thickness of the ice shell: Pluto likely has a subsurface ocean and Charon should be completely frozen. However, while the mean final state of either body should be similar regardless of the initial state, the tectonic path they took depends on that state. The tectonic

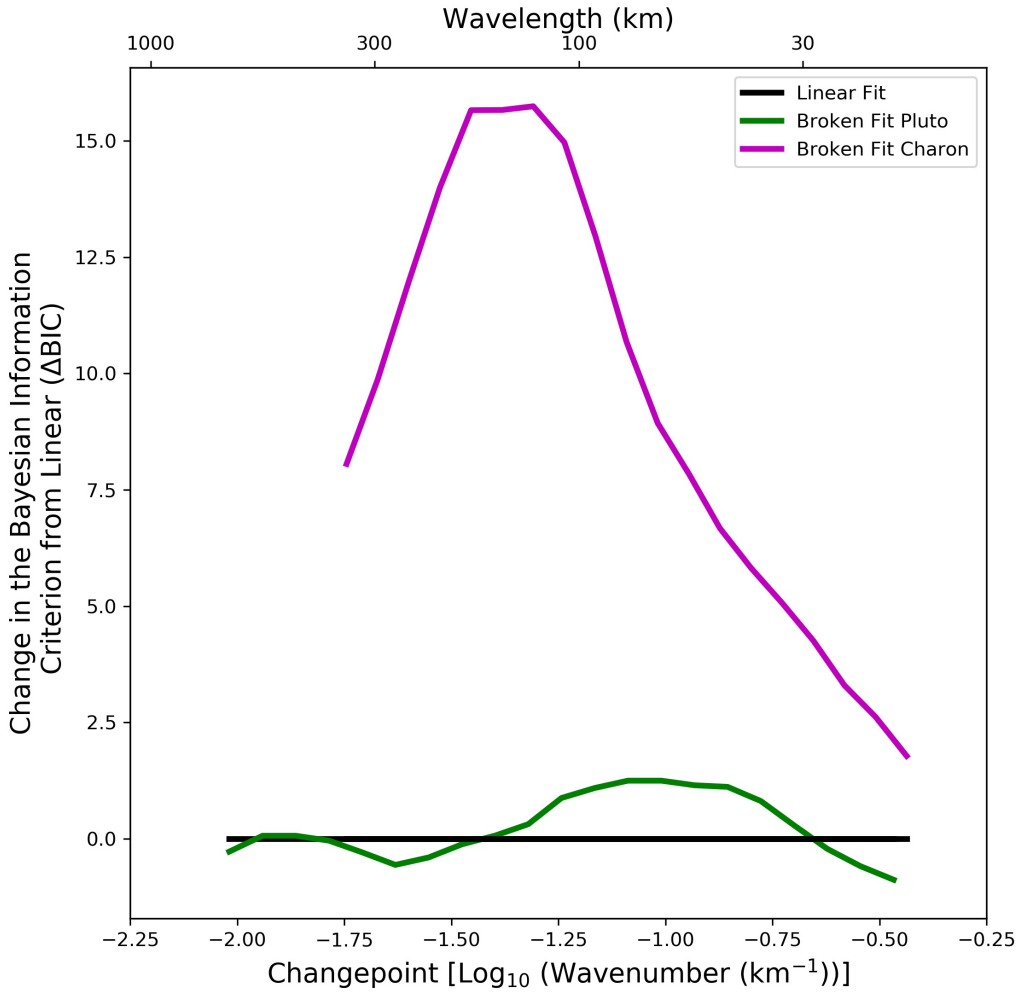

Figure 4.6: Change in the Bayesian Information Criteria from the linear fit. Hued lines are for Pluto (green) and Charon (magenta). After determining the BIC for the range of changepoints, we additionally determined the BIC for the linear fit. We consider the linear fit to be the null result, as a single power law slope is the commonly used approximation for the distribution of a solid world's topography and requires the fewest assumptions. To compare Pluto and Charon, we subtract out the linear BIC to calculate the ΔBIC. While the peak for Pluto's curve has some statistical strength (ΔBIC >2; Kass and Raftery, 1995), Charon has a stronger fit over all changepoints. The wavelength range of 70-300 km for Charon is especially significant (ΔBIC >10).

path refers to the duration and extent of strain in the ice shell. For both bodies there is extensive extensional tectonics (Moore et al. 2016; Beyer et al. 2017) on the order of $\sim$1% areal strain (less on Pluto than Charon). But the strain rate and how that strain rate changes depends on the initial state of the ice shell (thick or thin), chemistry in the subsurface ocean, or large impact events (e.g. Sputnik Planitia) to name some processes.

As we noted in the previous section, a break in the topographic variance spectrum may signal some change in the ability of the body's crust to support topography. As a rough approximation, this characteristic wavelength can be interpreted as the flexural parameter (Turcotte and Schubert, 2002). From the inferred wavelength range of 70-300 km for Charon, the implied elastic layer thickness is $\sim$15$\pm$10 km at the time of topography generation. To derive this number, we use the parameter values in Table 4.1. We note that the modern thickness of Charon's elastic layer is probably much greater as internal heating from radioactive material falls off with time (Nimmo and McKinnon 2020).

To produce a slightly more precise estimate, we can instead specify an initial topographic roughness spectrum based on the short-wavelength slope. We then treat this initial roughness as a surface load and calculate the flexural deflection at each wavelength to determine the final topographic roughness profile. The flexural deflection is calculated using either Cartesian or spherical (Turcotte et al. 1981) assumptions; this approach is identical to that used in Nimmo et al. (2011).

Table 4.1: Parameters used in chapter 4.

Parameter		Value Pluto (P), Charon (C)	Source
g	Surface acceleration due to gravity	P: 0.62 ms^{-2} C: 0.288 ms^{-2}	Stern et al. (2015)
R_0	Body Radius	P: 1188.3 km C: 606 km	Nimmo et al. (2017)
M_P	Mass of Pluto	1.3 x 10^{22}	Stern et al. (2015)
ρ_c	Load density	920 kgm^{-3}	
ρ_m	Density of the upper "mantle"	940 kgm^{-3}	
E	Young's modulus	9 x 10^9 Pa	Gammon et al. (1983)
υ	Poisson's ratio	0.3	Gammon et al. (1983)
Q	Activation energy	60[a], 49[b], 60[c] kJ/mol	see below[d]
n	Stress parameter	2.4[a], 1.8[b], 4[c]	see below[d]
A	Material parameter	a: 5.5x10^7 $MPa^{2.4}/s$ b: 3.9x10^{-3} $MPa^{1.8}m^{1.4}/s$ c: 4.0x10^{-5} MPa^4/s	see below[d]
p	Grain size parameter	0[a], 1.4[b], 0[c]	see below[d]
R	Gas constant	8.315 $JK^{-1}mol^{-1}$	
De	Deborah number	10^{-3}-10^{-4}	Mancktelow (1999)
μ	Rigidity modulus	3.46 x 10^9 Pa	$\mu = E/(2(1+\upsilon))$
d	Grain size	0.1-10 cm	Barr+McKinnon (2007)
T_s	Surface temperature	40 K	Stern et al. (2015)
κ	Thermal conductivity of pure H_2O ice	567/T Wm^{-1}	Klinger (1980)
a	Charon-Pluto initial semi-major axis	~1.5 x 10^4 km	About 75% of modern Stern et al. (2015)
k_2/Q	Estimated ratio of the Love number to the quality factor	~0.2	Upper limit; Chen and Nimmo (2008)
e	Charon's initial orbital eccentricity	10^{-1}-10^{-2}	Canup (2010)

[a] Basal slip-accommodated grain boundary sliding (GBS) regime.
[b] GBS-accommodated basal slip regime.
[c] Dislocation creep regime.
[d] Goldsby and Kohlstedt, 2001.

In detail, by calculating the compensation factor (C_l) for a range of wavelengths, we determine F_l, the ratio of the resultant topography to the initial load topography. Here l is the spherical harmonic degree, related to the wavenumber (k) by $l \approx kR_0 - 1/2$, where R_0 is the radius of the body. C_l is calculated using equation (27) from Turcotte et al. (1981) and determines the degree to which the topography is compensated by elastic and membrane support. As C_l approaches 0, the resultant topography is equivalent to the initial load topography. However, as C_l approaches 1, the resultant topography depends on the density difference between the two rheologically distinct sections of the ice shell. With the values from Table 4.1 for ρ_c, the density of the elastic section of the crust (assumed to be pure-water ice), and ρ_m, the density of the ductile ice immediately beneath the elastic layer, F_l approaches 1/47. We can use C_l to determine F_l as follows:

$$F_l = \frac{1}{1 + \left(\frac{\rho_c}{\rho_m - \rho_c}\right) C_l} \tag{4.3}$$

For our calculations we consider two approaches to calculating C_l. The first assumes a Cartesian geometry with no effects due to the sphericity of the world and the second includes membrane support from a spherical body. Once we determine F_l, we take the square of the value (F_l^2) and multiply it with an initial topographic variance spectrum that conforms to a single power law slope equal to the short-wavelength portion of Pluto or Charon's measured topographic variance spectrum. We use F_l^2 as the variance is calculated from the summed squares of the spherical harmonic coefficients. The results for both Pluto and Charon, with a variety of different possible elastic layer

thickness, are presented in Figure 4.7. For both bodies with either models an increase of ∼50 km in the elastic layer translates to about an order of magnitude increase in the topographic variance at the longest wavelengths.

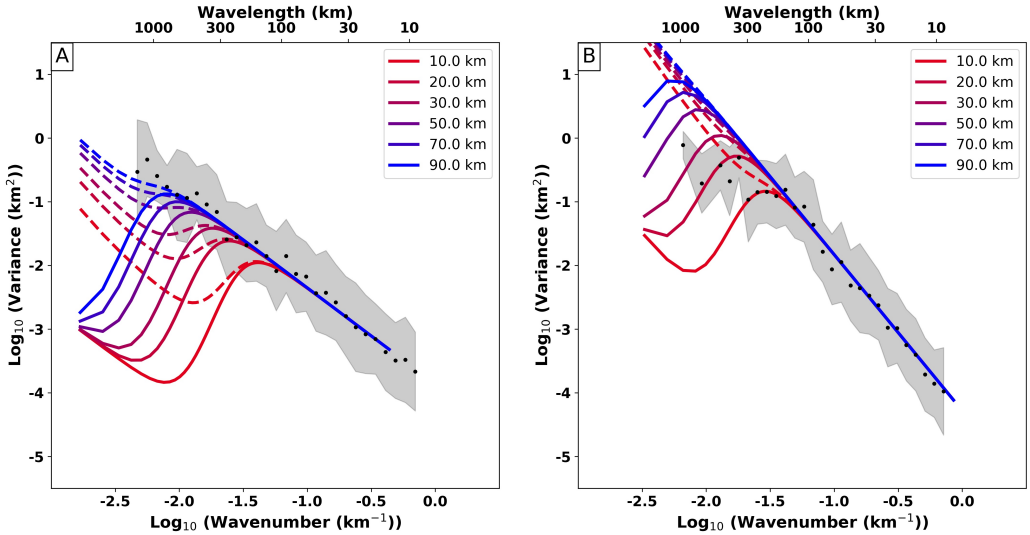

Figure 4.7: Modeled variance spectra compared with our limb profile spectra. a. Pluto's topographic variance spectrum with compensation model results overlain. The solid lines are from the cartesian model, and dashed lines are the spherical with membrane support. Lines shift in hue from red to blue as the thickness of the elastic layer increases. The primary observation of the results for Pluto are that a thicker elastic layer improves the fit of both models, but the lack of a break in slope only allows for a minimum thickness to be determined. b. Charon's topographic variance spectrum with compensation model results overlain. The solid lines are from the cartesian model, and dashed lines are the spherical with membrane support. Lines shift in hue from red to blue as the thickness of the elastic layer increases. Due to the break in slope a range of elastic thicknesses can be determined instead of a minimum as with Pluto.

Because Pluto's variance spectrum lacks a break in slope, our flexural models only place a lower bound on the elastic thickness. For either model, we would expect to see a statistically significant (Figure 4.6) break if the elastic thickness was less than ∼60 km during and after the period of topography formation. The exact timing of this is

relevant, as the elastic thickness could have been lower at times prior to the formation of the topography captured in limb profiles.

With Charon, however, the compensation model results roughly agree with the results of the straightforward assumption that the break in slope wavelength represents the flexural parameter value. The cartesian case gives a slightly higher elastic layer thickness (compared to the flexural parameter assumption) of $\sim$20$\pm$10 km, while the spherical case with membrane support implies much lower values for possible elastic thicknesses (<5 km). As we discuss below, the latter value would imply a much higher heat flux than reasonably possible (McKinnon and Nimmo, 2020), so we conclude that membrane support is not operating on Charon. The most reasonable explanation for this is that, as on the Earth, Charon's lithosphere is sufficiently fractured that long-distance transmission of membrane stresses is not possible. Since there is extensive evidence for large-scale faulting on Charon (Beyer et al. 2017) this explanation seems plausible.

4.3.4 Heat flux

With estimates for the elastic thickness – a lower bound for Pluto and a likely range for Charon - we can further estimate the thermal structure of either body's icy crust at the time of load emplacement. Although there are various methods to solve for the temperature at the base of the elastic layer (T_b), we will use the method outlined in Conrad et al. (2019; i.e. Chapter 3). We assume that any of the three most important ice deformation regimes can be dominant and as such use the cumulative strain relationship

(Goldsby and Kohlstdet, 2001).

$$\dot{\varepsilon}_{comp} = \left(\frac{1}{\dot{\varepsilon}_{gbs}} + \frac{1}{\dot{\varepsilon}_{basal}} \right)^{-1} + \dot{\varepsilon}_{dis} \tag{4.4}$$

Here $\dot{\varepsilon}$ is the strain rate (s^{-1}) and gbs, basal, dis, and comp correspond to basal slip-accommodated grain boundary sliding (GBS), GBS accommodated basal slip, dislocation creep, and composite (i.e. cumulative) respectively. The equation and respective parameters for the strain rate in each regime can be found in Goldsby and Kohlstedt (2001), but the important values we consider are T_b and σ_{crit}, the critical stress at T_b that can be determined with:

$$\sigma_{crit} = De * \mu \tag{4.5}$$

Here μ is the shear modulus of water ice and De is the Deborah number (Mancktelow, 1999), a dimensionless number that gives the strain rate where the transition from the elastic layer to the viscous layer based on the crust's Maxwell time. We use a different range of De (10^{-3} to 10^{-4}) as compared with the previous study of Pluto's heat flux (Conrad et al. 2019; 10^{-2} to 10^{3}). For the upper value of De=10^{-3}, we chose that value as it is consistent with the thermal state and measured elastic thicknesses of the terrestrial oceanic lithosphere (Watts, 2001). However, for the lower value of De=10^{-4}, we base this on our estimation of faulting-induced stresses (section 4.4.3). If we apply the maximum stress of a few hundred kPa to equation 5, we get the De of $\sim 10^{4}$.

We can now calculate $\dot{\varepsilon}$ given a set of T_b, De, and other important parameters (most notably grain size). The range of reasonable grain sizes (1 mm to 10 cm) is set

by the results of Barr and McKinnon (2007)) and the expectation that the material properties of Pluto and Charon's icy crusts will not differ much from large icy satellites. Our results for the relationship between $\dot{\varepsilon}$ and T_b are presented in Figure 4.8a and show that higher strain rates imply higher temperatures at the base of the elastic layer.

Figure 4.8a shows that as $\dot{\varepsilon}$ varies over the range of plotted values (10^{-20} s^{-1} to 10^{-14} s^{-1}), T_b can vary over 30 K. While narrowing down $\dot{\varepsilon}$ would allow for T_b to be better determined, at present, we can only define a range of reasonable values for $\dot{\varepsilon}$. Our two endmembers for the value of $\dot{\varepsilon}$ are based on likely aspects of Pluto and Charon's geophysical history. For the lowest values of $\dot{\varepsilon}$ we look at the results of thermal evolution models (e.g. Hammond et al. 2016; Bierson et al. 2018), where the strain rate is driven by the rate of freezing of the subsurface ocean. For Pluto and Charon, the amount of strain calculated by these models is $\sim$1%. If we assume that this strain is continuously generated over the extensional history of both bodies, then the strain rate is $\sim 10^{-19}$ s^{-1}. Additionally, given Charon's greater amount of strain (about twice the amount) and likely faster freezing rate the strain rate in that estimate could be higher for the moon. The high value endmember assumes that the entirety of Pluto and Charon's topography is generated by the stresses from a true polar wander event (TPW; Keane et al. 2016; Nimmo et al. 2018). If we take the timing estimate from Keane et al. (2016) of $\sim$5 million years, the strain rate should be 10^{-16} s^{-1}. From the two endmembers, our reasonable strain rates are between 10^{-19} and 10^{-16} s^{-1}. From our results in Figure 4.8a, the range of temperatures that match this range of strain rates is $\sim$117 K to 161 K.

To find the surface heat flux from the elastic layer base temperature values, we additionally need the thickness of the elastic layer (determined from the compensation analysis) and the thermal conductivity of ice (κ). We use the temperature dependent form of κ, which varies as 567/T (Klinger, 1980). Because the dual-synchronous orbit should be reached rapidly in the dynamical evolution of both bodies, we neglect any source of tidal heating in the ice shell. We do not consider effects due to porosity, although including porosity would result in a lower estimated heat flux. The heat flux F, with surface and basal temperatures T_s and T_b, respectively, is given by:

$$\frac{F}{567} = \frac{\ln(T_b/T_s)}{t_e} \tag{4.6}$$

Figure 4.8b shows how the surface heat flux depends on both the basal temperature and the elastic thickness. Contours of constant heat flux are plotted with regions that fit with our elastic thickness results highlighted in boxes. We also note the expected surface heat flux if radiogenic heat sources are the sole heating factor (~3-6 mWm^{-2}; Nimmo and McKinnon, 2020).

For Pluto, our minimum elastic thickness of 60 km gives a maximum surface heat flux since topography formation of ~13 mWm^{-2}, if we assume that all topography was generated due to TPW stresses (i.e. $\dot{\varepsilon} = 10^{-16}$ s^{-1}) and the higher temperature rheology is the active case (i.e. $De = 0.001$). In our more conservative case where the topography forms over the entire lifetime of Pluto (i.e. $\dot{\varepsilon} = 10^{-19}$ s^{-1}) with the lower temperature rheology, the maximum heat flux is reduced to ~10 mWm^{-2}. This maximum constraint is consistent with radiogenic heating estimates, and smaller compared

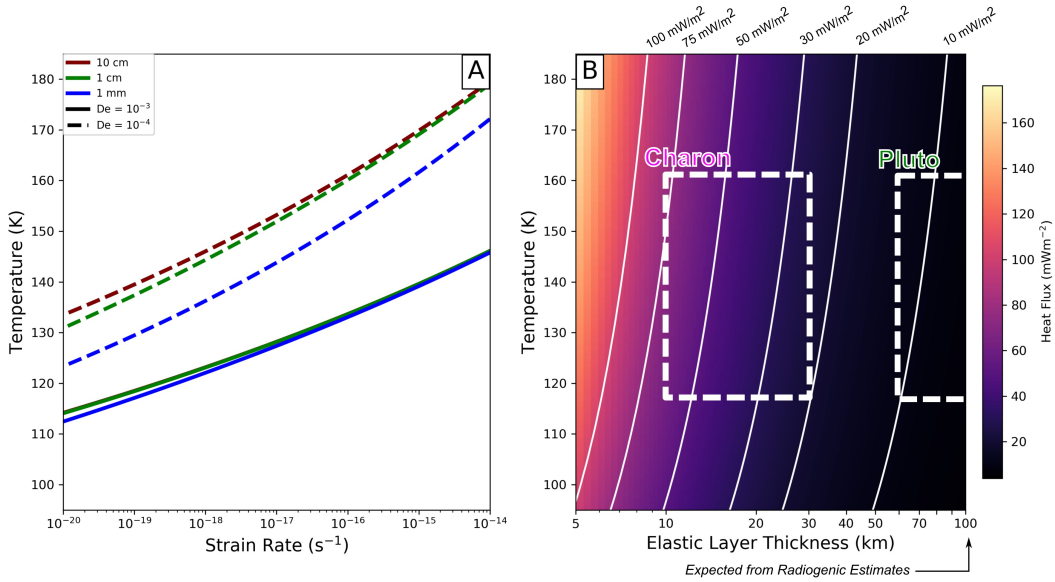

Figure 4.8: Rheologic and heat flux model results for Pluto and Charon. A. Temperature at the base of the elastic layer over a range of strain rates for a variety of rheologic parameters. The results for $De = 10^{-3}$ start to show the trade-off between the dislocation creep and grain-boundary dependent regimes. At the lower De of 10^{-4}, the transition between the same regimes and how they depend more on the grain size as grain-boundary dependence regimes starts to dominate. B. "Heat" map of surface heat flux as a function of the elastic layer thickness and basal temperature. Contours for 10, 20, 30, 50, 75 and 100 $\mathrm{mWm^{-2}}$ are plotted in white. Dashed boxes define our estimates for the possible range of heat fluxes for Pluto and Charon.

to the previous upper bound of 66-85 $\mathrm{mWm^{-2}}$ from a lack of flexural signals at Pluto's faults (Conrad et al. 2019). Although there are still individual features on the surface of Pluto, notably Edgeworth crater that may imply a higher heat flux (McKinnon et al. 2017), these are now harder to reconcile with our new, lower heat flux constraints. Conversely, these heat flux bounds are not in contradiction to the "hot start" model of Pluto (Bierson et al. 2020), as long as the topography was created at least a few tens of Myr after Pluto formed.

Since Charon has a range of possible elastic thicknesses rather than a lower bound, we can use this to determine a range of possible surface heat fluxes. For our estimate of ∼20±10 km with the range of rheological parameters, we get a heat flux range of 35^{+44}_{-15} mWm^{-2}. With a thinner elastic layer (10 km), TPW stresses (i.e. $\dot{\varepsilon}$ = 10^{-16} s^{-1}) and the higher temperature resultant rheology (i.e. De=10^{-4}), we get the high end of our surface heat flux range: 79 mWm^{-2}. This value is approximately in the same range as average surface heat fluxes for tidally heated icy satellites (e.g. Giese et al. 2007; 2008) and would require a larger heat source than can be provided by radiogenic heat production, either today or in the past. On the low end of our estimate ∼20 mWm^{-2}, which is achieved by the more conservative ice shell freezing strain rate (i.e. $\dot{\varepsilon} = 10^{-19}$ s^{-1}), a higher De of 10^{-3}, and a thicker elastic layer during topography formation (i.e. 30 km), we still have a value that is higher than radiogenic. These results suggest the existence of a heat source for Charon in addition to radiogenic heat; we will review various hypotheses for this unknown heat source in the following discussion.

4.4 Discussion

4.4.1 Early heat sources for Charon

The elastic thickness derived for Charon provides an estimate of the surface heat flux during the period of topography formation that is difficult to reconcile with results that model a purely radiogenic heat source (Bierson et al. 2018). There are a few, shorter lived, heat sources that could have increased the available heat during

topography formation. The two that we will elaborate on are heat from accretion, especially if Charon was formed in a giant impact (Canup 2010), and tidal deformation while Charon's orbit circularizes (Barr and Collins 2015; Rhoden et al. 2020).

4.4.1.1 Heat from a Charon forming impact

One of the more popular hypotheses for the formation of Charon involves a giant impact into a proto-Pluto (Canup, 2010). A newly formed Charon would either coalesce out of orbiting debris or directly form from the largest intact fragments (Arakawa et al. 2019). In either case, depending on the parameters of the impact, Charon could form partially melted. Smooth particle hydrodynamics impact simulations from Canup (2010) and Arakawa et al. (2019) record the state and temperature of particles through the simulations. Canup (2010) found that the temperature increase in the impact is concentrated towards the outer layers. This temperature increase is enough to melt around 10% of the bulk volume if the increase is focused in water ice. Melting introduces heat into the body that needs to radiate away before it can refreeze. If 10% of Charon ($\sim$1.6x10^{20} kg) melts, the energy released upon refreezing is $\sim$5x10^{25} J. On a per area basis, this would mean that $\sim 10^{13}$ Jm^{-2} needs to radiate. If we consider our moderate surface heat flux result ($\sim$35 mWm^{-2}), Charon's initial heat budget would be largely exhausted after $\sim$10 Myr. An interval of $\sim$15 Myr to generate the bulk of Charon's topography (as recorded by limb profiles) is quite short, but perhaps not completely unreasonable.

4.4.1.2 Charon tidal heating

Presently, Pluto and Charon are caught in a double tidally locked state, where they constantly face each other in their circular orbits. This orbital configuration does not cause a temporally variable tidal deformation and as a result cannot generate heat, but Charon's orbit was probably initially more inclined and/or eccentric. Either of those orbital states can generate heat if the body can be tidally deformed. However, since we do not know the initial state of the orbit, we need to assume an initial state based on formation models (Canup, 2010; Arakawa et al. 2019). Unlike the distribution of increased temperature, the range of possible eccentricities is wide. Below we neglect any obliquity tidal heating due to an initial inclination, and only look at the effect due to eccentricity tides.

Possible eccentricities for a newly formed Charon can reach values near 1.0 (Arakawa et al. 2019). Eccentricities that high would reduce rapidly, especially if Charon were molten, and the heating during these periods would be brief. Modelling the tidal evolution during this period is especially complicated given the change in the deformability and rigidity (i.e. the Q and k_2 values). To estimate the heat flux during periods of different eccentricities we use a simplified version of the equation which calculates the surface heat flux due to synchronous tidal deformation (Murray and Dermott 1999, equation 4.197):

$$HeatFlux = \left(15,320\frac{mW}{m^{-2}}\right)\left(\frac{13,720km}{a}\right)^{\frac{15}{2}}\left(\frac{k_2/Q}{0.2}\right)\left(\frac{e}{0.1}\right)^2 \tag{4.7}$$

Here the poorly constrained parameters are a, the semimajor axis of Charon's

orbit around Pluto, k_2 is the Love number, Q is the dissipation factor, and e is the eccentricity of the orbit. Estimated values for these variables are presented in Table 4.1. For a we assume a nominal initial semimajor axis about 70% of Charon's current orbit (a_{modern} ~2x10^4 km). The importance of this term is clear from the high exponent (15/2) that governs it, although we do not expect it to start much lower than our estimate. k_2/Q is the term that describes the internal structure and rigidity of the body. A lower k_2/Q signals a more rigid body that cannot deform as easily and create heat. We assume, based on the results of Arakawa et al. (2019), that Charon was initially partially molten (i.e. fluid). Following those results we look to other bodies in the solar system and base our upper limit k_2/Q for Charon on Tethys results (Chen and Nimmo 2008), since Tethys has a similar radius to Charon. This effect of this parameter is linear when applied to equation 7, although the parameter itself is highly unconstrained. A common initial eccentricity used in tidal stress studies of Charon (e.g. Rhoden et al. 2020) is 0.01. This eccentricity with a lower k_2/Q of 0.01 would yield a surface heat flux of ~8 mWm^{-2}, at least a factor of two smaller than the smallest value we estimate from our derived elastic thickness values. However, an eccentricity of 0.1, which is on the lower end of those predicted from giant impact simulations (Canup, 2010), with a k_2/Q of 0.2 would yield ~15 Wm^{-2}, a value an order of magnitude higher than present-day Io. Thus, either (or more likely) both the k_2/Q or the eccentricity must have been lower during the tidal heating period. While our derived heat fluxes during topography formation are certainly consistent with possible tidal heat production on Charon, the uncertainties in the latter are very large.

One issue with the high eccentricity estimate is that, if topographic loads were emplaced during this period, we would also expect to see the faulting of Charon fit the stress pattern caused by eccentricity tides (Rhoden et al. 2020). Rhoden et al., however, did not find a fit between their modeled stress patterns and the observed tectonics. The timing of topography formation is thus crucial: if the topography formed after Charon's orbit circularized, as Rhoden et al. (2020) postulate, then there needs to be a way for the ice shell to have remained thin once the orbit became circular. One possible solution to this problem is latent heat: tidal heating may have been stored as ice (or silicate) melts, which would provide a reservoir of heat released slowly after circularization was complete. Further investigation of Charon's early thermal evolution including tidal heat production is clearly warranted.

4.4.2 Comparisons with previous Pluto/Charon topographic variance results

The variance spectra presented in this work are the first for Pluto and Charon based on limb profile topography. However, variance spectra of Pluto and Charon have also been presented in Ermakov et al. (2018). They used the published DEMs (Schenk et al. 2018a&b) to calculate estimates for spherical harmonic coefficients. Since the DEMs only cover 30-40% of the surface area of Pluto and Charon they created their data using spectral-spatial localization techniques (Wieczorek and Simons 2005; Simons and Dahlen 2006). With those spherical harmonic coefficients, they were able to calculate the variance spectra in a similar manner as we did with Fourier series coefficients. The

major difference is that spherical harmonics are two dimensional and Fourier series have just a single dimension.

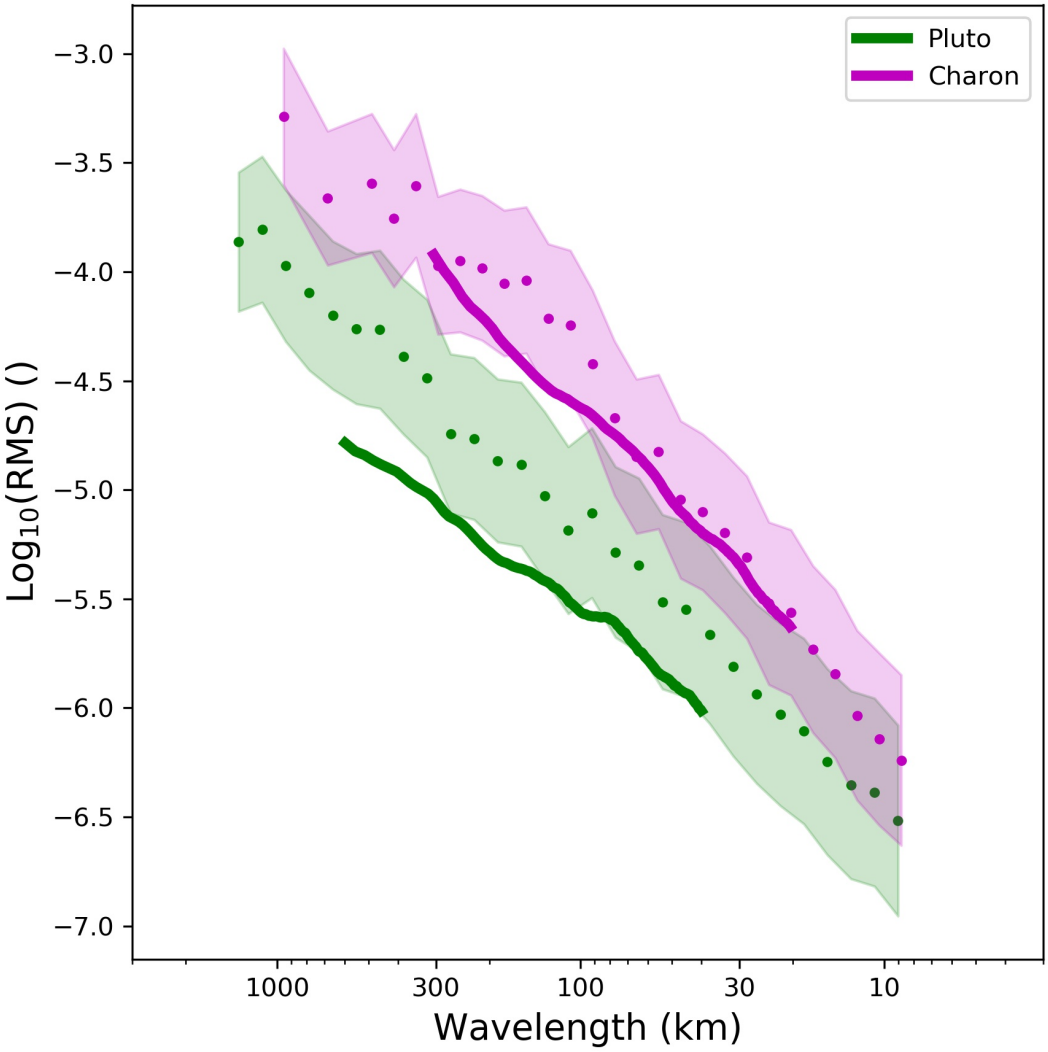

Figure 4.9: RMS spectra comparison of Ermakov et al. (2018) and this study. The data from Ermakov et al. (2018) is presented as solid lines, and the data from this study as the binned average with shaded regions of the standard deviation within the bin. Color matches those used in Figures 4.6 and 4.8b. Shorter wavelengths for Charon match well, and longer wavelengths are within the standard deviation. However, there is an observable mismatch of the values for Pluto.

Ermakov et al. (2018)'s data is available as root mean squared (RMS) values, which are normalized by the radius. These values are different from what we present in Figure 4.5, which are the (non-normalized variances) for the two worlds. Our values are useful for understanding the observed variations in the topography in kilometers, and theirs are more useful for the comparison of multiple different bodies. We convert our variance spectra to RMS spectra following equations (4), (6), and (8) from Ermakov et al. (2018). The spectral comparison is shown in Figure 4.9.

Our results for Charon show that Ermakov et al. (2018) could not have observed the break in slope given their limited wavelength range. At short wavelengths the RMS values and slopes are almost identical between the two approaches, but these diverge somewhat at long wavelengths, perhaps because of the difference between 1D and 2D analyses. However, when Pluto is compared, although the slope differences are similar to those of Charon (both limb profile spectra are steeper by $\sim$0.5 compared to DEM-derived spectra slopes), we see a large discrepancy in the RMS values. The most likely explanation for this large difference is that the geographical coverage of the two data sets is very different. In particular, the most obvious topographic feature on Pluto, Sputnik Planitia – which is very flat – is missed by our limb profiles but is a central feature of the DEM (Schenk et al. 2018a) used in Ermakov et al. (2018).

4.4.3 Stresses induced by faulting

Once the elastic thickness of a layer has been determined, we can estimate the maximum stress (σ_{max}) a fault is required to support to maintain the observed

topography. Such maximum stresses have previously been determined for Pluto (Conrad et al. 2019) and Charon (Beyer et al. 2017); the difference in this study is that the elastic thickness derived is different. We use the set of equations from Jackson and White (1989) to calculate σ_{max}:

$$\sigma_{max} = \frac{\rho_c g h}{2e} \qquad if\ \frac{\lambda}{t_e} < \frac{\pi}{2} \tag{4.8}$$

$$\sigma_{max} = \frac{3\rho_c g h \lambda}{8\pi t_e} \qquad if\ \frac{\pi}{2} < \frac{\lambda}{t_e} < \pi \tag{4.9}$$

$$\sigma_{max} = \frac{3\rho_c g h \lambda^2}{8\pi^2 t_e^2} \qquad if\ \frac{\lambda}{t_e} > \pi \tag{4.10}$$

Here $2h$ is the vertical displacement of the fault, e is the base of natural logarithms (not the orbital eccentricity), and λ is the wavelength of the faulting width (twice the trough width in most cases). All other variables are the same as described in previous equations. Stresses must support the gravitational load of the faults to maintain topography; otherwise the faults would move in such a way as to reduce the topography (Jackson and White, 1989).

For Pluto, the major faulting in Viking and Cthulhu regions have widths (i.e. $\lambda/2$) on the order of 20km and throws (i.e. $2h$) around 2km. Thus, given our minimum elastic thickness of ~60km, the largest observable faults on Pluto fall within $\lambda/t_e < \pi/2$ as λ/t_{emin} is near unity. Equation (8) is thus relevant to all faults on Pluto and implies that the value of σ_{max} ~100 kPa. This matches previous results (Conrad et al. 2019) and does not imply any significant changes to how we view those faults.

However, on Charon, our new estimate of t_e (20±10 km) is nearly an order of magnitude higher compared to previous results (2.5 km; Beyer et al. 2017). We

can take the range of observed tectonics on Charon and apply values from Table 4.1 to equations 8 through 10. For h we assume a value of 2 km from the throw of Serenity Chasma (∼4 km; Beyer et al. 2017) and for λ we use the geometry of Serenity Chasma as well (∼50 km). We find that σ_{max} ∼105 to 500 kPa, which is equal to or higher than what we infer for Pluto but at the high end is the same order of magnitude as a previous estimate for faults on Europa (Nimmo and Schenk 2006). Since the depth at which a frictional stress of 500 kPa would be reached is about 3 km on Charon, it is evident that faults on Charon need not be abnormally strong to withstand the imposed topographic stresses. This evidence for a higher value of t_e resolves the paradox noted in Beyer et al. (2017).

4.5 Conclusions

In this study we have carried out a spectral analysis of limb profile data for Pluto and Charon These data complement previously derived DEM topography (Schenk et al. 2018a&b) and provide longer baselines to analyze. The topographic variance spectra of these two bodies reveal stark differences between them in how topography is distributed over the range of observed wavelengths. While Pluto exhibits a topographic variance spectrum that can be characterized by a single slope power law, which is common for other worlds (Ermakov et al. 2018), Charon's topographic variance spectrum has a break in slope. This might imply relaxation or lack of topography with wavelengths greater than that of the break in slope. Making a flexural interpretation, we

determine that Charon had a thin elastic ice shell (t_e = 20±10 km) during the period of topography formation, which had to be driven by a high surface heat flux (35^{+44}_{-15} mWm^{-2}). This high surface heat flux requires heat sources beyond radiogenic, likely either from a giant impact formation for Charon or (more likely) tidal heating from the circularization of Charon's orbit. These constraints may be used in future work to probe the early evolution of both Pluto and Charon.

Appendix A

Supplementary Figures for Chapter 2

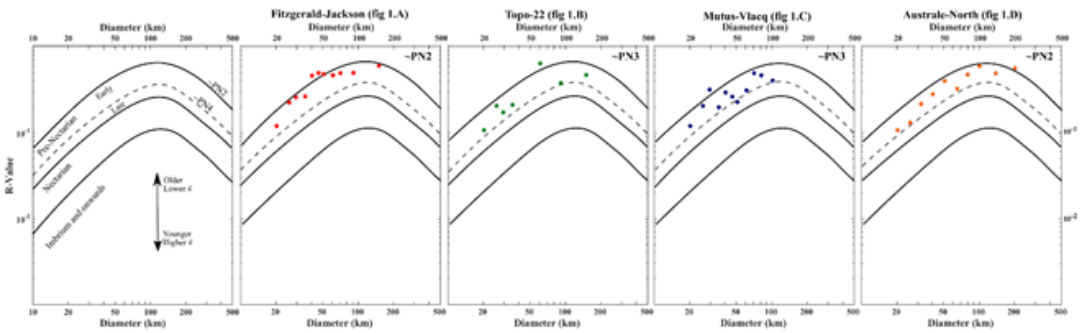

Figure A.1: R-plot variation of Figure 2.2. This is a construction similar to the one made for Figure 2.2, but instead we show the relative size-frequency plots for each proposed basin where we achieved a reasonable crater count.

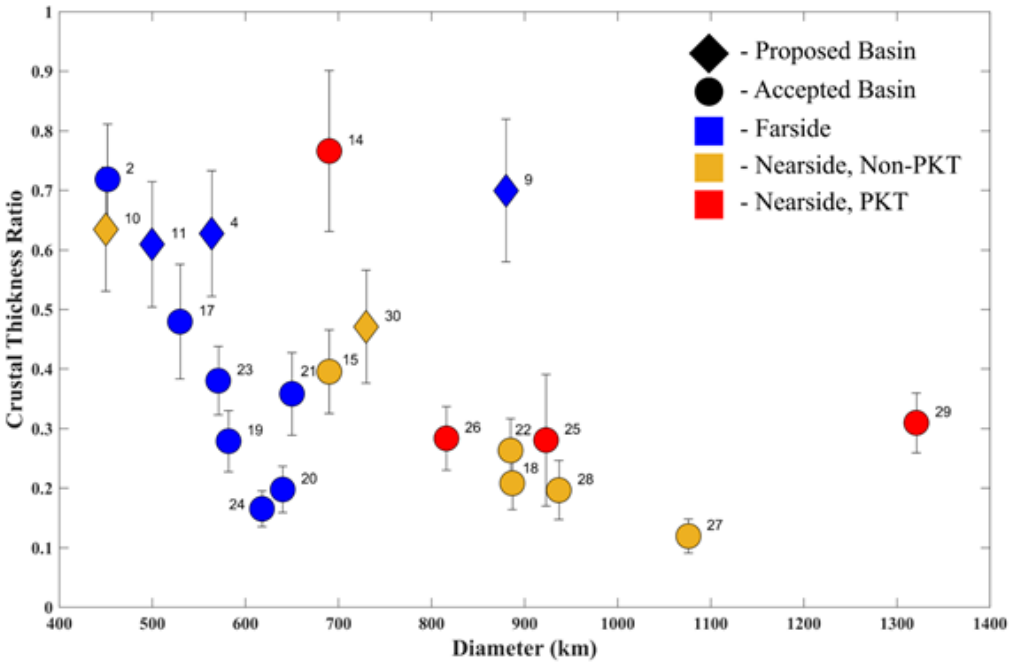

Figure A.2: Crustal Thickness Ratio Against Basin Diameter Labeled by Region. This figure is a readjustment of Figure 2.3 where the Crustal Thickness Ratio is shown as a factor of diameter and the color labeling is done by region on the Moon. Basins in the thicker farside crust are shown in blue, and the thinner crust nearside basins are shown in warm colors with yellow outside and red inside the PKT region. The Miljkovic et al. (2013) result can be clearly seen for unrelaxed basins. Any apparent trend can better be explained through age rather than location or size.

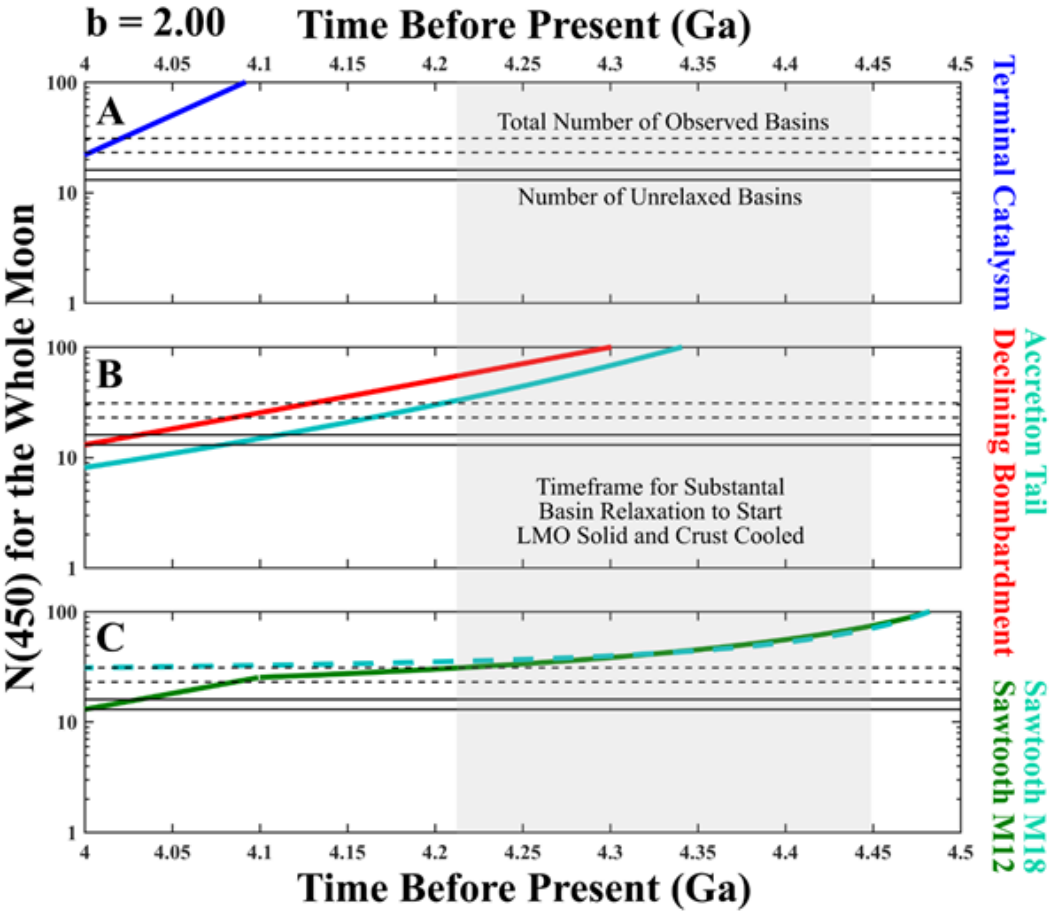

Figure A.3: A comparison of three lunar cratering chronologies assuming a scaling value of b=2.00. Same dimensions and symbolism as Figure 2.4. Lower b values imply that events happen later in lunar history.

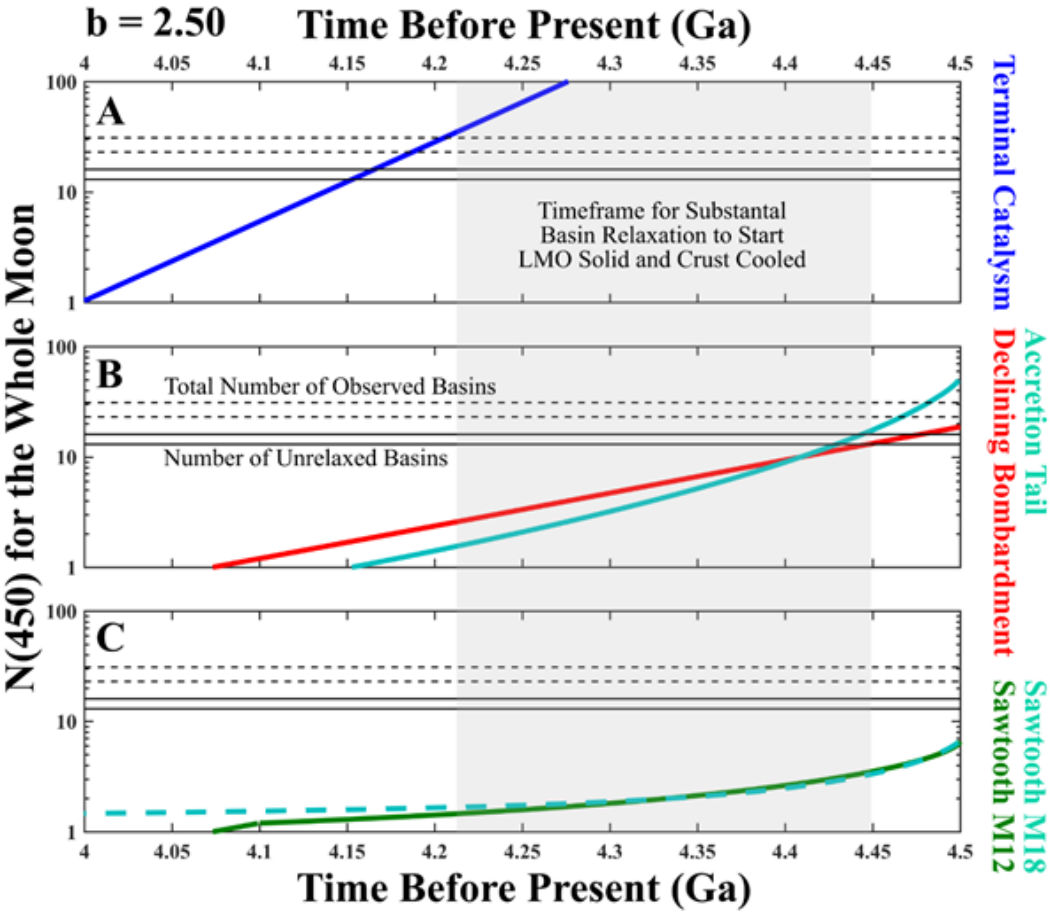

Figure A.4: A comparison of three lunar cratering chronologies assuming a scaling value of b=2.50. Same dimensions and symbolism as Figure 2.4. Higher b values imply that events happen earlier in lunar history.

Appendix B

Supplementary Figures for Chapter 3

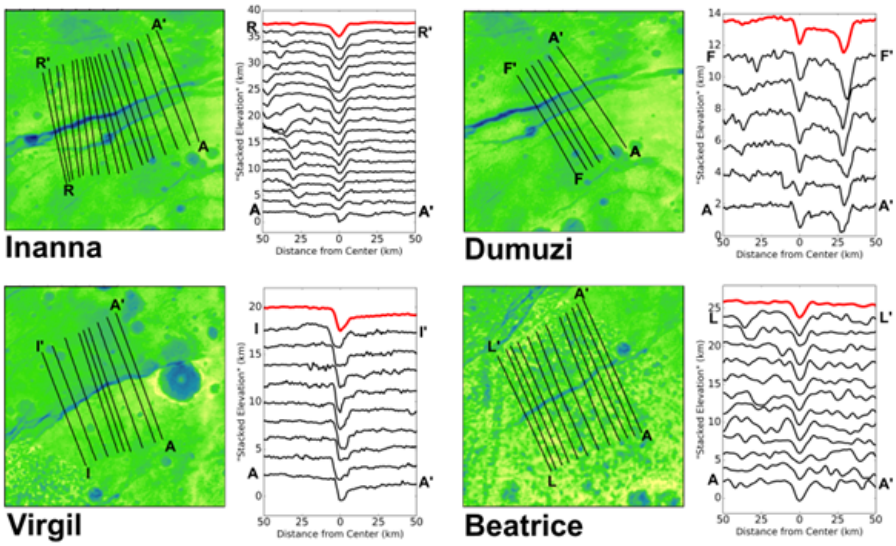

Figure B.1: Profile topography for the four major Fossa. The derived topography from Schenk et al. (2018a)'s DEM for each of our chosen profiles (black) with the average profile also included (red). Changes in fault depth along strike can be observed, especially with Inanna Fossae where the maximum depth is ∼0.5 km deeper than the average. The vertical exaggeration varies for each set of profiles but is ∼2.5 times for Inanna, ∼10 times for Dumuzi, ∼5 times each for Virgil and Beatrice Fossa.

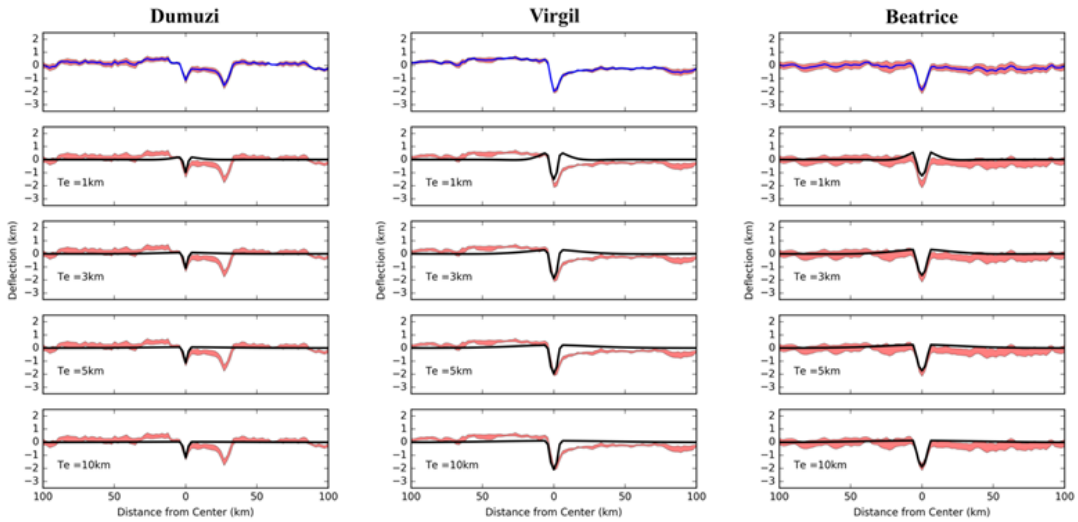

Figure B.2: Comparison of observed topography with modeled topography for Dumuzi, Virgil, and Beatrice Fossa. The uppermost plot is the averaged topographic profile of the faults we included in our study. The red area brackets the profile to show the profile's standard deviation. The lowermost four plots show the resulting model topography when the load described in this section is applied to a plate of various elastic thicknesses. As the elastic thickness increases the resulting model topography approaches the applied load shape. These may be compared to the uppermost plot. We include the red area which represents the standard deviation of the topographic profiles. Beatrice Fossae fits well starting at $t_e = 10$ km, much like Inanna Fossae. This is unlike Dumuzi Fossae for which a load profile fails to fit well. The load profile is a representative profile, while a slightly different profile was used for the north and south flanks in the RMS calculations.

Appendix C

Supplementary Data for Chapter 4

Table C.1: Pluto Image Properties. The spacecraft parameters are calculated using the most consistent SPICE information based on the smithed kernels from Schenk et al. (2018a).

ID[a]	Image MET[b]	Sub S/C[c] lat, lon (°)	Subsolar lat, lon (°)	Rotation angle[d](°)	Distance[e] (km)	GSD[f] (km/pix)
P1	299045489	42.9, 234.98	51.55, 215.91	319.08	1860388	9.234
P2	299059349	42.87, 225.99	51.55, 206.86	119.11	1669165	8.285
P3	299064419	42.86, 222.7	51.55, 203.55	118.88	1599222	7.938
P4	299067359	42.85, 220.8	51.55, 201.64	319.01	1558665	7.737
P5	299075249	42.83, 215.69	51.55, 196.49	129.07	1449832	7.196
P6	299104079	42.71, 197.1	51.55, 177.68	159.08	1052255	5.222
P7	299110129	42.67, 193.22	51.55, 173.73	110.68	968846.1	4.809
P8	299121439	42.57, 186	51.55, 166.35	171.11	812942.5	4.035
P9	299124379	42.54, 184.13	51.55, 164.43	219.91	772420.8	3.834
P10	299126909	42.51, 182.53	51.55, 162.78	201.7	737552.7	3.661
P11	299135087	42.39, 177.39	51.55, 157.45	178.51	624856.3	3.102
P12	299140025	42.29, 174.33	51.55, 154.23	191.17	556820	2.764
P13	299140073	42.29, 174.3	51.55, 154.19	191.28	556158.7	2.761
P14	299147337	42.09, 169.87	51.55, 149.45	318.88	456092.7	2.264
P15	299147481	42.08, 169.78	51.55, 149.36	318.8	454109.3	2.254
P16	299148215	42.06, 169.34	51.55, 148.88	198.76	443999.6	2.204
P17	299148263	42.05, 169.32	51.55, 148.85	198.93	443338.4	2.201
P18	299152810	41.86, 166.64	51.55, 145.88	198.48	380717.7	1.889

Continued on next page

Table C.1 – *Continued from previous page*

ID[a]	Image MET[b]	Sub S/C[c] lat, lon (°)	Subsolar lat, lon (°)	Rotation angle[d](°)	Distance[e] (km)	GSD[f] (km/pix)
P19	299152859	41.86, 166.61	51.55, 145.85	198.67	380043	1.886
P20	299167607	40.28, 159.31	51.55, 136.23	317.05	177134.1	0.879
P21	299167943	40.2, 159.21	51.55, 136.01	316.85	172519.4	0.856
P22	299168423	40.07, 159.06	51.55, 135.7	316.45	165928.4	0.823

[a] Informal image ID used in our text and figures.

[b] MET refers to spacecraft clock time.

[c] S/C stands for Spacecraft

[d] The rotation angle is the clockwise angle between the assumed body rotation pole and the image y-axis.

[e] Distance is measured from the spacecraft to the body center.

[f] Ground sample distance (GSD) at the limb is determined from spacecraft range assuming an angular resolution of 4.9636 μrad/pixel.

Table C.2: Charon Image Properties. The spacecraft parameters are calculated using the most consistent SPICE information based on the smithed kernels from Schenk et al. (2018b).

ID[a]	Image MET[b]	Sub S/C[c] lat, lon (°)	Subsolar lat, lon (°)	Rotation angle[d](°)	Distance[e] (km)	GSD[f] (km/pix)
C1	299104383	42.02, 16.52	51.55, 357.48	176.03	1062052	5.272
C2	299127274	41.49, 2.27	51.55, 342.54	201.62	747099.7	3.708
C3	299147641	40.5, 350.33	51.55, 329.26	315.63	466350.5	2.315
C4	299148419	40.43, 349.91	51.55, 328.75	197.67	455621	2.262
C5	299158958	39.19, 344.68	51.55, 321.87	201.99	310338	1.540
C6	299168679	36.19, 342	51.55, 315.53	308.23	176835.7	0.878
C7	299168727	36.16, 342	51.55, 315.5	308.3	176180.2	0.874
C8	299168967	36.03, 342	51.55, 315.34	308.06	172903.6	0.858
C9	299169015	36, 342	51.55, 315.31	307.96	172248.5	0.854
C10	299171296	34.37, 342.33	51.55, 313.82	307.86	141217.8	0.701
C11	299171335	34.34, 342.34	51.55, 313.8	307.92	140689.4	0.698

[a] Informal image ID used in our text and figures.

[b] MET refers to spacecraft clock time.

[c] S/C stands for Spacecraft

[d] The rotation angle is the clockwise angle between the assumed body rotation pole and the image y-axis.

[e] Distance is measured from the spacecraft to the body center.

[f] Ground sample distance (GSD) at the limb is determined from spacecraft range assuming an angular resolution of 4.9636 μrad/pixel.

Table C.3: Pluto limb fit parameters. The non-identification values in this table have been derived from our limb picking techniques (section 4.2.1) and are utilized in section 4.2.2.

ID	Image MET	X_0 (pix)	Y_0 (pix)	Radius (pix)
P1	299045489	577.22	561.18	127.70
P2	299059349	493.09	608.28	142.80
P3	299064419	611.10	399.13	149.02
P4	299067359	482.42	609.47	153.09
P5	299075249	639.50	552.81	163.83
P6	299104079	435.36	527.51	226.32
P7	299110129	484.55	474.56	246.24
P8	299121439	545.46	471.17	293.69
P9	299124379	458.36	548.04	309.61
P10	299126909	530.54	477.95	325.39
P11	299135087	329.16	691.28	380.80
P12	299140025	353.50	733.28	429.86
P13	299140073	747.07	740.67	431.19
P14	299147337	768.19	286.70	526.23
P15	299147481	794.52	804.35	528.85
P16	299148215	220.92	772.67	540.62
P17	299148263	854.30	726.79	540.29
P18	299152810	133.69	912.94	628.64
P19	299152859	938.96	929.00	629.86
P20	299167607	1.27E+03	-681.46	1.34E+03
P21	299167943	1.37E+03	163.81	1.44E+03
P22	299168423	1.26E+03	1.86E+03	1.45E+03

Table C.4: Charon limb fit parameters. The non-identification values in this table have been derived from our limb picking techniques (section 4.2.1) and are utilized in section 4.2.2.

ID	Image MET	X_0 (pix)	Y_0 (pix)	Radius (pix)
C1	299104383	493.22	441.55	114.85
C2	299127274	536.63	448.04	162.74
C3	299147641	484.43	539.54	261.33
C4	299148419	540.46	447.71	267.63
C5	299158958	291.67	750.60	394.33
C6	299168679	1.35E+03	81.20	693.04
C7	299168727	589.87	154.04	662.84
C8	299168967	662.03	1.01E+03	692.87
C9	299169015	1.40E+03	1.04E+03	725.50
C10	299171296	1.56E+03	395.45	865.27
C11	299171335	950.78	587.49	887.13

Bibliography

Arakawa, S., R. Hyodo, and H. Genda (Sept. 2019). "Early formation of moons around large trans-Neptunian objects via giant impacts". In: *Nature Astronomy* 3.9. Number: 9 Publisher: Nature Publishing Group, pp. 802–807. ISSN: 2397-3366. DOI: 10.1038/s41550-019-0797-9.

Araki, H. et al. (Feb. 13, 2009). "Lunar Global Shape and Polar Topography Derived from Kaguya-LALT Laser Altimetry". In: *Science* 323.5916. Publisher: American Association for the Advancement of Science Section: Report, pp. 897–900. ISSN: 0036-8075, 1095-9203. DOI: 10.1126/science.1164146.

Artemieva, N. and V. Shuvalov (2008). "Numerical simulation of high-velocity impact ejecta following falls of comets and asteroids onto the Moon". In: *Solar System Research* 42.4, pp. 329–334.

Balcerski, J., S. Hauck, A. Dombard, and E. Turtle (2010). "The influence of local thermal anomalies on large impact basin relaxation". In: *Lunar and Planetary Science Conference*. Vol. 41, p. 2535.

Baldwin, R. B. (1987). "On the relative and absolute ages of seven lunar front face basins: I. From Viscosity Arguments". In: *Icarus* 71.1, pp. 1–18.

Barboni, M. et al. (Jan. 1, 2017). "Early formation of the Moon 4.51 billion years ago". In: *Science Advances* 3.1, e1602365. ISSN: 2375-2548. DOI: 10.1126/sciadv.1602365.

Barnett, D. N. and F. Nimmo (May 1, 2002). "Strength of Faults on Mars from MOLA Topography". In: *Icarus* 157.1, pp. 34–42. ISSN: 0019-1035. DOI: 10.1006/icar.2002.6817.

Barr, A. C. and G. C. Collins (Jan. 15, 2015). "Tectonic activity on Pluto after the Charon-forming impact". In: *Icarus*. Special Issue: The Pluto System 246, pp. 146–155. ISSN: 0019-1035. DOI: 10.1016/j.icarus.2014.03.042.

Barr, A. C. and W. B. McKinnon (2007). "Convection in ice I shells and mantles with self-consistent grain size". In: *Journal of Geophysical Research: Planets* 112 (E2).

Beeman, M, W. Durham, and S. Kirby (1988). "Friction of ice". In: *Journal of Geophysical Research: Solid Earth* 93 (B7), pp. 7625–7633.

Bevington, P. R., D. K. Robinson, J. M. Blair, A. J. Mallinckrodt, and S. McKay (July 1, 1993). "Data Reduction and Error Analysis for the Physical Sciences". In: *Computers in Physics* 7.4. Publisher: American Institute of Physics, pp. 415–416. ISSN: 0894-1866. DOI: 10.1063/1.4823194.

Beyer, R. A. et al. (May 1, 2017). "Charon tectonics". In: *Icarus*. Special Issue: The Pluto System 287, pp. 161–174. ISSN: 0019-1035. DOI: 10.1016/j.icarus.2016.12.018.

Bierson, C. J., F. Nimmo, and W. B. McKinnon (July 15, 2018). "Implications of the observed Pluto–Charon density contrast". In: *Icarus* 309, pp. 207–219. ISSN: 0019-1035. DOI: 10.1016/j.icarus.2018.03.007.

Bierson, C. J. and F. Nimmo (July 2020). "Explaining the Galilean Satellites' Density Gradient by Hydrodynamic Escape". In: *The Astrophysical Journal* 897.2. Publisher: American Astronomical Society, p. L43. ISSN: 2041-8205. DOI: 10.3847/2041-8213/aba11a.

Bierson, C. J., F. Nimmo, and S. A. Stern (July 2020). "Evidence for a hot start and early ocean formation on Pluto". In: *Nature Geoscience* 13.7. Number: 7 Publisher: Nature Publishing Group, pp. 468–472. ISSN: 1752-0908. DOI: 10.1038/s41561-020-0595-0.

Bottke, W. F. and M. D. Norman (2017). "The Late Heavy Bombardment". In: *Annual Review of Earth and Planetary Sciences* 45.1.

Bottke, W. F., R. J. Walker, J. M. Day, D. Nesvorny, and L. Elkins-Tanton (2010). "Stochastic late accretion to Earth, the Moon, and Mars". In: *science* 330.6010, pp. 1527–1530.

Bottke, W. F. et al. (2012). "An Archaean heavy bombardment from a destabilized extension of the asteroid belt". In: *Nature* 485.7396, p. 78.

Brown, C. D. and R. J. Phillips (1999). "Flexural rift flank uplift at the Rio Grande rift, New Mexico". In: *Tectonics* 18.6, pp. 1275–1291. ISSN: 1944-9194. DOI: 10.1029/1999TC900031.

Buratti, B. J. et al. (May 1, 2017). "Global albedos of Pluto and Charon from LORRI New Horizons observations". In: *Icarus*. Special Issue: The Pluto System 287, pp. 207–217. ISSN: 0019-1035. DOI: 10.1016/j.icarus.2016.11.012.

Canup, R. M. (Dec. 2010). "On a Giant Impact Origin of Charon, Nix, and Hydra". In: *The Astronomical Journal* 141.2. Publisher: IOP Publishing, p. 35. ISSN: 1538-3881. DOI: 10.1088/0004-6256/141/2/35.

Chen, E. M. A. and F. Nimmo (2008). "Implications from Ithaca Chasma for the thermal and orbital history of Tethys". In: *Geophysical Research Letters* 35.19. _eprint: https://agupubs.onlinelibrary.wiley.com/doi/pdf/10.1029/2008GL035402. ISSN: 1944-8007. DOI: 10.1029/2008GL035402.

Cheng, A. F. et al. (2009). "Long-Range Reconnaissance Imager on New Horizons". In: *New Horizons: Reconnaissance of the Pluto-Charon System and the Kuiper Belt*. Ed. by C. T. Russell. New York, NY: Springer, pp. 189–215. ISBN: 978-0-387-89518-5. DOI: 10.1007/978-0-387-89518-5_9.

Cohen, B., T. Swindle, and D. Kring (2000). "Support for the lunar cataclysm hypothesis from lunar meteorite impact melt ages". In: *Science* 290.5497, pp. 1754–1756.

Conrad, J. W. et al. (Aug. 1, 2019). "An upper bound on Pluto's heat flux from a lack of flexural response of its normal faults". In: *Icarus* 328, pp. 210–217. ISSN: 0019-1035. DOI: 10.1016/j.icarus.2019.03.028.

Cook, A., P. Spudis, M. Robinson, and T. Watters (2002). "Lunar topography and basins mapped using a Clementine stereo digital elevation model". In: *Lunar and Planetary Science Conference*. Vol. 33.

Day, J. M. and R. J. Walker (2015). "Highly siderophile element depletion in the Moon". In: *Earth and Planetary Science Letters* 423, pp. 114–124.

Day, J. M., D. G. Pearson, and L. A. Taylor (2007). "Highly siderophile element constraints on accretion and differentiation of the Earth-Moon system". In: *Science* 315.5809, pp. 217–219.

Dermott, S. F. and P. C. Thomas (Jan. 1, 1988). "The shape and internal structure of Mimas". In: *Icarus* 73.1, pp. 25–65. ISSN: 0019-1035. DOI: 10.1016/0019-1035(88)90084-X.

Dombard, A. J., S. A. Hauck, and J. A. Balcerski (2013). "On the origin of mascon basins on the Moon (and beyond)". In: *Geophysical Research Letters* 40.1, pp. 28–32.

Elkins-Tanton, L. T., S. Burgess, and Q.-Z. Yin (Apr. 15, 2011). "The lunar magma ocean: Reconciling the solidification process with lunar petrology and geochronology". In: *Earth and Planetary Science Letters* 304.3, pp. 326–336. ISSN: 0012-821X. DOI: 10.1016/j.epsl.2011.02.004.

Ermakov, A. I., R. S. Park, and B. G. Bills (2018). "Power Laws of Topography and Gravity Spectra of the Solar System Bodies". In: *Journal of Geophysical Research: Planets* 123.8, pp. 2038–2064. ISSN: 2169-9100. DOI: 10.1029/2018JE005562.

Fassett, C. I. and J. W. Head (2008). "The timing of martian valley network activity: Constraints from buffered crater counting". In: *Icarus* 195.1, pp. 61–89.

Fassett, C. I. and B. J. Thomson (2014). "Crater degradation on the lunar maria: Topographic diffusion and the rate of erosion on the Moon". In: *Journal of Geophysical Research: Planets* 119.10, pp. 2255–2271.

Fassett, C. et al. (2012). "Lunar impact basins: Stratigraphy, sequence and ages from superposed impact crater populations measured from Lunar Orbiter Laser Altimeter (LOLA) data". In: *Journal of Geophysical Research: Planets* 117 (E12).

Foster, A. and F. Nimmo (Sept. 1, 1996). "Comparisons between the rift systems of East Africa, Earth and Beta Regio, Venus". In: *Earth and Planetary Science Letters* 143.1, pp. 183–195. ISSN: 0012-821X. DOI: 10.1016/0012-821X(96)00146-X.

Freed, A. M. et al. (2014). "The formation of lunar mascon basins from impact to contemporary form". In: *Journal of Geophysical Research: Planets* 119.11, pp. 2378–2397.

Frey, H. (2011). "Previously unknown large impact basins on the Moon: Implications for lunar stratigraphy". In: *Geological Society of America Special Papers* 477, pp. 53–75.

Fu, R. R. et al. (Oct. 15, 2017). "The interior structure of Ceres as revealed by surface topography". In: *Earth and Planetary Science Letters* 476, pp. 153–164. ISSN: 0012-821X. DOI: 10.1016/j.epsl.2017.07.053.

Gammon, P. H., H. Kiefte, and M. J. Clouter (Oct. 1, 1983). "Elastic constants of ice samples by Brillouin spectroscopy". In: *The Journal of Physical Chemistry* 87.21, pp. 4025–4029. ISSN: 0022-3654. DOI: 10.1021/j100244a004.

Giese, B., R. Wagner, G. Neukum, P. Helfenstein, and P. C. Thomas (2007). "Tethys: Lithospheric thickness and heat flux from flexurally supported topography at Ithaca Chasma". In: *Geophysical Research Letters* 34.21. ISSN: 1944-8007. DOI: 10.1029/2007GL031467.

Giese, B. et al. (2008). "Enceladus: An estimate of heat flux and lithospheric thickness from flexurally supported topography". In: *Geophysical Research Letters* 35.24. ISSN: 1944-8007. DOI: 10.1029/2008GL036149.

Goldsby, D. and D. Kohlstedt (2001). "Superplastic deformation of ice: Experimental observations". In: *Journal of Geophysical Research: Solid Earth* 106 (B6), pp. 11017–11030.

Gomes, R., H. F. Levison, K. Tsiganis, and A. Morbidelli (2005). "Origin of the cataclysmic Late Heavy Bombardment period of the terrestrial planets". In: *Nature* 435.7041, p. 466.

Greenstreet, S., B. Gladman, and W. B. McKinnon (2015). "Impact and cratering rates onto Pluto". In: *Icarus* 258, pp. 267–288.

Group, C. A. T. W. (1979). "Standard techniques for presentation and analysis of crater size-frequency data". In: *Icarus* 37.2, pp. 467–474.

Hammond, N. P., A. C. Barr, and E. M. Parmentier (2016). "Recent tectonic activity on Pluto driven by phase changes in the ice shell". In: *Geophysical Research Letters* 43.13, pp. 6775–6782. ISSN: 1944-8007. DOI: 10.1002/2016GL069220.

Hartmann, W. K. (1999). “Martian cratering VI: Crater count isochrons and evidence for recent volcanism from Mars Global Surveyor”. In: *Meteoritics & Planetary Science* 34.2, pp. 167–177.

Hartmann, W., G. Ryder, L. Dones, and D. Grinspoon (2000). “The time-dependent intense bombardment of the primordial Earth/Moon system”. In: *Origin of the Earth and Moon*, pp. 493–512.

Head, J. W. et al. (2010). “Global distribution of large lunar craters: Implications for resurfacing and impactor populations”. In: *science* 329.5998, pp. 1504–1507.

Hirabayashi, M., D. A. Minton, and C. I. Fassett (2017). “An analytical model of crater count equilibrium”. In: *Icarus* 289, pp. 134–143.

Hoppa, G. V., B. R. Tufts, R. Greenberg, and P. E. Geissler (1999). “Formation of cycloidal features on Europa”. In: *Science* 285.5435, pp. 1899–1902.

Jackson, J. and N. White (1989). “Normal faulting in the upper continental crust: observations from regions of active extension”. In: *Journal of Structural Geology* 11.1, pp. 15–36.

Johnson, B. C. et al. (2016). “Spherule layers, crater scaling laws, and the population of ancient terrestrial impactors”. In: *Icarus* 271, pp. 350–359.

Johnson, C. L. and D. T. Sandwell (Nov. 1, 1994). “Lithospheric flexure on Venus”. In: *Geophysical Journal International* 119.2, pp. 627–647. ISSN: 0956-540X. DOI: 10.1111/j.1365-246X.1994.tb00146.x.

Jolliff, B. L. et al. (2000). "New views of the Moon: Improved understanding through data integration". In: *Eos, Transactions American Geophysical Union* 81.31, pp. 349–355.

Jutzi, M. and E Asphaug (2011). "Forming the lunar farside highlands by accretion of a companion moon". In: *Nature* 476.7358, p. 69.

Kadel, S. D., F. C. Chuang, R. Greeley, and J. M. Moore (2000). "Geological history of the Tyre region of Europa: A regional perspective on Europan surface features and ice thickness". In: *Journal of Geophysical Research: Planets* 105 (E9), pp. 22657–22669.

Kadish, S. et al. (2011). "A Global Catalog of Large Lunar Craters (>= 20 km) from the Lunar Orbiter Laser Altimeter". In: *Lunar and Planetary Science Conference.* Vol. 42, p. 1006.

Kamata, S. et al. (2013). "Viscoelastic deformation of lunar impact basins: Implications for heterogeneity in the deep crustal paleo-thermal state and radioactive element concentration". In: *Journal of Geophysical Research: Planets* 118.3, pp. 398–415.

Kamata, S. et al. (Apr. 2015). "The relative timing of Lunar Magma Ocean solidification and the Late Heavy Bombardment inferred from highly degraded impact basin structures". In: *Icarus* 250, pp. 492–503. ISSN: 00191035. DOI: `10.1016/j.icarus.2014.12.025`.

Karato, S.-i. (2012). *Deformation of earth materials: an introduction to the rheology of solid earth.* Cambridge University Press.

Kass, R. E. and A. E. Raftery (June 1, 1995). "Bayes Factors". In: *Journal of the American Statistical Association* 90.430. Publisher: Taylor & Francis _eprint: https://www.tandfonline.com/doi/pdf/10.1080/01621459.1995.10476572, pp. 773–795. ISSN: 0162-1459. DOI: 10.1080/01621459.1995.10476572.

Keane, J. T., I. Matsuyama, S. Kamata, and J. K. Steckloff (2016). "Reorientation and faulting of Pluto due to volatile loading within Sputnik Planitia". In: *Nature* 540.7631, p. 90.

Klinger, J (1980). "Influence of a phase transition of ice on the heat and mass balance of comets". In: *Science* 209, p. 271.

Kneissl, T, G. Michael, T Platz, and S. Walter (2015). "Age determination of linear surface features using the Buffered Crater Counting approach–Case studies of the Sirenum and Fortuna Fossae graben systems on Mars". In: *Icarus* 250, pp. 384–394.

Kneissl, T., S. van Gasselt, and G. Neukum (2011). "Map-projection-independent crater size-frequency determination in GIS environments—New software tool for ArcGIS". In: *Planetary and Space Science* 59.11, pp. 1243–1254.

Korotev, R. L. (2000). "The great lunar hot spot and the composition and origin of the Apollo mafic ("LKFM") impact-melt breccias". In: *Journal of Geophysical Research: Planets* 105 (E2), pp. 4317–4345.

Kruijer, T. S. and T. Kleine (Oct. 1, 2017). "Tungsten isotopes and the origin of the Moon". In: *Earth and Planetary Science Letters* 475, pp. 15–24. ISSN: 0012-821X. DOI: 10.1016/j.epsl.2017.07.021.

Kusznir, N. J., G. Marsden, and S. S. Egan (Jan. 1, 1991). "A flexural-cantilever simple-shear/pure-shear model of continental lithosphere extension: applications to the Jeanne d'Arc Basin, Grand Banks and Viking Graben, North Sea". In: *Geological Society, London, Special Publications* 56.1, pp. 41–60. ISSN: 0305-8719, 2041-4927. DOI: 10.1144/GSL.SP.1991.056.01.04.

Laneuville, M., M. Wieczorek, D. Breuer, and N. Tosi (2013). "Asymmetric thermal evolution of the Moon". In: *Journal of Geophysical Research: Planets* 118.7, pp. 1435–1452.

Main, I. G., T. Leonard, O. Papasouliotis, C. G. Hatton, and P. G. Meredith (1999). "One slope or two? Detecting statistically significant breaks of slope in geophysical data, with application to fracture scaling relationships". In: *Geophysical Research Letters* 26.18, pp. 2801–2804. ISSN: 1944-8007. DOI: 10.1029/1999GL005372.

Mancktelow, N. (1999). "Finite-element modelling of single-layer folding in elasto-viscous materials: the effect of initial perturbation geometry". In: *Journal of Structural Geology* 21.2, pp. 161–177.

Marchi, S, R. Canup, and R. Walker (2018). "Heterogeneous delivery of silicate and metal to the Earth by large planetesimals". In: *Nature Geoscience* 11.1, p. 77.

Marchi, S., W. F. Bottke, D. A. Kring, and A. Morbidelli (2012). "The onset of the lunar cataclysm as recorded in its ancient crater populations". In: *Earth and Planetary Science Letters* 325, pp. 27–38.

McCoy, T. J., D. W. Mittlefehldt, and L. Wilson (2006). "Asteroid differentiation". In: *Meteorites and the early solar system II*, pp. 733–745.

McEwen, A. S. and E. B. Bierhaus (2006). "The importance of secondary cratering to age constraints on planetary surfaces". In: *Annu. Rev. Earth Planet. Sci.* 34, pp. 535–567.

McKenzie, D. and C. Bowin (Apr. 10, 1976). "The relationship between bathymetry and gravity in the Atlantic Ocean". In: *Journal of Geophysical Research* 81.11, pp. 1903–1915. ISSN: 2156-2202. DOI: 10.1029/JB081i011p01903.

McKenzie, D., F. Nimmo, J. A. Jackson, P. Gans, and E. Miller (2000). "Characteristics and consequences of flow in the lower crust". In: *Journal of Geophysical Research: Solid Earth* 105 (B5), pp. 11029–11046.

McKinnon, W. et al. (2018). "Pluto's Heat Flow: A Mystery Wrapped in an Ocean Inside an Ice Shell". In: *Lunar and Planetary Science Conference*. Vol. 49.

McKinnon, W. B. et al. (2016). "Convection in a volatile nitrogen-ice-rich layer drives Pluto's geological vigour". In: *Nature* 534.7605, p. 82.

Melosh, H. et al. (2013). "The origin of lunar mascon basins". In: *Science* 340.6140, pp. 1552–1555.

Meyer, J., L. Elkins-Tanton, and J. Wisdom (July 1, 2010). "Coupled thermal–orbital evolution of the early Moon". In: *Icarus* 208.1, pp. 1–10. ISSN: 0019-1035. DOI: 10.1016/j.icarus.2010.01.029.

Michael, G., A. Basilevsky, and G. Neukum (2018). "On the history of the early meteoritic bombardment of the Moon: Was there a terminal lunar cataclysm?" In: *Icarus* 302, pp. 80–103.

Miljković, K et al. (2016). "Subsurface morphology and scaling of lunar impact basins". In: *Journal of Geophysical Research: Planets* 121.9, pp. 1695–1712.

Miljković, K. et al. (2013). "Asymmetric distribution of lunar impact basins caused by variations in target properties". In: *Science* 342.6159, pp. 724–726.

Miljkovic, K, M. Wieczorek, M Laneuville, P. Bland, and M. Zuber (2017). "Elusive Formation of Impact Basins on the Young Moon". In: *Lunar and Planetary Science Conference*. Vol. 48.

Minton, D. A., J. E. Richardson, and C. I. Fassett (2015). "Re-examining the main asteroid belt as the primary source of ancient lunar craters". In: *Icarus* 247, pp. 172–190.

Moore, J. M. et al. (2004). "Callisto". In: *Jupiter. The planet, satellites and magnetosphere* 1, pp. 397–426.

Moore, J. M. et al. (2016). "The geology of Pluto and Charon through the eyes of New Horizons". In: *Science* 351.6279, pp. 1284–1293.

Moore, J. M. et al. (2018). "Bladed Terrain on Pluto: Possible origins and evolution". In: *Icarus* 300, pp. 129–144.

Morbidelli, A. et al. (May 1, 2018). "The timeline of the lunar bombardment: Revisited". In: *Icarus* 305, pp. 262–276. ISSN: 0019-1035. DOI: 10.1016/j.icarus.2017.12.046.

Morbidelli, A., H. F. Levison, K. Tsiganis, and R. Gomes (2005). "Chaotic capture of Jupiter's Trojan asteroids in the early Solar System". In: *Nature* 435.7041, p. 462.

Morbidelli, A., R. Brasser, R. Gomes, H. F. Levison, and K. Tsiganis (2010). "Evidence from the asteroid belt for a violent past evolution of Jupiter's orbit". In: *The Astronomical Journal* 140.5, p. 1391.

Morbidelli, A., S. Marchi, W. F. Bottke, and D. A. Kring (2012). "A sawtooth-like timeline for the first billion years of lunar bombardment". In: *Earth and Planetary Science Letters* 355, pp. 144–151.

Murray, C. D. and S. F. Dermott (1999). *Solar System Dynamics*. Google-Books-ID: aU6vcy5L8GAC. Cambridge University Press. 612 pp. ISBN: 978-0-521-57597-3.

Neukum, G., B. König, and J. Arkani-Hamed (1975). "A study of lunar impact crater size-distributions". In: *Earth, Moon, and Planets* 12.2, pp. 201–229.

Neukum, G., B. A. Ivanov, and W. K. Hartmann (2001). "Cratering records in the inner solar system in relation to the lunar reference system". In: *Chronology and evolution of Mars*. Springer, pp. 55–86.

Neumann, G. A., M. T. Zuber, D. E. Smith, and F. G. Lemoine (1996). "The lunar crust: Global structure and signature of major basins". In: *Journal of Geophysical Research: Planets* 101 (E7), pp. 16841–16863.

Neumann, G. A. et al. (2015). "Lunar impact basins revealed by Gravity Recovery and Interior Laboratory measurements". In: *Science advances* 1.9, e1500852.

Nimmo, F. and W. B. McKinnon (2020). "Pluto's Thermal History." In: *The Pluto System*. Unversity of Arizona Press.

Nimmo, F. and P. Schenk (Dec. 1, 2006). "Normal faulting on Europa: implications for ice shell properties". In: *Journal of Structural Geology*. Faulting and fault-related processes on planetary surfaces 28.12, pp. 2194–2203. ISSN: 0191-8141. DOI: 10.1016/j.jsg.2005.08.009.

Nimmo, F., B. G. Bills, P. C. Thomas, and S. W. Asmar (Oct. 1, 2010). "Geophysical implications of the long-wavelength topography of Rhea". In: *Journal of Geophysical Research (Planets)* 115, E10008. ISSN: 0148-0227. DOI: 10.1029/2010JE003604.

Nimmo, F., B. G. Bills, and P. C. Thomas (2011). "Geophysical implications of the long-wavelength topography of the Saturnian satellites". In: *Journal of Geophysical Research: Planets* 116 (E11). _eprint: https://agupubs.onlinelibrary.wiley.com/doi/pdf/10.1029 ISSN: 2156-2202. DOI: 10.1029/2011JE003835.

Nimmo, F. et al. (Dec. 2016). "Reorientation of Sputnik Planitia implies a subsurface ocean on Pluto". In: *Nature* 540.7631. Number: 7631 Publisher: Nature Publishing Group, pp. 94–96. ISSN: 1476-4687. DOI: 10.1038/nature20148.

Nimmo, F., R. T. Pappalardo, and B. Giese (2002). "Effective elastic thickness and heat flux estimates on Ganymede". In: *Geophysical Research Letters* 29.7, pp. 62–1–62–4. ISSN: 1944-8007. DOI: 10.1029/2001GL013976.

Nimmo, F. et al. (May 1, 2017). "Mean radius and shape of Pluto and Charon from New Horizons images". In: *Icarus*. Special Issue: The Pluto System 287, pp. 12–29. ISSN: 0019-1035. DOI: 10.1016/j.icarus.2016.06.027.

Peterson, G., F. Nimmo, and P. Schenk (Apr. 1, 2015). "Elastic thickness and heat flux estimates for the uranian satellite Ariel". In: *Icarus* 250, pp. 116–122. ISSN: 0019-1035. DOI: 10.1016/j.icarus.2014.11.007.

Potter, R. W., G. S. Collins, W. S. Kiefer, P. J. McGovern, and D. A. Kring (2012). "Constraining the size of the South Pole-Aitken basin impact". In: *Icarus* 220.2, pp. 730–743.

Press, W. H. (1992). *Numerical Recipes in Fortran 77: The Art of Scientific Computing*. Cambridge University Press. ISBN: 978-0-521-43064-7.

Reuter, D. C. et al. (Oct. 1, 2008). "Ralph: A Visible/Infrared Imager for the New Horizons Pluto/Kuiper Belt Mission". In: *Space Science Reviews* 140.1, pp. 129–154. ISSN: 1572-9672. DOI: 10.1007/s11214-008-9375-7.

Rhoden, A. R. et al. (2020). "Charon: A Brief History of Tides". In: *Journal of Geophysical Research: Planets* 125.7. _eprint: https://agupubs.onlinelibrary.wiley.com/doi/pdf/10.1029/e2020JE006449. ISSN: 2169-9100. DOI: 10.1029/2020JE006449.

Robbins, S. J. (2014). "New crater calibrations for the lunar crater-age chronology". In: *Earth and Planetary Science Letters* 403, pp. 188–198.

Robuchon, G. and F. Nimmo (Dec. 1, 2011). "Thermal evolution of Pluto and implications for surface tectonics and a subsurface ocean". In: *Icarus* 216.2, pp. 426–439. ISSN: 0019-1035. DOI: 10.1016/j.icarus.2011.08.015.

Rubie, D. C. et al. (2016). "Highly siderophile elements were stripped from Earth's mantle by iron sulfide segregation". In: *Science* 353.6304, pp. 1141–1144.

Schenk, P. M. et al. (Nov. 1, 2018a). "Basins, fractures and volcanoes: Global cartography and topography of Pluto from New Horizons". In: *Icarus* 314, pp. 400–433. ISSN: 0019-1035. DOI: 10.1016/j.icarus.2018.06.008.

Schenk, P. M. et al. (Nov. 15, 2018b). "Breaking up is hard to do: Global cartography and topography of Pluto's mid-sized icy Moon Charon from New Horizons". In: *Icarus* 315, pp. 124–145. ISSN: 0019-1035. DOI: 10.1016/j.icarus.2018.06.010.

Schultz, R. A., C. H. Okubo, and S. J. Wilkins (2006). "Displacement-length scaling relations for faults on the terrestrial planets". In: *Journal of Structural Geology* 28.12, pp. 2182–2193.

Shepard, M. K. et al. (2001). "The roughness of natural terrain: A planetary and remote sensing perspective". In: *Journal of Geophysical Research: Planets* 106 (E12). _eprint: https://agupubs.onlinelibrary.wiley.com/doi/pdf/10.1029/2000JE001429, pp. 32777–32795. ISSN: 2156-2202. DOI: 10.1029/2000JE001429.

Simons, F. J. and F. A. Dahlen (Sept. 1, 2006). "Spherical Slepian functions and the polar gap in geodesy". In: *Geophysical Journal International* 166.3. Publisher: Oxford Academic, pp. 1039–1061. ISSN: 0956-540X. DOI: 10.1111/j.1365-246X.2006.03065.x.

Snyder, J. P. (1987). *Map Projections–a Working Manual*. Google-Books-ID: nPdOAAAAMAAJ. U.S. Government Printing Office. 410 pp.

Solomon, S. C., R. P. Comer, and J. W. Head (1982). "The evolution of impact basins: Viscous relaxation of topographic relief". In: *Journal of Geophysical Research* 87 (B5), pp. 3975–3992.

Sori, M. M., M. T. Zuber, J. W. Head, and W. S. Kiefer (2016). "Gravitational search for cryptovolcanism on the Moon: Evidence for large volumes of early igneous activity". In: *Icarus* 273, pp. 284–295.

Spencer, J. R. et al. (Feb. 28, 2020). "The geology and geophysics of Kuiper Belt object (486958) Arrokoth". In: *Science* 367.6481. Publisher: American Association for the Advancement of Science Section: Research Article. ISSN: 0036-8075, 1095-9203. DOI: 10.1126/science.aay3999.

Stern, S. A. et al. (Oct. 16, 2015). "The Pluto system: Initial results from its exploration by New Horizons". In: *Science* 350.6258, aad1815. ISSN: 0036-8075, 1095-9203. DOI: 10.1126/science.aad1815.

Stern, S. A. et al. (Apr. 14, 2020). "Pluto's Far Side". In: *Icarus*, p. 113805. ISSN: 0019-1035. DOI: 10.1016/j.icarus.2020.113805.

Stöffler, D. et al. (2006). "Cratering history and lunar chronology". In: *Reviews in Mineralogy and Geochemistry* 60.1, pp. 519–596.

Strom, R. G., R. Malhotra, T. Ito, F. Yoshida, and D. A. Kring (Sept. 16, 2005). "The Origin of Planetary Impactors in the Inner Solar System". In: *Science* 309.5742. Publisher: American Association for the Advancement of Science Section: Report, pp. 1847–1850. ISSN: 0036-8075, 1095-9203. DOI: 10.1126/science.1113544.

Tera, F., D. Papanastassiou, and G. Wasserburg (1974). "Isotopic evidence for a terminal lunar cataclysm". In: *Earth and Planetary Science Letters* 22.1, pp. 1–21.

Trowbridge, A., H. Melosh, J. Steckloff, and A. Freed (2016). "Vigorous convection as the explanation for Pluto's polygonal terrain". In: *Nature* 534.7605, p. 79.

Tsiganis, K., R Gomes, A Morbidelli, and H. Levison (2005). "Origin of the orbital architecture of the giant planets of the Solar System". In: *Nature* 435.7041, p. 459.

Turcotte, D. L., R. J. Willemann, W. F. Haxby, and J. Norberry (1981). "Role of membrane stresses in the support of planetary topography". In: *Journal of Geophysical Research: Solid Earth* 86 (B5), pp. 3951–3959. ISSN: 2156-2202. DOI: 10.1029/JB086iB05p03951.

Turcotte, D. and G Schubert (2002). *Geodynamics, 456 pp.* Cambridge Univ. Press, New York.

Walsh, K. J. and A. Morbidelli (2011). "The effect of an early planetesimal-driven migration of the giant planets on terrestrial planet formation". In: *Astronomy & Astrophysics* 526, A126.

Watts, A. B. (2001). *Isostasy and Flexure of the Lithosphere.* Cambridge University Press.

Weaver, H. A., W. C. Gibson, M. B. Tapley, L. A. Young, and S. A. Stern (2009). "Overview of the New Horizons Science Payload". In: *New Horizons: Reconnaissance of the Pluto-Charon System and the Kuiper Belt.* Ed. by C. T.

Russell. New York, NY: Springer, pp. 75–91. ISBN: 978-0-387-89518-5. DOI: 10.1007/978-0-387-89518-5_5.

Werner, S. C. (2014). "Moon, Mars, Mercury: Basin formation ages and implications for the maximum surface age and the migration of gaseous planets". In: *Earth and Planetary Science Letters* 400, pp. 54–65.

Wetherill, G. (1975). "Late heavy bombardment of the moon and terrestrial planets". In: *Lunar and Planetary Science Conference Proceedings*. Vol. 6, pp. 1539–1561.

White, O. L. et al. (2017). "Impact crater relaxation on Dione and Tethys and relation to past heat flow". In: *Icarus* 288, pp. 37–52.

Wieczorek, M. A. and M. Meschede (2018). "SHTools: Tools for Working with Spherical Harmonics". In: *Geochemistry, Geophysics, Geosystems* 19.8. _eprint: https://agupubs.onlinelib pp. 2574–2592. ISSN: 1525-2027. DOI: 10.1029/2018GC007529.

Wieczorek, M. A. and F. J. Simons (Sept. 1, 2005). "Localized spectral analysis on the sphere". In: *Geophysical Journal International* 162.3. Publisher: Oxford Academic, pp. 655–675. ISSN: 0956-540X. DOI: 10.1111/j.1365-246X.2005.02687.x.

Wieczorek, M. A. et al. (2013). "The crust of the Moon as seen by GRAIL". In: *Science*, p. 1231530.

Wilhelms, D., V. Oberbeck, and H. Aggarwal (1978). "Size-frequency distributions of primary and secondary lunar impact craters". In: *Lunar and Planetary Science Conference Proceedings*. Vol. 9, pp. 3735–3762.

Wilhelms, D. E. and J. F. McCauley (1971). *Geologic map of the near side of the Moon.* US Geological Survey Reston.

Wilhelms, D. E., J. F. with sections by McCauley, and N. J. Trask (1987). *The geologic history of the Moon.* USGS Numbered Series 1348. Code Number: 1348 Code: The geologic history of the Moon Publication Title: The geologic history of the Moon Reporter: The geologic history of the Moon Series: Professional Paper. DOI: 10.3133/pp1348.

Zuber, M. T. et al. (2013). "Gravity field of the Moon from the Gravity Recovery and Interior Laboratory (GRAIL) mission". In: *Science* 339.6120, pp. 668–671.